

Alma Mater Studiorum – Università di Bologna

DOTTORATO DI RICERCA IN
SCIENZE CHIMICHE

Ciclo XXVI

Settore Concorsuale di afferenza: 03/C2

Settore Scientifico disciplinare: CHIM/05

TITOLO TESI

CHARGE TRANSPORT PROPERTIES OF ORGANIC
CONJUGATED POLYMERS FOR PHOTOVOLTAIC
APPLICATIONS

Presentata da: Sara Righi

Coordinatore Dottorato

Prof. Aldo Roda

Relatore

Prof. Stefano Stagni

Correlatori

Dr.ssa Nadia Camaioni

Dr.ssa Francesca Tinti

Esame finale anno 2014

*To my family and
to my friend and sister Roberta*

ABSTRACT

Charge transport in conjugated polymers as well as in bulk-heterojunction (BHJ) solar cells made of blends between conjugated polymers, as electron-donors (D), and fullerenes, as electron-acceptors (A), has been investigated.

It is shown how charge carrier mobility of a series of anthracene-containing poly(p-phenylene-ethynylene)-alt-poly(p-phenylene-vinylene)s (AnE-PVs) is highly dependent on the lateral chain of the polymers, on a moderate variation of the macromolecular parameters (molecular weight and polydispersity), and on the processing conditions of the films. For the first time, the good ambipolar transport properties of this relevant class of conjugated polymers have been demonstrated, consistent with the high delocalization of both the frontier molecular orbitals.

Charge transport is one of the key parameters in the operation of BHJ solar cells and depends both on charge carrier mobility in pristine materials and on the nanoscale morphology of the D/A blend, as proved by the results here reported. A straight correlation between hole mobility in pristine AnE-PVs and the fill factor of the related solar cells has been found.

The great impact of charge transport for the performance of BHJ solar cells is clearly demonstrated by the results obtained on BHJ solar cells made of neat-C₇₀, instead of the common soluble fullerene derivatives (PCBM or PC₇₀BM). The investigation of neat-C₇₀ solar cells was motivated by the extremely low cost of non-functionalized fullerenes, compared with that of their soluble derivatives (about one-tenth). For these cells, an improper morphology of the blend leads to a deterioration of charge carrier mobility, which, in turn, increases charge carrier recombination. Thanks to the appropriate choice of the donor component, solar cells made of neat-C₇₀ exhibiting an efficiency of 4.22% have been realized, with an efficiency loss of just 12% with respect to the counterpart made with costly PC₇₀BM.

TABLE OF CONTENTS

ABSTRACT	I
1. INTRODUCTION	1
1.1 <i>The promise of organic electronics</i>	1
1.2 <i>Organic conjugated materials</i>	3
1.3 <i>Charge transport in organic solids</i>	5
1.4 <i>Organic solar cells</i>	7
1.5 <i>Charge transport and loss channels in organic solar cells</i>	9
1.6 <i>Aim of the thesis</i>	11
2. EXPERIMENTAL METHODS	13
2.1 <i>Measurement of charge carrier mobility</i>	13
2.1.1 <i>Space-charge limited-current</i>	13
2.1.2 <i>Time of Flight</i>	15
2.1.3 <i>Admittance spectroscopy</i>	16
2.2 <i>Solar cells: preparation and characterization</i>	19
2.2.1 <i>Device preparation</i>	21
2.2.2 <i>Current-voltage characterization</i>	22
2.2.3 <i>Analysis of photocurrents</i>	26
2.2.4 <i>Impedance spectroscopy</i>	28
3. CHARGE TRANSPORT IN ANTHRACENE-CONTAINING POLY((P-PHENYLENE-ETHYNYLENE) -ALT-POLY(P-PHENYLENE- VINYLENE))S	30
3.1 <i>Materials</i>	31
3.2 <i>Ambipolar behaviour</i>	33
3.3 <i>Effect of side-chains</i>	37
3.4 <i>Effect of solvent and thermal treatments</i>	44
3.5 <i>Effect of a fine variation of the macromolecular parameters</i>	49
3.5.1 <i>Effect on the optical properties</i>	50

3.5.2	<i>Effect on the structural and morphological properties</i>	52
3.5.3	<i>Effect on charge carrier mobility</i>	56
3.5.4	<i>Effect on the performance of BHJ solar cells</i>	58
3.6	<i>Discussion</i>	61
4.	CHARGE TRANSPORT IN SOLAR CELLS MADE OF LOW BANDGAP CONJUGATED POLYMERS AND NEAT-C₇₀	64
4.1	<i>Materials</i>	64
4.2	<i>Solar cells made of neat-C₇₀ as electron acceptor</i>	66
4.2.1	<i>Photovoltaic parameters</i>	66
4.2.2	<i>Analysis of photocurrents</i>	71
4.2.3	<i>Charge carrier mobility</i>	75
4.2.4	<i>Impedance spectra</i>	77
4.2.5	<i>Blend morphology</i>	79
4.3	<i>The use of pyrene as C₇₀ disperdant</i>	82
4.3.1	<i>Blend morphology</i>	83
4.3.2	<i>Photovoltaic parameters</i>	84
4.3.3	<i>Analysis of photocurrents</i>	87
4.3.4	<i>Charge carrier mobility</i>	89
4.3.5	<i>Impedance spectra</i>	90
4.4	<i>Discussion</i>	93
5.	CONCLUDING REMARKS	96
	LIST OF PUBLICATIONS	98
	REFERENCES	99
	ACKNOWLEDGEMENTS	103

CHAPTER 1 – INTRODUCTION

1.1 *The promise of organic electronics*

Nowadays we live in an electronic world, indeed the use of personal computers, tablets and smart phones is steadily increasing. In 2012, there were an estimated 30–40 processors per person, on average, with some individuals surrounded by as many as 1000 processors on a daily basis.^[1] However, the resources and methodologies used to fabricate electronic devices bring up urgent questions about the negative environmental impacts of the manufacture, use, and disposal of electronic devices.

The use of organic conjugated materials^[2,3] to produce electronic devices could enable a more eco–friendly and sustainable way to let the electronic world grow. Chemists are synthesizing a wealth of new organic materials for use in electronic devices, which enable novel properties impossible to be replicated with traditional inorganic semiconductors like silicon. These carbon–based materials, like the ones of living things, hold the promise to expand our electronic landscape in ways that will radically change the way society interacts with technology. Indeed, an electronics made of organic materials, *organic electronics*, may be printed on flexible substrates at room temperature, making possible electronic newspapers and magazines, smart windows, flexible photovoltaic sheets and luminescent wallpapers. In other words, organic materials give to electronic devices unique properties such as mechanical flexibility, lightweight, sensing, biocompatibility and low–temperature processing,^[4-6] impossible to be achieved with silicon.

Some applications of organic electronics have already been realized, like OLED (organic light emitting diodes) smartphones and low–cost solar cells being installed on rooftops in rural off–grid communities in South Sudan. Some others, like the ultra–thin OLED TVs and foldable smartphones, are expected to be launched in the near future. Further applications, like electronic skin which mimics human skin with its tactile sensitivity, will take longer. Still others cannot be foreseen. The potential future applications are many and varied, spanning across multiple fields: medicine and biomedical research, energy and environment, communications and

entertainment, home and office furnishings, clothing and personal accessories, and more.

The market of organic electronics is growing with an annual rate of 70%.^[7] By 2015, 80% of organic electronic materials will be sold into three main applications, as shown in *Figure 1.1*: Radio Frequency IDentification (RFID), display backplanes and OLED lighting and displays.

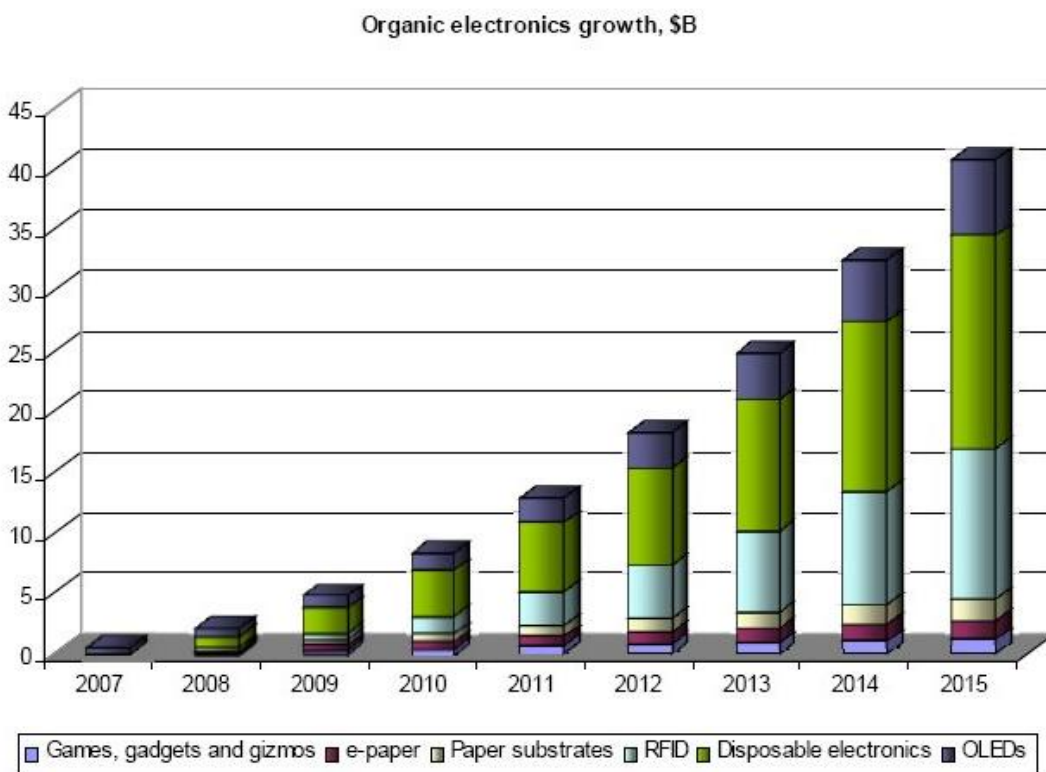


Figure 1.1 Organic electronics market actual and forecast growth rate by segment. Source: www.oled-info.com/organic-electronic-growth-chart-nanomarkets-2009.

Inexpensive printed RFID tags will replace barcodes in some applications, giving to packaging and low cost products a great deal of self-information while e-paper technology will replace ordinary paper as information medium in applications where updateability is crucial. For disposable electronics, a large market is expected to emerge for inexpensive conductive inks, which are far less demanding than larger displays or solar panels.

In summary, *organic electronics* has clearly made huge improvements over the past few decades, with some devices already on the market and a multitude of

prototypes under development. It will continue to grow, changing the way society interacts with technology. However, there are also challenges. Charge carrier mobility of organic materials is typically orders of magnitude lower than its silicon counterpart and its enhancement is expected to expand the market of organic electronics.

1.2 Organic conjugated materials

Organic conjugated materials, small molecules and polymers,^[8,9] have the typical chemical structure with the alternation of single and double (or triple) carbon-carbon bonds, determining their electronic properties. Single bonds are referred as σ -bonds whereas double bonds embody one σ -bond and one π -bond. In a sigma bond the orbital overlapping is always along the inter-nuclear axis and the probability to find the shared electron in a σ -bond is large between the two carbon nuclei. The π -bonds entail the electrons in the remaining p-orbital for each carbon atom. The p-orbitals are electron clouds that are generally located above and below each carbon atom. The overlapping of two atomic p-orbitals forms a molecular π -bond. The π -bond does not overlap in the region directly between the two carbon nuclei, where the σ -bond is combined, but it is found on the sides, for example above and below, of the axis joining the two nuclei. In this case, the probability to find the shared electron is larger a bit outside the direct line between the two atoms, and at two places in the space surrounding the atoms.

Among organic conjugated materials, conjugated polymers are of particular relevance for organic electronics. This because they combine electronic properties similar to those of traditional semiconductors with the mechanical ones of common plastics. Conjugated polymers have a σ -bond backbone of overlapping sp^2 -orbitals and the remaining out-of-plane p-orbitals (p_z) of the carbon atoms overlap with neighbouring p_z -orbitals to make the π -bonding. The two overlapping positions are called bonding (π) and anti bonding (π^*), the latter with a higher energy. The π -bonding electrons are free to move at certain distance over the molecular chain. As an example, the molecular structure of ethylene, the simplest molecule with a

double carbon–carbon bond, is shown in *Figure 1.2*, together with the overlap of the sp^2 -orbitals and the p -orbitals to form σ -bonds and π -bonds.

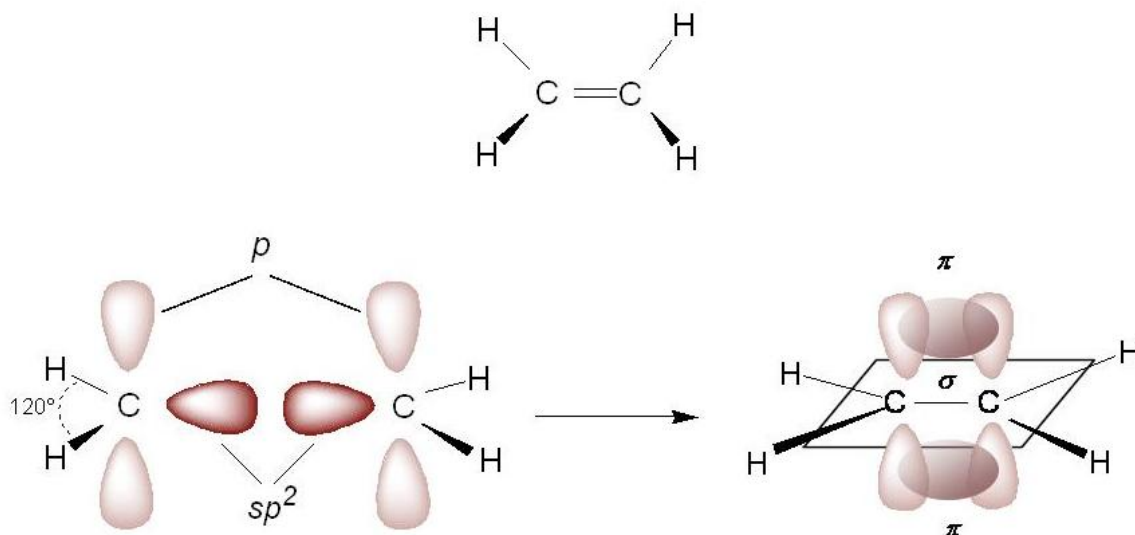


Figure 1.2 Molecular structure of ethylene (above) and the overlap of atomic sp^2 and p -orbitals to form molecular σ and π -bonds (below).

The features of the π -bonds are the origin of the semiconducting properties of organic conjugated materials. The semiconducting properties are enabled by the quantum mechanical overlap of the p -orbitals that produces π and π^* orbitals. The highest energy π orbital is called HOMO (Highest Occupied Molecular Orbital) and the lowest energy π^* one is the LUMO (Lowest Unoccupied Molecular Orbital). The difference in energy between these two levels is the energy gap, defining the optoelectronic properties of organic conjugated materials.

The main advantages of organic conjugated materials, compared to inorganic semiconductors, are:

- the availability of new organic materials is almost unlimited, while inorganic semiconductors are still a few;
- the electronic properties of organic materials can be easily modulated through molecular design;
- organic materials are lightweight;

- organic materials, if designed with appropriate side substituents, can be processed from solution with printing techniques (ink-jet printing, screen printing, etc..) over any substrate of large area;
- the absorption coefficient of organic materials is typically very high ($> 10^5 \text{ cm}^{-1}$).

The latter point is of particular interest for the photovoltaic application, for which efficient absorption of sunlight in thin films is required.

1.3 Charge transport in organic solids

Charge transport properties constitute a major determining factor for the operation of any electronic device and mainly for *organic electronics*, given the much worse mobility of charge carriers in organic materials, compared to that in conventional semiconductors. Indeed, the process of charge transport in organic materials is very different from that of inorganic semiconductors, due to the molecular nature of organic solids. While inorganic semiconductors show an energy band structure and charge transport is a band-like process, in organic materials charges are localized to single molecules and are not highly delocalized. Therefore, charge transport in such localized systems occurs via an “hopping” process,^[10] with charge carriers tunnelling from one localized state to another within the lattice of molecular sites. This localization as well as potential for collisions, scattering and delays, result in charge carrier mobility typically ranging between $10^{-7} \text{ cm}^2 \text{ V}^{-1} \text{ s}^{-1}$ to $10 \text{ cm}^2 \text{ V}^{-1} \text{ s}^{-1}$ in organic solids,^[11] orders of magnitude lower compared to inorganic crystalline semiconductors.

In disordered organic materials hopping transport is a process determined by two main factors:^[12] the transfer integral and the reorganization energy. The transfer integral represents basically the overlap of the HOMO levels, for hole transport, and of the LUMO levels for electron transport. The magnitude of the transfer integral is controlled by the wave functions of the π -clouds, by their orientations with respect to one another, and by their separation. The higher the transfer integral is, the faster the hopping rate is, and the higher charge carrier mobility is. The reorganization energy is the energy cost due to geometry modifications to go from a neutral to a charged state and vice versa. The lower the

reorganization energy is, the smaller the geometry relaxations and the higher the charge transfer rate are.

Differently from traditional semiconductors, charge transport in organic materials is usually field and thermally activated. The Poole–Frenkel conduction formalism has been shown to be applicable to charge transport in organic solids for electric fields from 10^4 to 10^6 V cm⁻¹.^[13-15] The Poole–Frenkel expression,^[16,17] given by Equation 1.1, relates the mobility μ , to the electric field E ,

$$\mu(E) = \mu_0 \exp(\gamma\sqrt{E}) \quad (1.1)$$

where μ_0 denotes the mobility at zero-field and γ is the parameter that describes the field dependence.

Concerning the positive dependence of μ with the absolute temperature T usually observed for disordered organic materials, it is explained in terms of the additional thermal energy provided to overcome the barriers resulting from energetic disarray. Bässler's disorder formalism^[18] is the most prominent model to account for both the field and the temperature dependence of μ in organic solids. In this case, the disorders in both position (including orientational effects) and energy are considered to be Gaussian distributions with widths of Σ and σ , respectively. Equation 1.2 features the full expression for Bässler's formalism:

$$\mu(E, T) = \mu_\infty \exp\left[-\left(\frac{2\sigma}{3k_B T}\right)^2\right] \exp\left\{C\left[\left(\frac{\sigma}{k_B T}\right)^2 - \Sigma^2\right]E^{1/2}\right\} \quad (1.2)$$

where μ_∞ is the mobility at infinite temperature and C is an empirical constant.

While the understanding of charge transport in disordered organic materials is growing, charge carrier mobility is still a rather empirical quantity, as simulations are still inadequate to predict it *a priori*. Thus, it must be accurately measured for all systems of interest to really know its value.

1.4 Organic solar cells

The core of organic solar cells is the photoactive layer, which is generally composed by two organic π -conjugated materials with suitable energy levels: an electron-donor (D) and an electron-acceptor (A).^[19,20] Conjugated polymers or small molecules are commonly used as electron-donors while soluble derivatives of fullerene are commonly used as electron-acceptors. Fullerenes have not been replaced yet by other acceptors because of their unique properties such as high electron affinity and high electron mobility, making them the best electron-acceptors till now.^[21] The photoactive layer, typically around 100–200 nm in thickness, is interposed between two collecting electrodes: the anode for positive charge carriers and the cathode for electrons. Additional layers of electron or hole transporting materials, are usually included at the interface between the active layer and the electrodes for a more efficient collection of charge carriers.^[22]

One of the main differences between inorganic semiconductors and organic materials is given by the value of the relative dielectric constant, very low in organic materials (~ 3), highly affecting the behaviour of the related solar cells. Indeed, differently from inorganic semiconductors, the absorption of light with energy higher than the energy gap does not lead to the generation of free pairs of charge carriers in organic materials, but to Frenkel-type excitons. An exciton can be considered as a bound state of an electron and a hole which are attracted each other by the electrostatic Coulomb interaction. To allow exciton dissociation, a driving force exceeding their binding energy (typically of 0.3–0.5 eV) is required. This is possible at the D/A interface of the active layer of organic solar cells if the energy offsets between the LUMO and HOMO levels of the two materials are sufficiently high. In summary, the process leading to the generation of free charge carriers in organic solar cells is much more complex than in the inorganic counterpart and is composed of three steps:^[23]

1. the photoexcitation of the absorber material(s) causes the promotion of electrons from the ground state to the excited state, leading to the generation of Frenkel-type excitons;

- excitons photogenerated within a diffusion length (typically 10–20 nm) from the D/A interface have the chance to reach it before decaying, radiatively or not;
- if the offsets of the energy levels of the D/A pair are higher than the exciton binding energy, excitons can dissociate at the D/A interface. Excitons photogenerated in the donor side dissociate by transferring the electron to the LUMO level of the acceptor (photoinduced electron–transfer, *Figure 1.3a*) and retaining the positive charge. Those created in the other side transfer the hole to the HOMO of the donor (photoinduced hole–transfer) while retaining the negative charge.

The role of an intermediate state between photogenerated excitons and completely unbound electron–hole pairs, denoted as charge transfer state, is still debated.^[24] It could be responsible for the decay of the photoexcitation by recombination of the bound electron–hole pair and leading to a loss for solar cells.

Free charge carriers originated from the dissociation of excitons are free to move. They are transported through the respective materials (electrons in the acceptor and holes in the donor) and collected at the respective electrodes.

The best approach for the active layer of organic solar cells is represented by the intimate mixing of the donor and the acceptor material, the so-called bulk–heterojunction (BHJ) approach (*Figure 1.3b*).^[25,26]

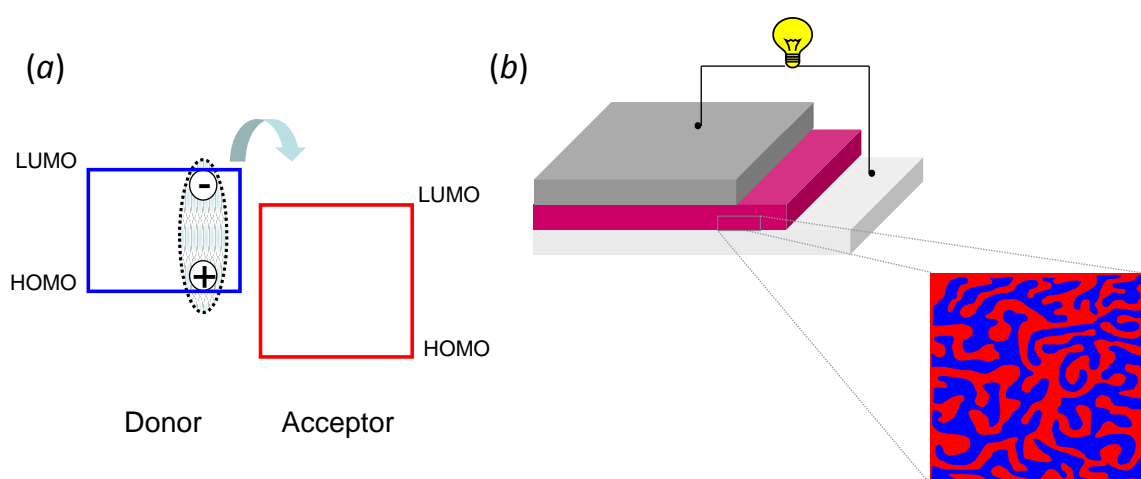


Figure 1.3 Photoinduced electron–transfer from the donor to the acceptor (a) and the structure of a bulk–heterojunction solar cell (b).

In a BHJ solar cell the donor and the acceptor materials are mixed on the nanoscale level to form a distributed D/A interface throughout the bulk of the device. In this way all photogenerated excitons are within a diffusion length of the D/A interface and can dissociate into free charge carriers. The fine control of the nanoscale morphology of the interpenetrating D/A network is crucial to ensure the best trade-off between high generation of free charge carriers and their efficient transport to the respective electrodes.^[27] Indeed a phase separation of the order of the exciton diffusion length is required for the efficient diffusion of photogenerated excitons to the D/A heterojunction, while a higher segregation is usually useful to achieve suitable bicontinuous percolative donor and acceptor pathways for effective charge transport.

The new millennium has seen a rapid progression of the performance of organic solar cells, not only due to the utilization of more suitable electron-donor materials,^[28] with respect to the past, but mainly triggered by the fine control over the nanoscale morphology of the interpenetrating D/A network.^[29] Currently the record power conversion efficiency of organic solar cells is around 10%.^[30]

Organic solar cells could really represent a new technology that in the mid-long term could lead to affordable energy. In addition, they are light-weight and can be made flexible, opening the possibility for a range of new applications. Large-area, pliable devices can be fabricated easily and inexpensively, by employing cost-effective techniques like, for instance, ink-jet or screen printing, and slot-die, gravure or spray coating.

1.5 Charge transport and loss channels in organic solar cells

Charge transport in the two different phases of the active layer of organic solar cells, highly dependent on the blend morphology as well as on the transport properties of pristine materials, is strictly related to most of the channel losses for these devices. Indeed, to achieve an efficient collection of charge carriers at the contacts, the mobility of charge carriers must be high enough to prevent high losses due to recombination (bimolecular recombination). In other words, charge carriers must reach electrodes prior to recombination. In addition, for materials with a low

mobility, this puts also a restraint on the maximum thickness of the active layer,^[31] because a longer residence time of charge carriers in the film creates more chances for recombination.

Bimolecular or non-geminate recombination is due to the recombination at the D/A interface of free charge carriers of opposite sign coming from distinct photoexcitation events (*Figure 1.4a*). Bimolecular recombination is mainly determined by the mobility of the slowest charge carriers,^[32] usually holes in the donor phase.

Another type of recombination can occur in organic solar cells. After photoinduced charge transfer, the still bound pairs of charges (charge transfer states) that cannot escape the mutual Coulombic attraction will recombine at the D/A interface (*Figure 1.4b*). In this case (monomolecular or geminate recombination), charge carriers within a single photoexcitation event recombine, or better, recombination occurs before complete dissociation of bound states at the interface. Charge carrier mobility seems to play a relevant role also for geminate recombination.^[33]

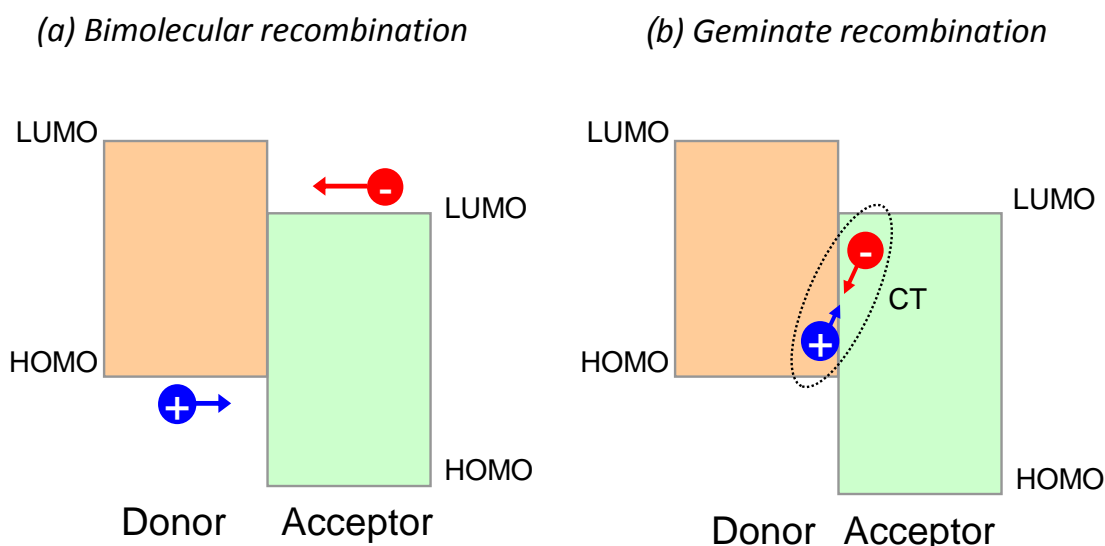


Figure 1.4 Bimolecular recombination of free charge carriers (a) and geminate recombination of charge transfer (CT) states (b).

High charge carrier mobilities in the donor and in the acceptor phases are required to reduce recombination losses in organic solar cells, but also balanced.

Indeed, strongly unbalanced mobilities, differing by more than one order of magnitude, lead to the formation of space charge in the cell, due to the longer residence time of the slowest carriers. Space charge formation strongly enhances bimolecular recombination.^[34]

In summary, charge transport in the bi-continuous D/A network is critical for cell behaviour. Electron-donor materials showing high hole mobility are required for the photovoltaic application, possibly comparable with that of common fullerene derivatives (of the order of $10^{-3} \text{ cm}^2 \text{ V}^{-1} \text{ s}^{-1}$).^[35] In addition to the good intrinsic transport properties of the composing materials, the blend morphology has to provide continuous pathways for the efficient transport of both type of charge carriers to the respective electrodes.

1.6 Aim of the thesis

The aim of the work of the thesis is the investigation of charge transport, both in pristine polymer films and in the active layer of bulk-heterojunction solar cells made of conjugated polymers as electron-donors and fullerene as acceptor.

Charge carrier mobility in a series of anthracene-containing poly((p-phenylene-ethynylene)-alt-poly(p-phenylene-vinylene))s (AnE-PVs) was studied as a function of the electric field to understand the complex interplay between the typical factors affecting charge transport properties (chemical structure, macromolecular parameters and film processing conditions) and charge carrier mobility in this relevant class of conjugated polymers. The strong correlation between charge carrier mobility of pristine AnE-PV donors and the fill factor of related bulk-heterojunction solar cells, was also demonstrated.

The investigation of the critical role of charge transport in the D/A double network for the performance of organic photovoltaic devices was extended to bulk-heterojunction solar cells made of two low-energy-gap conjugated polymers and neat-C₇₀ as acceptor. The replacing of common fullerene derivatives with neat-fullerenes has a great advantage for an innovative photovoltaic technology as organic photovoltaics, for which low-cost is one of the key factors. Indeed, the cost of neat-fullerenes is roughly one tenth of that of common C₆₀ or C₇₀ derivatives,

chemically functionalised with suitable groups to enable an excellent solubility/processability in chlorinated solvents.

Given the extremely poor solubility of pristine fullerenes,^[36] very different morphologies for the related D/A blends are expected, compared to those made of functionalised C₆₀/C₇₀ derivatives, highly affecting both the dissociation of photogenerated excitons and the transport of charge carriers. The aim of the work is to find the conditions for the preparation of low-cost and high-efficiency organic solar cells made of neat-fullerene.

CHAPTER 2 – EXPERIMENTAL METHODS

2.1 Measurement of charge carrier mobility

Common techniques for the measurement of mobility in traditional semiconductors are not applicable to organic solids. This because undoped conjugated materials are required for most organic electronic applications, including the photovoltaic one, thus materials with a very low electrical conductivity, other than with a relatively low charge carrier mobility. Hence, alternative techniques are utilized for the characterization of charge transport in organic films, most of them used in this thesis, such as, space–charge limited–current (SCLC),^[37] time of flight (TOF),^[38] carrier extraction by linearly increasing voltage (CELIV),^[39] and admittance spectroscopy (AS).^[40] TOF and AS methods were used in this thesis for the investigation of charge carrier mobility in pristine polymer films, while the SCLC technique was employed for the measurement of charge carrier mobility in the donor and the acceptor phase of solar cells, this latter method being the most best–suited for very thin films, like the active layer of organic photovoltaic devices.

2.1.1 Space–charge limited–current

In the space–charge limited–current technique, charge carriers are injected by applying an electric field to an appropriate device provided with ohmic contacts, in order the flowing current is not injection–limited. One–carrier devices are usually employed, in which the injection of only one type of carriers is allowed.

At high injection level, the space–charge regime is established in the sample, which limits the current by a lowering of the applied electric field, and the space–charge limited current density (in a trap–free material) is given by the Mott–Gurney equation (2.1):^[37]

$$J_{SCLC} = \frac{9}{8} \varepsilon_0 \varepsilon_r \mu \frac{V^2}{d^3} \quad (2.1)$$

where ε_r is the relative dielectric constant of the material, ε_0 is the dielectric constant of vacuum, d the thickness of the organic layer and V is the net voltage. The net voltage is given by:

$$V = V_{app} - V_{rs} - V_{bi} \quad (2.2)$$

where V_{app} is the applied voltage, V_{rs} is the voltage drop due to the series resistance of the contacts and V_{bi} is the built-in voltage, due to the possible asymmetry of the electrical contacts and estimated from the difference of the work function of the contacts .

Charge carrier mobility is obtained by the fit of the Mott–Gurney equation to the experimental J – V curve. Equation 2.1 assumes that mobility is independent of the electric field, however in many cases a more satisfactory fitting of the experimental data is obtained by using Equation 2.3, which accounts for the dependence of mobility on the electric field:

$$J_{SCLC} = \frac{9}{8} \varepsilon_0 \varepsilon_r \mu_0 \frac{V^2}{d^3} \exp\left(\frac{0.89\gamma}{\sqrt{d}} \sqrt{V}\right) \quad (2.3)$$

where μ_0 is the zero-field mobility and γ is the field-activation factor.

The SCLC technique was used in this thesis for mobility measurements in the active layer of solar cells (about 70–100 nm thick). Hole-only and electron-only devices were prepared, with the organic layer deposited in the same conditions used for solar cell fabrication, in order to measure the mobility of holes in the donor phase and that of electrons in the acceptor phase, respectively. The selective injection of the desired charge carriers was achieved by tuning the work function of the contacts near the HOMO level of the donor material (for hole-only) or near the LUMO of the acceptor (for electron-only) of the blend (*Figure 2.1*).

In hole-only devices, poly(3,4-ethylenedioxythiophene)/polystyrene sulphonic acid (PEDOT:PSS, Clevis P VP Al 4083 from H. C. Starck, with a work function of about 5.0 eV, quite matching with the HOMO level of typical donors) was used as the bottom injecting contact for holes, while Au (work function of about 5.0 eV) formed the top blocking electrode for electrons. On the contrary, aluminium (work

function of about 4.2 eV) was used in electron-only devices as the bottom blocking contact for holes, while the electron injection contact was realized with LiF/Al (work function of about 3.8 eV,^[41] matching with the LUMO level of fullerenes).

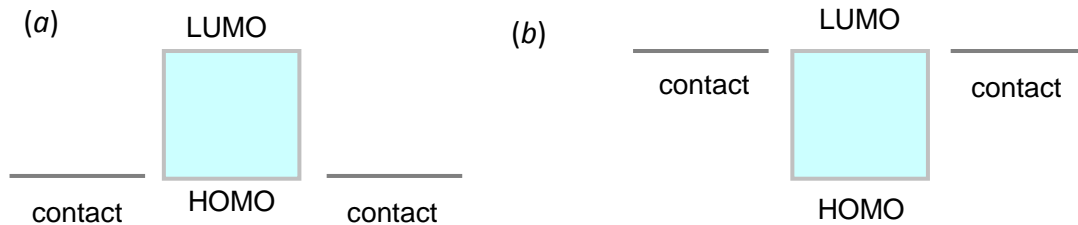


Figure 2.1 Ideal energy scheme of hole-only (a) and electron-only (b) devices. The contacts are represented with the Fermi energy level.

Hole-only devices were prepared onto glass substrates coated with Indium-Tin-Oxide (ITO, Kintec, sheet resistance = $20 \Omega/\square$, transmittance in the visible range $\sim 86\%$ and work function $\sim 4.8\text{--}4.9$ eV), while electron-only ones on glass. A selective chemical etching was used to pattern ITO electrodes. The substrates were previously cleaned in detergent and water, and then ultrasonicated in acetone and isopropyl alcohol for 15 minutes each.

PEDOT:PSS was spin-coated at 4000 rpm (~ 40 nm) onto UV-ozone-treated ITO substrates, and then baked in an oven, in air, at 140°C for 10 minutes. Metal layers were deposited by thermal evaporation at a base pressure of 3×10^{-6} mbar.

The blends were prepared and deposited as for solar cell fabrication (described in *paragraph 2.2.1* and in Chapter 3) onto ITO/PEDOT:SS or glass/Al, for hole-only and electron-only devices, respectively. After the blend deposition, the samples were transferred to an argon glove-box where the device structure was completed with the evaporation of the top electrode. Au (70 nm) was used as the top contact for hole-only devices and LiF/Al (20–80 nm) for electron-only ones. The device active area, defined by the shadow mask used for the top electrode deposition, was 25 mm^2 . The thickness of the blends, roughly the same of the active layer of solar cells, was measured with a Tencor Alphastep 200 profilometer.

The resulting device structure for hole-only and electron-only devices was ITO/PEDOT:PSS/blend/Au and glass/Al/blend/LiF/Al, respectively. The electrical characterization of the devices was carried out in glove-box at room temperature, by using a Keithley 2400 source-measure unit to take the current-voltage curves.

2.1.2 Time of Flight

The time-of-flight technique is well known and widely used to investigate charge transport in various low mobility solids. It was first developed between 1957 and 1960 by three independent scientists: Spear,^[42,43] Le Blanc^[44] and Kepler.^[45] The typical experimental setup is shown in *Figure 2.2*.

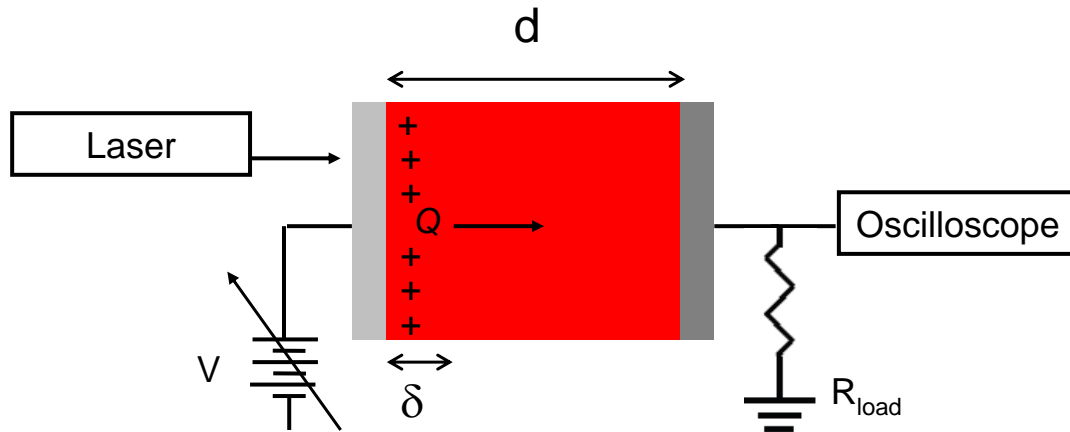


Figure 2.2 Typical time-of-flight experimental setup

In the TOF technique, charge carriers are photogenerated in the sample by a short laser pulse (a few ns long). The sample to be measured consists of a film of thickness d (usually on the order of microns) sandwiched between two blocking contacts (*Figure 2.3*), required to avoid the injection of dark charge carriers, one of which is semitransparent to receive pulsed illumination. The illuminated electrode is connected to a voltage source and the other one to a digital oscilloscope through a load resistor, (R_{load}). The method is based on the measurement of the current transient, due to the photogenerated charge carriers of the same sign (selected by the polarity of the applied bias), moving in the electric field created in the inter-electrode distance of the sample. The low conductivity of the material ensures

that, during the drift of the photogenerated charge carriers through the inter-electrode distance, the density of equilibrium charge carriers will be too low to redistribute the electric field inside the sample.

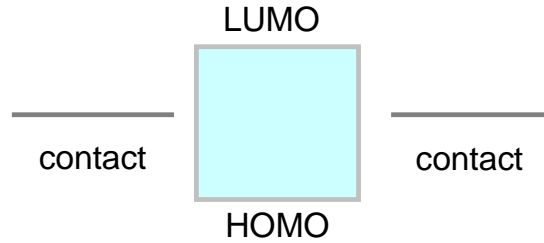


Figure 2.3 Ideal energy scheme of time-of-flight devices. The contacts are represented with the Fermi energy level

The TOF method is usually used in the so-called small signal mode. This regime is ensured when the photogenerated charge, Q , is much less than the charge on the electrodes at the given applied voltage V , i.e. $Q \ll C_g V$, where C_g is the geometrical capacitance of the sample. In addition, a strong absorption of light is required in a thin sheet δ of the sample ($\alpha d \gg 1$, where α is the absorption coefficient of the material), in order to generate a well-defined charge sheet, just below the illuminated electrode.

The transit time or drift time of charge carriers, t_{tr} , is the time the charge sheet takes to reach the collecting electrodes and exit from the sample. t_{tr} is related to charge carrier mobility through the equation:

$$\mu = \frac{d}{Et_{tr}} \quad (2.4)$$

In case of non-dispersive transport,^[46] i.e. if the charge sheet only spreads slightly and exits the sample cleanly, the shape of the photocurrent transient is close to rectangular (*Figure 2.4a*), showing a current plateau before a sharp drop representing the transit time of fastest charge carriers. Differently, in case of dispersive charge transport,^[47] the current transient does not demonstrate an obvious break point, but monotonically decreases with time (*Figure 2.4b*). In this

case, t_{tr} is estimated by the inflection point of the current transient usually observed when represented in a double-logarithmic scale.

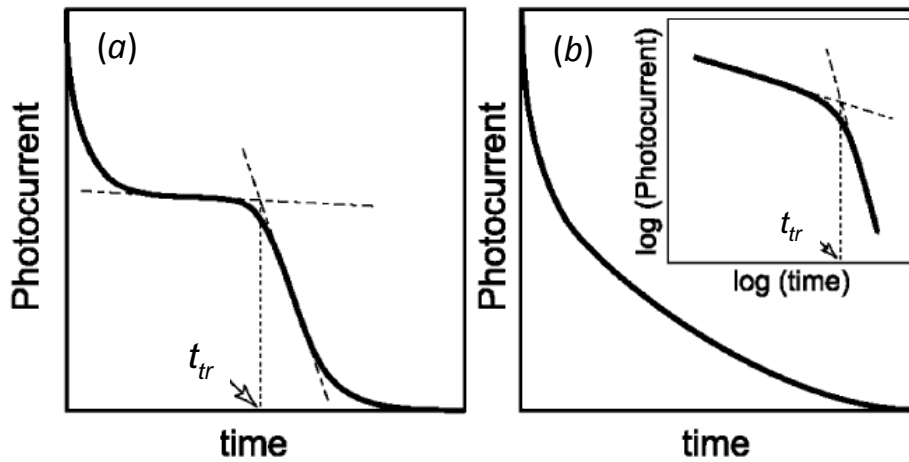


Figure 2.4 Typical time-of-flight transients for non-dispersive charge transport (a), and dispersive transport (b). The inset of (b) shows the signal in log-log scales.

The devices for TOF experiments were realized onto patterned glass/ITO or Al-coated substrates. Polymer films were deposited by drop-casting from 1,2-dichlorobenzene or chlorobenzene solutions (30 g L^{-1}), stirred for 4 days at $45\text{--}50 \text{ }^\circ\text{C}$. After deposition, the films were solvent-vapour annealed in chlorobenzene overnight. The device structure was completed with a vacuum evaporated semitransparent aluminium layer (18 nm), acting as the illuminated electrode. A nitrogen laser ($\lambda = 337 \text{ nm}$) with a pulse duration of 6–7 ns was used in single-pulse mode to photogenerate charge carriers. A variable dc potential was applied to the samples and, in order to ensure a uniform electric field inside the device, the total photogenerated charge was kept less than $0.1 C_g V$. The photocurrent was monitored across a variable load resistance by using a Tektronix TDS620A digital oscilloscope. The TOF experiments were performed at room temperature, under dynamic vacuum ($8 \times 10^{-6} \text{ mbar}$).

2.1.3 Admittance spectroscopy

Admittance spectroscopy is a powerful tool for the investigation of charge-carrier transport in high resistivity materials.^[40] For the application of this technique to the measurement of charge carrier mobility, charge carriers must be injected into the sample, as for the SCLC method. Depending on the sign of the carriers to be investigated, hole-only or electron-only devices are usually prepared.

In an admittance experiment, the charge relaxation, driven by a small voltage modulation v_{ac} , is probed.^[48] The amplitude and the phase difference of the corresponding alternating current, i_{ac} , are monitored as a function of frequency, f , obtaining a spectrum. Because of the capacitive components of the sample, i_{ac} is shifted with respect to v_{ac} , as shown in *Figure 2.5*.

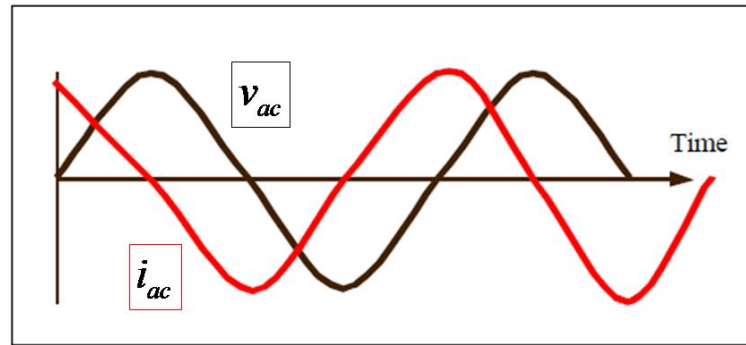


Figure 2.5 Alternating voltage modulation v_{ac} and corresponding alternating current i_{ac} .

The alternating current is linked to v_{ac} through the impedance Z of the sample:

$$Z(\omega) = \frac{v_{ac}(\omega)}{i_{ac}(\omega)} \quad (2.5)$$

where ω ($\omega = 2\pi f$) is the angular frequency. The admittance, Y , is defined as the reciprocal of impedance:

$$Y(\omega) = \frac{1}{Z(\omega)} = G(\omega) + iB(\omega) = G(\omega) + i\omega C(\omega) \quad (2.6)$$

where its real part, G , is the conductance, B is the susceptance, C is the capacitance, and i is the imaginary unit.

Free charge carriers are injected into the sample by superimposing a forward dc bias, V_{dc} , to the harmonic voltage modulation. In case of injection, the frequency dependence of Y is determined by the effect of the transit time t_{tr} of injected carriers. The capacitance spectrum makes a step around the frequency of t_{tr}^{-1} (Figure 2.6a) and tends, at higher frequencies, to the geometrical capacitance of the sample.

The average transit time of charge carriers can be easily evaluated from the negative differential susceptance, $-\Delta B$, obtained from capacitance through the following expression:

$$-\Delta B = \omega(C_g - C) \quad (2.7)$$

It has been demonstrated that t_{tr} is related to the frequency f_{max} at which $-\Delta B$ exhibits its maximum value through $f_{max} = kt_{tr}^{-1}$ (Figure 2.6b), where k is an empirical coefficient for which a value of 0.54 is usually assumed.^[49]

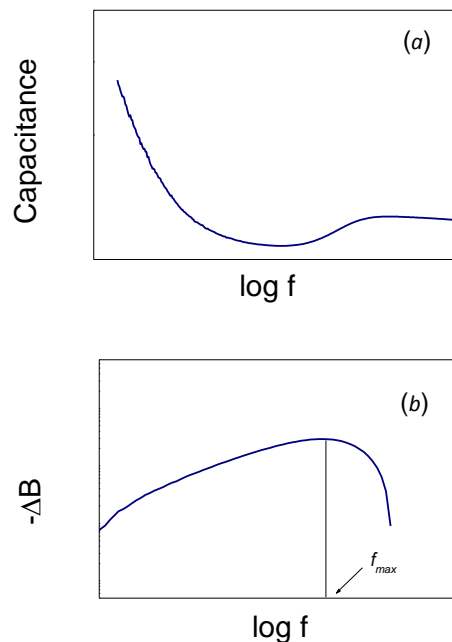


Figure 2.6 Typical frequency dependence of capacitance (a) and variation in the negative differential susceptance with frequency (b).

The hole-only devices used for AS measurements were prepared in the sandwiched structure ITO/PEDOT:PSS/polymers/Au, using the same conditions described in *paragraph 2.1.1*. The polymers were dissolved in chloroform (20–30 g L⁻¹) and deposited by spin-coating at a rotation speed ranging between 800 rpm and 1600 rpm (film thickness between 470 nm and 675 nm). Devices prepared with as-cast polymer films were compared with those made with annealed films:

- “*thermal annealed*”: polymer films were put onto a hot plate in glove-box at 90 °C for 20 minutes;
- “*solvent annealed*”: the films were solvent-vapour annealed (in chlorobenzene) overnight.

Then, the device structure was completed with the evaporation of Au layer (90 nm).

Admittance measurements were carried out at room temperature in glove-box by using an Agilent 4294A impedance analyser. The amplitude of the ac modulation voltage was 50 mV, the forward dc bias was varied in the range 0–10 V with a step of 1 V, and a frequency range of 40 Hz – 1 MHz was used.

2.2 Solar cells: preparation and characterization

The bulk-heterojunction solar cells were prepared in the so-called “conventional” device structure,^[22] with a bottom transparent hole-collecting electrode and a top opaque electron-collecting contact, according to usual procedures.

Solar cells were illuminated through the bottom contact by using a sun simulator (SUN 2000 Abet Technologies, AM1.5G). The intensity of the incident light power was calibrated using a certified silicon solar cell.

The electrical characterization of solar cells was carried out in a glove-box at room temperature and included:

- current density-voltage (*J-V*) characterization;
- analysis of photocurrents;
- impedance spectroscopy.

The J - V characterization (both in dark and under illumination) and the photocurrent measurements were performed by using a Keithley 2400 source-measure-unit, while impedance spectroscopy measurements were conducted using an Agilent 4294A impedance analyser.

2.2.1 Device preparation

Solar cells were fabricated onto glass/ITO patterned substrates, used as hole-collecting contacts. The patterned substrates were cleaned as described in *paragraph 2.1.1* and UVO-treated for 25 minutes. Then a layer of PEDOT:PSS was deposited and treated as described in *2.1.1*.

Polymers and fullerene derivatives were dissolved in chlorinated solvents (chlorobenzene or 1,2-dichlorobenzene) with concentrations in the range between 10 g L^{-1} and 34 g L^{-1} . The solutions were stirred at a temperature ranging between 40°C and 70°C for at least one night. The blend solutions were spin-coated in air onto the ITO/PEDOT:PSS substrates at a rotation speed ranging between 500 and 1000 rpm, in order to obtain the desired thickness. The details of the prepared solutions (solvent, concentration, D/A weight ratio) as well as of the deposition conditions are reported in *paragraph 3.5.1* and Chapter 4. After the spin-coating deposition of the active layer, the samples were transferred to a glove-box, where the device structure was completed through the thermal evaporation of the top electron-collecting electrode at a base pressure of 3×10^{-6} mbar. To this purpose, aluminium (100 nm) or modified-aluminium layers were thermally deposited, such as LiF (0.9 nm)/Al (80 nm). The active device area, defined by the shadow mask used for the top electrode deposition, was 8 mm^2 . The thickness of the active layer was in the range between 70 nm and 100 nm. The structure of the resulting solar cells and the scheme of the energy levels of the devices are shown in *Figure 2.5*.

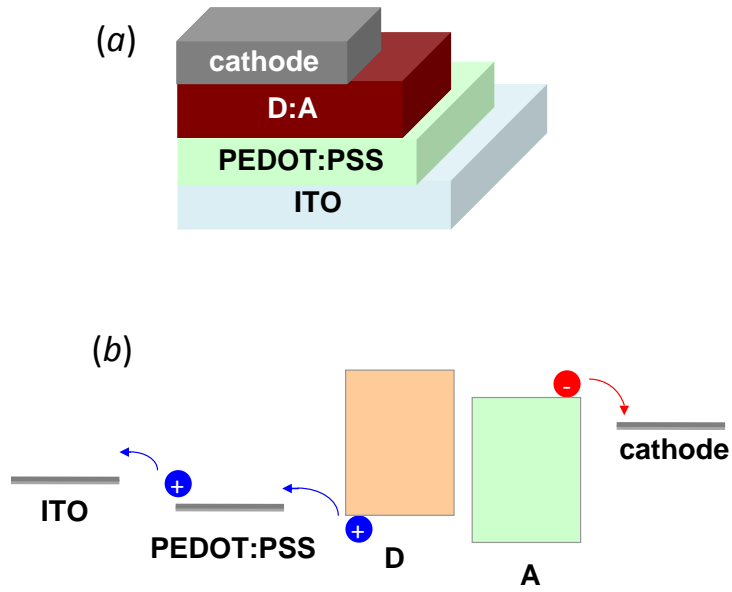


Figure 2.5 Structure of solar cells (a) and scheme of the energy levels (b).

2.2.2 Current–voltage characterization

When measured in the dark, the J – V characteristics of solar cells resemble the exponential response of a diode, with high current in forward bias and small current in reverse bias. Shining light on the device, generates a photocurrent in addition to the diode behaviour, and the J – V characteristics under illumination is ideally the superposition of the dark characteristics and the photocurrent.

Neglecting the effects of series and shunt resistances, the J – V characteristics of an ideal device in the dark can be described by the Shockley equation:^[50]

$$J = J_0 \left(e^{qV/kT} - 1 \right) \quad (2.8)$$

where, J_0 is the reverse saturation current density of the diode, q is the elementary charge and k is the Boltzmann constant. When the solar cell is illuminated, a photocurrent J_L is generated and it is dependent on light intensity. The effect of the photocurrent J_L on the J – V characteristics is that of a downward shift, as illustrated in Figure 2.6, and equation 2.8 becomes:^[33]

$$J = J_0 \left(e^{qV/kT} - 1 \right) - J_L \quad (2.9)$$

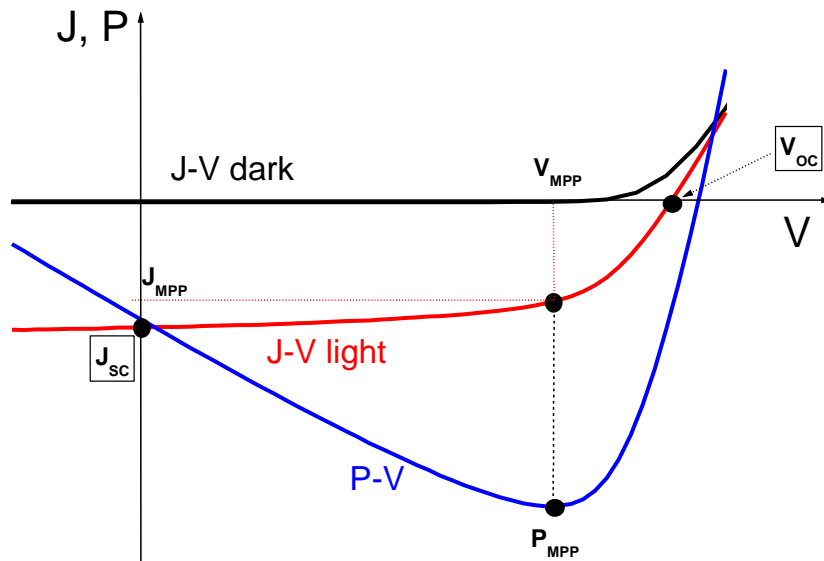


Figure 2.6 J - V characteristics of a solar cell in the dark (black line) and under illumination (red line). Plot of the power density as a function of voltage (blue line).

In Figure 2.6, the electrical power density P , the product of voltage and current density, is also plotted versus voltage, and the negative power indicates power generation.

The main photovoltaic parameters describing the performance of solar cells are the short-circuit current density (J_{sc}), the open-circuit voltage (V_{oc}), and the fill factor (FF). These parameters are determined from the illuminated J - V characteristics (Figure 2.6). The short-circuit current is the current that flows through the external circuit when the electrodes are short-circuited. J_{sc} is the photocurrent measured when the cell is short-circuited on itself (for $V = 0$ in equation 2.9):

$$J_{sc} = -J_L \quad (2.10)$$

The open-circuit voltage is the voltage at which no current flows through the external circuit. In this case the dark current compensates the photocurrent. The open-circuit voltage depends on the photo-generated current density and, assuming that the net current is zero, it is derived from equation 2.9:

$$V_{oc} = \frac{kT}{q} \ln \left(\frac{J_L}{J_0} - 1 \right) \quad (2.11)$$

The operation regime of a solar cell is not, however, neither under open-circuit nor under short-circuit condition, but it is connected to an external load to which provides an electrical power. The maximum power ($P_{MPP} = J_{MPP}V_{MPP}$) that the cell can deliver is related to the fill factor of the device, defined as:

$$FF = \frac{P_{MPP}}{J_{sc} V_{oc}} \quad (2.12)$$

The power conversion efficiency, η , usually expressed in percentage, is defined as the ratio between the generated maximum electrical power and the incident light power (P_{in}):

$$\eta = \frac{P_{MPP}}{P_{in}} = \frac{J_{sc} V_{oc} FF}{P_{in}} \quad (2.13)$$

Since η is dependent on both temperature and light power, solar cells are characterized in terms defined by a standard. For terrestrial applications the standard includes: temperature of 25 °C; a white light source with a spectral distribution AM1.5G, that is that of solar irradiance with the sun 45 ° above the horizon; the density of the incident light power of 100 mW cm⁻².

The photovoltaic parameters are obviously closely related to the electronic properties of the active layer of the cell. J_{sc} is mainly determined by the number of absorbed photons, and the efficiency of dissociation of photo-generated excitons into pairs of free charges. V_{oc} is a thermodynamic parameter mainly related to the energy difference between the LUMO of the acceptor and the HOMO of the donor.^[51,52] The value of fill factor is significantly dependent on charge transport properties in the D/A blend and on charge recombination processes.

The density of the light power incident on the cells was varied from a few mW cm⁻² to 100 mW cm⁻² by using a set of quartz neutral filters to attenuate the light beam from the sun simulator, calibrated at 100 mW cm⁻².

2.2.3 Analysis of photocurrents

For the analysis of photocurrents, the J - V characteristics is recorded by applying a voltage scan from a positive value, higher than V_{oc} , towards negative potentials. The density of the net photocurrent, J_{ph} , is given by:

$$J_{ph} = J_L - J_D \quad (2.14)$$

where J_D is the current density registered under dark conditions. J_{ph} is usually plotted, changed in sign, as a function of the effective voltage $V_0 - V$ (Figure 2.7), where V is the applied voltage and V_0 , the compensation voltage, is defined as $J_{ph}(V_0) = 0$.

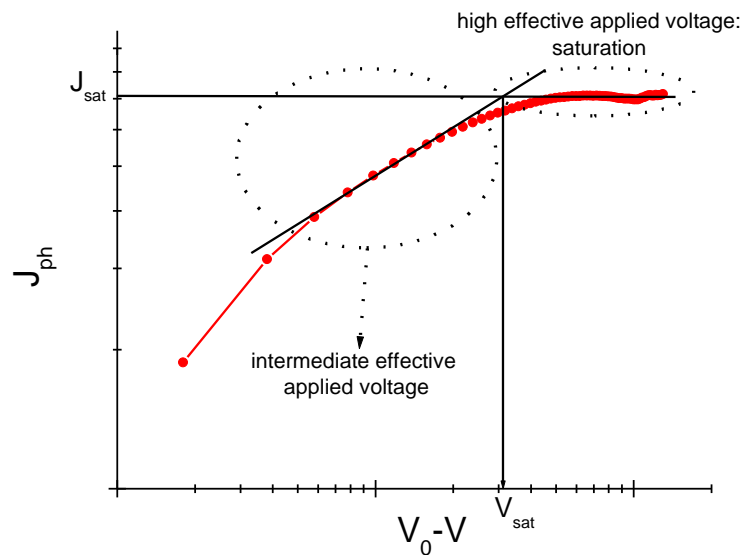


Figure 2.7 Typical plot of the net photocurrent as a function of the effective voltage.

At high effective voltages, i.e. at high reverse applied voltages or at high internal field, the photocurrent can saturate. In case of saturation, it is possible to calculate the maximum generation rate (G_{max}) of free electron–hole (e–h) pairs at the D/A interface by using the simple relation:^[53]

$$J_{sat} = qG_{max}d \quad (2.15)$$

where J_{sat} is the saturation photocurrent. In the saturation regime, all bound e–h pairs (CT states at the D/A interface) are separated into free charge carriers and consequently G_{max} is only governed by the amount of absorbed photons.

Being aware of G_{max} , it is possible to estimate the generation rate of free e–h pair for any applied voltage, $G(V)$, using the simple proportion:

$$\frac{G_{max}}{G(V)} = \frac{J_{sat}}{J_{ph}(V_0 - V)} \quad (2.16)$$

The dependence of J_{ph} on the effective voltage at low internal field is mainly governed by the competition between diffusion and drift current and J_{ph} scales linearly with $V_0 - V$. For intermediate and higher internal fields, J_{ph} may show a square–root dependence on the effective voltage. Such square–root behaviour is typically explained in terms of a space–charge–limited (SCL) or a $\mu\tau$ –limited model, where τ is the lifetime of free charge carriers before their recombination.^[54] The first type of limitation of J_{ph} typically occurs when the difference between the electron and the hole mobility in the D/A blend exceeds one order of magnitude (strongly unbalanced transport), leading to the accumulation of the slowest carriers in the device. The fingerprints of the SCL–limited J_{ph} are the $\frac{3}{4}$ power law dependence on the light power:

$$J_{ph} \propto P_{in}^{0.75} \sqrt{V_0 - V} \quad (2.17)$$

and a clear dependence on P_{in} of V_{sat} , V_{sat} being the saturation voltage at which J_{ph} starts to saturate (*Figure 2.6*).

Differently, in the $\mu\tau$ –limited case a too short carrier lifetime or a too low mobility limits the photocurrent, which linearly scales with P_{in} :

$$J_{ph} \propto P_{in} \sqrt{V_0 - V} \quad (2.18)$$

and V_{sat} is roughly independent of the light intensity.

A voltage scan from 1.4 V to –12 V was applied to the cells and the light intensity was varied as described in the previous *paragraph*.

2.2.4 Impedance spectroscopy

Impedance spectroscopy is a complex but very powerful tool, with many applications in the field of materials science.^[48] It is used to investigate relaxation phenomena of charge carriers and, when applied to solar cells, it permits the evaluation of charge carrier lifetime.^[55] Impedance spectroscopy can also reveals charge trapping phenomena in the D/A blends.^[56]

The impedance of the system, stimulated by an harmonic voltage as described in *paragraph 2.1.3*, and given by :

$$Z(\omega) = \frac{v_{ac}(\omega)}{i_{ac}(\omega)} = Re[Z(\omega)] + i Im[Z(\omega)] \quad (2.19)$$

is monitored as a function of frequency. The impedance spectrum is usually represented with the imaginary part of Z plotted against the real part of Z (Cole–Cole or Nyquist plot), with the frequency as the implicit variable.

The impedance spectrum is modelled on the basis of an equivalent circuit able to account for the electrical behaviour of the device. Each resistor or capacitor composing the equivalent circuit has a precise chemical/physical meaning, connected with the behaviour of the device under test. The values of the circuit elements are provided by the fit of the experimental data according to the model circuit, and their combinations leads to relevant parameters for the behaviour of the device (as lifetime of charge carriers, for solar cells). A simple example of an impedance spectrum in the Cole–Cole representation, together with the related equivalent circuit, is shown in *Figure 2.7*.

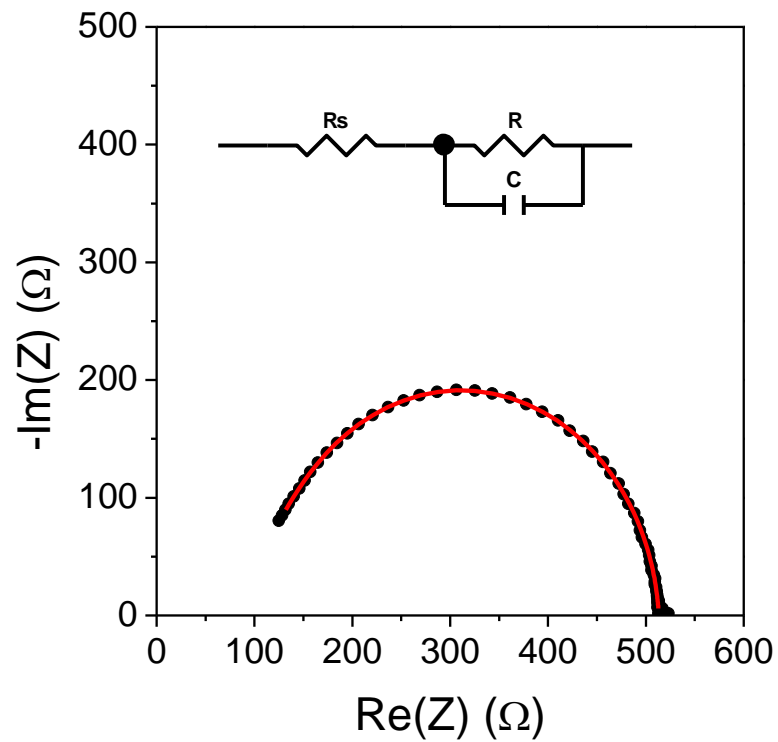


Figure 2.7 Example of Cole–Cole plot representation of an impedance spectrum (black points) and data fit (red curve) according to the model equivalent circuit shown as inset.

Impedance spectra of illuminated solar cells were taken in the frequency range 40 Hz – 1 MHz. The amplitude of the harmonic voltage was 20 mV. A dc bias equal to the open–circuit voltage of the cells was superimposed to the harmonic voltage.

CHAPTER 3 – CHARGE TRANSPORT IN ANTHRACENE-CONTAINING POLY ((P-PHENYLENE-ETHYNYLENE)-ALT-POLY (P-PHENYLENE-VINYLENE))S

This chapter is dedicated to the investigation of charge transport proprieties in a series of anthracene-containing poly((p-phenylene-ethynylene)-alt-poly(p-phenylene-vinylene))s (PPE-PPVs), denoted AnE-PVs. AnE-PVs, with the anthracene unit between two triple bonds, are a relevant class of conjugated polymers,^[57] exhibiting outstanding optoelectronic properties. Light-emitting diodes showing a turn-on voltage below 2 V^[58] and solar cells exhibiting a state-of-art efficiency of around 5%, for PPV-based materials, have been already demonstrated for this class of conjugated polymers.^[59] The advantage of the triple bond in the polymer structure, due to its cylindrical symmetry, is the preservation of the conjugation between aromatic groups in case of rotation of the aromatic plane, though it is maximum in the planar conformation.^[60, 61] It has been shown that PPE-PPVs are characterized by an enhancement of both backbone stiffness and electron affinity, as compared to parent PPV, due to the incorporation of the electron-withdrawing ethynylene units into the polymer backbone.^[62] Indeed, the triple bond acts as a bridge for the electrons of two aromatic systems also by means of π - π^* hyperconjugation. In addition, this class of conjugated polymers shows a good ambipolar charge transport behaviour, as discussed in *paragraph 3.2*.

Substituents can greatly affect the electronic properties of conjugated polymers,^[8,9] other than modifying their processability in organic solvents. Depending on their nature, size and position, substituents can influence the molecular packing of polymer chains, thus greatly affecting charge transport properties of polymer films. So, the effect of lateral-chains on charge carrier mobility of AnE-PVs was investigated.

The electronic properties of conjugated polymers are not simply dependent on their chemical structure but are highly affected by macromolecular parameters, such as molecular weight (*MW*) and polydispersity. Indeed, macromolecular

parameters are known to have great effects on the optical and charge transport properties of conjugated polymer films, also through a different organization of polymer chains in the solid state induced by different *MW*.^[4, 5] A study of the effects of a moderate variation of molecular weight on the transport properties (as well as on the optical, structural, and morphological properties) was conducted for one of the best-performing AnE–PV here considered. The investigation was extended to the photovoltaic performance of the related BHJ solar cells made with [6,6]–phenyl–C₆₁–butyric acid methylester (PCBM) as electron–acceptor.

Another parameter which has a critical role for the transport properties of polymer films is the organization of polymer chains, which can be affected by post–deposition treatments.^[63] The effect of a thermal treatment and of a solvent treatment on charge carrier mobility was also investigated.

3.1 Materials

The chemical structure of the investigated AnE–PVs polymers is shown in *Figure 3.1a*. They are characterized by the same conjugated backbone, but differ in the nature of the grafted solubilising alkoxy side–chains (linear or branched), and were prepared either with well–defined or with randomly distributed side–chains (random polymers). Side–chains and macromolecular parameters (number–average molecular weight, M_n , weight–average molecular weight, M_w , and polydispersity index, *PDI*) of AnE–PVs here investigated, are collected in *Table 3.1*. In the case of AnE–PV–*stat*, three different samples were considered with different macromolecular parameters.

The polymers were synthesized at the Linz Institute for Organic Solar Cells, Johannes Kepler University of Linz, according to procedures already reported in the literature.^[57, 58, 60] Their HOMO/LUMO levels, electrochemically determined, are – 5.09 eV and – 3.04 eV, respectively.^[64]

PCBM was purchased from Sigma–Aldrich.

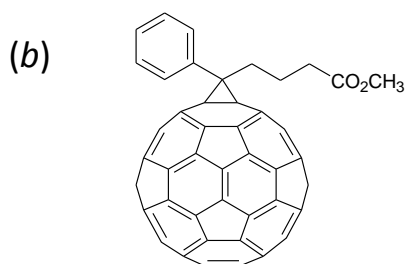
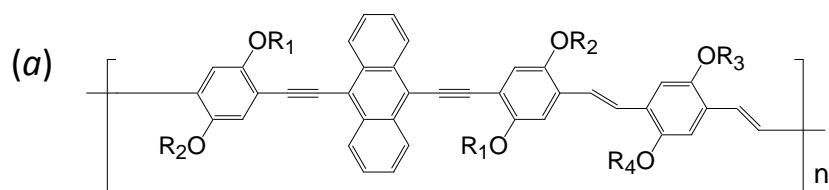


Figure 3.1 Molecular structure of the materials used in this chapter: AnE–PVs (a) and fullerene derivative PCBM (b). R₁–R₄ indicate the lateral chains.

Table 3.1 Side–chains and macromolecular parameters of AnE–PVs here investigated. For the random polymers, the ratio of each side–chain type is indicated in parenthesis.

AnE-PV	Random	Side-chains	M_n (g mol ⁻¹)	M_w (g mol ⁻¹)	<i>PDI</i>
AnE-PV- <i>ab</i>		R1, R2: octyl; R3, R4: 2-ethylhexyl	40000	141600	3.54
AnE-PV- <i>ae</i>		R1, R2: octyl; R3, R4: dodecyl	13300	26200	1.97
AnE-PV- <i>bb</i>		R1 – R4: 2-ethylhexyl	16000	47200	2.98
AnE-PV- <i>stat</i>	AnE-PV- <i>stat-a</i>	R1 – R4: octyl(1) or 2-ethylhexyl(1)	41200	82700	2.01
	AnE-PV- <i>stat-b</i>		18000	43700	2.43
	AnE-PV- <i>stat-c</i>		30600	83900	2.74
AnE-PV- <i>stat4</i>	X	R1, R3: octyl(1) or methyl(1); R2, R4 octyl(1) or 2-ethylhexyl(1)	9100	30030	3.30
AnE-PV- <i>stat5</i>	X	R1, R3: octyl(1) or 2-ethylhexyl(1) or methyl(1); R2, R4: octyl(1) or 2-ethylhexyl(2)	7500	30000	4.00

3.2 Ambipolar behaviour

For the first time, the excellent ambipolar charge transport behaviour of AnE–PVs was reported. The ambipolar transport ability was first demonstrated for AnE–PV–*stat*–a, then confirmed for the other investigated AnE–PVs, as shown in the next paragraphs.

AnE–PV–*stat*–a is capable of both easy oxidation and reduction, as demonstrated by the reversible oxidation and reduction peaks observed in its cyclic voltammogram,^[64] this being a prerequisite for ambipolar transport. A further evidence for ambipolar transport ability was given by the electron–state–distribution of the HOMO/LUMO levels of AnE–PVs, computed by B3LYP/6-31G*^[65] density functional theory, which shows a very good delocalization of both energy levels (*Figure 3.2*).

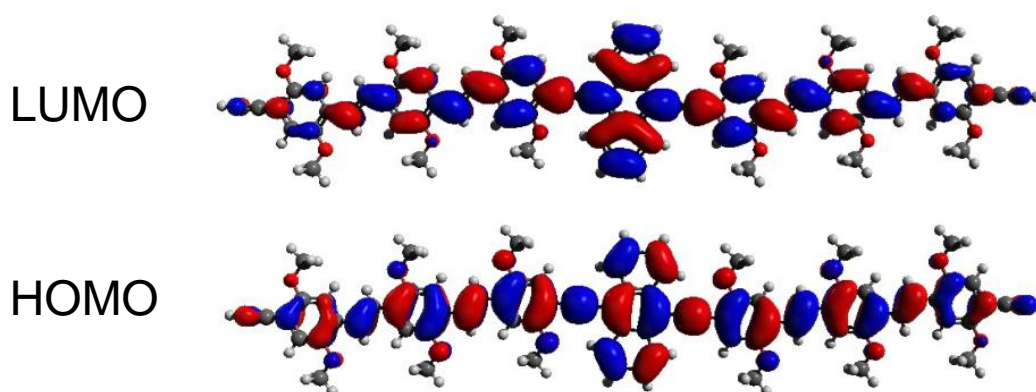


Figure 3.2 HOMO/LUMO electron density plots calculated by B3LYP/6-31G* for the energy–minimized model structure of the methoxy–substituted trimer.

Charge transport was investigated by using the TOF technique. For a better comparison, hole and electron mobility were obtained from TOF measurements made on the same device, with the structure ITO/AnE–PV–*stat*–a/Al (18 nm). The polymer film (3.6 μm thick) was deposited by drop–casting from 1,2–dichlorobenzene solution (30 g L⁻¹).

A typical photocurrent transient for holes is shown in *Figure 3.3a*, for an applied field of 4.2×10^4 V cm⁻¹. Transport of holes is not affected by high dispersion

in cast-films of AnE-PV-*stat-a* and the transit time of carriers can be detected also in a linear scale, mainly at higher fields. The low dispersion of TOF signals is consistent with the multi-crystalline character of this copolymer.^[66] By reversing the polarity of the illuminated semitransparent Al electrode, the signal reported in *Figure 3.3b* was observed for electrons, clearly showing that current due to negative carriers decreases more rapidly and indicating that the time required for electrons to travel through the same sample is much shorter than that for holes.

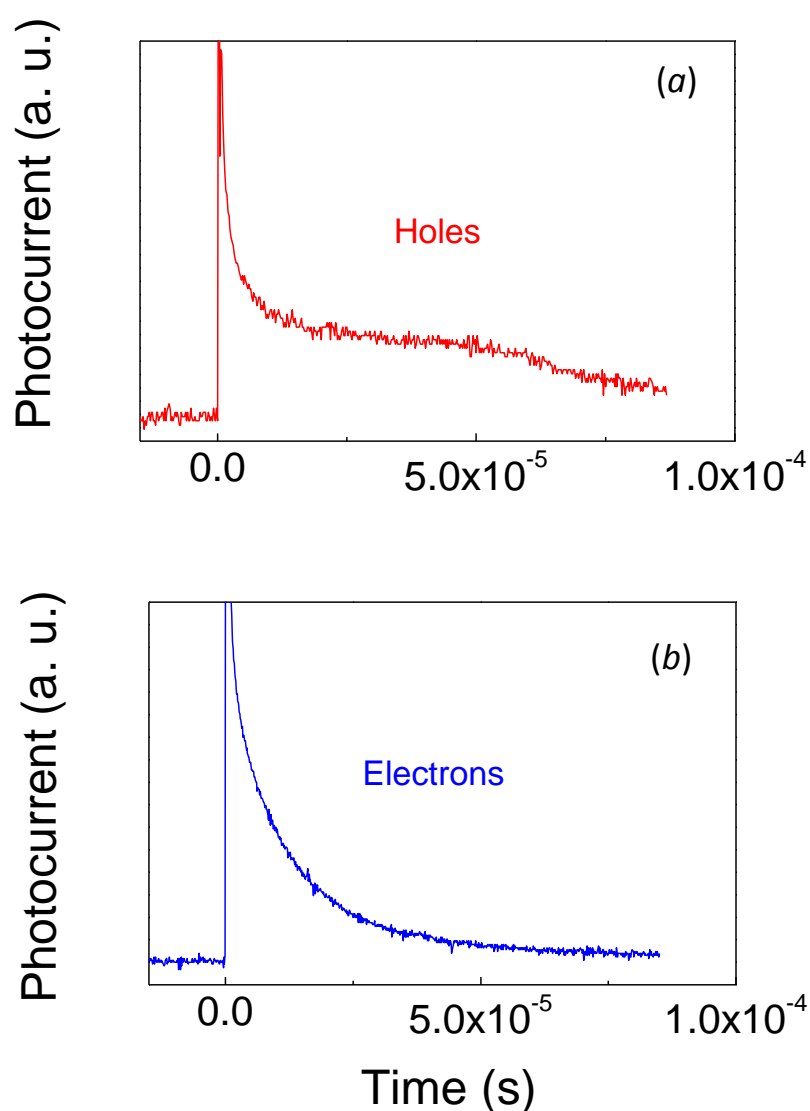


Figure 3.3 Linear plots of photocurrent signals for an ITO/AnE-PV-*stat-a* /Al device with the illuminated semitransparent Al electrode: positively biased (a) and negatively biased (b). In both cases, the applied field was 4.2×10^4 V cm⁻¹.

The comparison of the two signals of *Figure 3.3* confirms the usual finding that transport of electrons is more dispersed than that of positive carriers in conjugated polymers,^[67] commonly attributed to trapping effects. Indeed, with the LUMO level at -3.04 eV,^[62] electron transport states of AnE–PV–stat–a are expected to lie close to the typical impurities acting as trapping states for negative carriers.^[68] However, though the dispersion of photocurrent signals, two different slopes were clearly observed also for electrons in the double–logarithmic representation, as shown in *Figure 3.4*, with slopes far below -1 for times shorter than t_{tr} and much higher than -1 for longer times and whose sum was very close to -2 , as predicted by the Scher–Montroll theory.^[69] Both for electron and hole TOF signals, charge carrier transit times were determined from the intersection point between the two straight lines with different slopes.

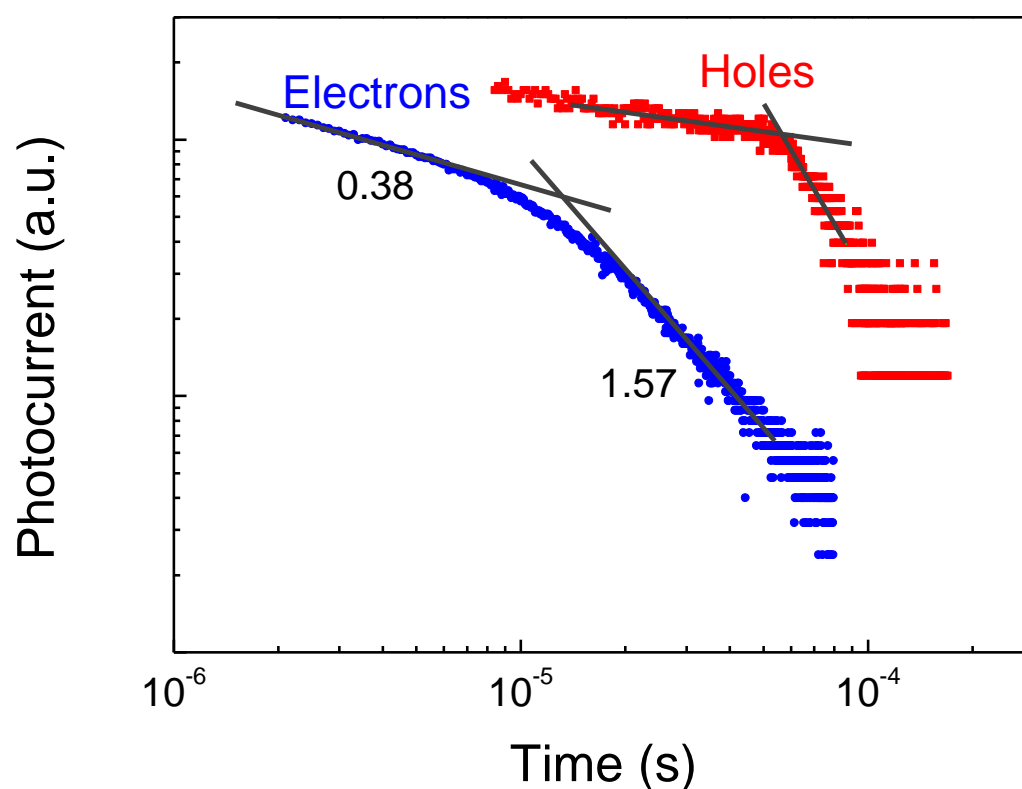


Figure 3.4 The same signals of *Figure 3.3* shown in a double–logarithmic scale. The values of the slopes before and after the transit time are also indicated in the case of electrons.

The values of charge carrier mobility were calculated through the well-known expression of Equation 2.4, and are plotted as a function of the square-root of E in Figure 3.5.

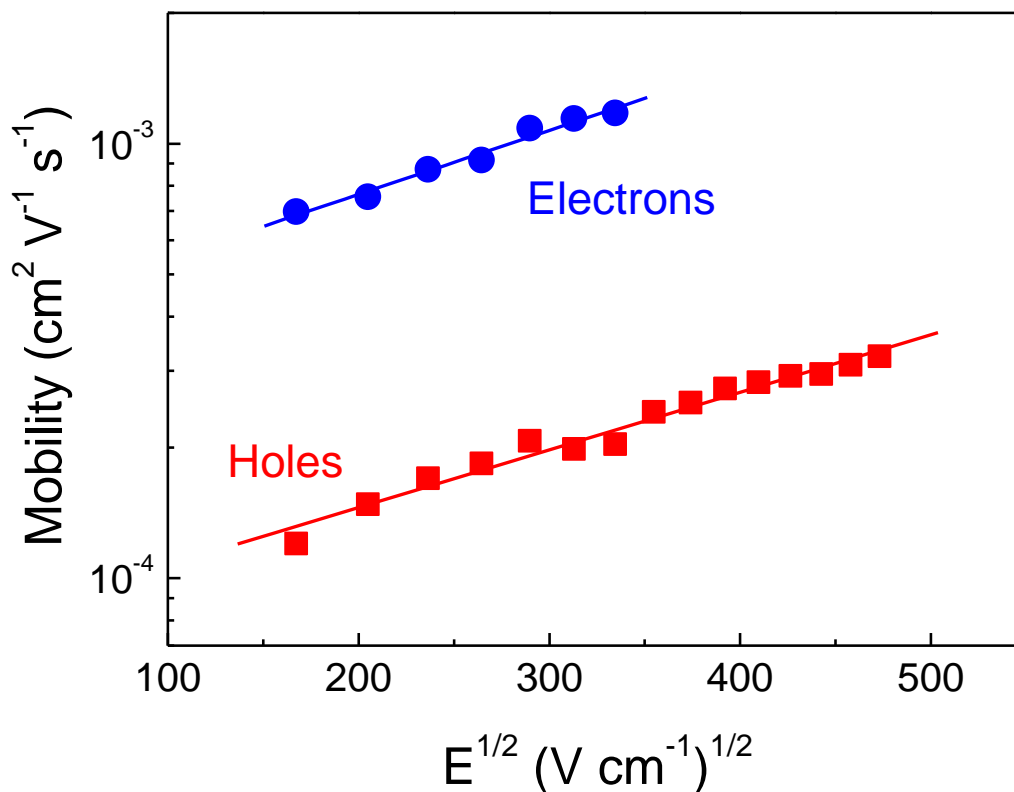


Figure 3.5 Room-temperature TOF mobility as a function of the square-root of field for an as-cast AnE-PV-*stat*-a film 3.6 μm thick. The lines indicate the linear fit to the experimental data.

Differently from other good ambipolar conjugated polymers already reported in the literature, the bulk electron mobility (μ_e) in as-cast AnE-PV-*stat*-a films is roughly six times higher than hole mobility (μ_h) in the investigated range of field. For example, at the same field of $1.1 \times 10^5 \text{ V cm}^{-1}$, an electron mobility of $1.2 \times 10^{-3} \text{ cm}^2 \text{V}^{-1} \text{s}^{-1}$ was calculated, against $2.0 \times 10^{-4} \text{ cm}^2 \text{V}^{-1} \text{s}^{-1}$ for holes. Both for electron and hole mobility, a good linear trend of μ with $E^{1/2}$ was obtained (Figure 3.5), indicating a Poole-Frenkel behaviour (Equation 1.1). Such a behaviour has been frequently observed in organic materials and could be attributed to the effects of energetic and positional disorder on the hopping conduction in disordered molecular solids.^[18] The parameters for the Poole-Frenkel fit to mobility data of

Figure 3.5 are $\mu_{0e} = 3.9 \times 10^{-4} \text{ cm}^2 \text{ V}^{-1} \text{ s}^{-1}$ and $\gamma = 3.4 \times 10^{-3} (\text{V cm}^{-1})^{-1/2}$ for electrons and $\mu_{0h} = 7.9 \times 10^{-5} \text{ cm}^2 \text{ V}^{-1} \text{ s}^{-1}$ and $\gamma = 3.1 \times 10^{-3} (\text{V cm}^{-1})^{-1/2}$ for holes. The values of γ are rather usual for conjugated polymers and indicate a moderate field-dependence of charge carrier mobility in AnE-PV-*stat*-a. That of electron mobility is however a bit stronger than that for holes, consistent with increased/different trapping processes.^[70]

3.3 Effect of side-chains

The investigation of hole and electron mobility by TOF was extended to the other five AnE-PVs with different side-chains (*Table 3.1*).

Given that transport of charge carriers is highly affected by the organization of polymers chains in the solid state,^[71, 72] the same conditions (solvent, deposition method, post-deposition treatment) were used for the deposition of all polymer films, that is those already described in *paragraph 3.2* for AnE-PV-*stat*-a. The thickness of the polymer layers was 9.4, 1.4, 2.9, 7.0 and 15.5 μm for AnE-PV-*ab*, AnE-PV-*ae*, AnE-PV-*bb*, AnE-PV-*stat4*, and AnE-PV-*stat5*, respectively.

Typical photocurrent transients, both for holes and electrons, are displayed in *Figure 3.6* in a double-logarithmic representation and for a comparable applied electric field of about $1 \times 10^5 \text{ V cm}^{-1}$. The inspection of *Figures 3.6a–3.6f* indicates that all AnE-PVs investigated show an ambipolar charge transport, though much more dispersed for negative carriers.

By plotting the logarithm of mobility as a function of the square-root of E , a good linear trend was obtained in most cases, as shown in *Figure 3.7*. The parameters obtained from the Poole-Frenkel fit to mobility data of *Figure 3.7* are collected in *Table 3.2*.

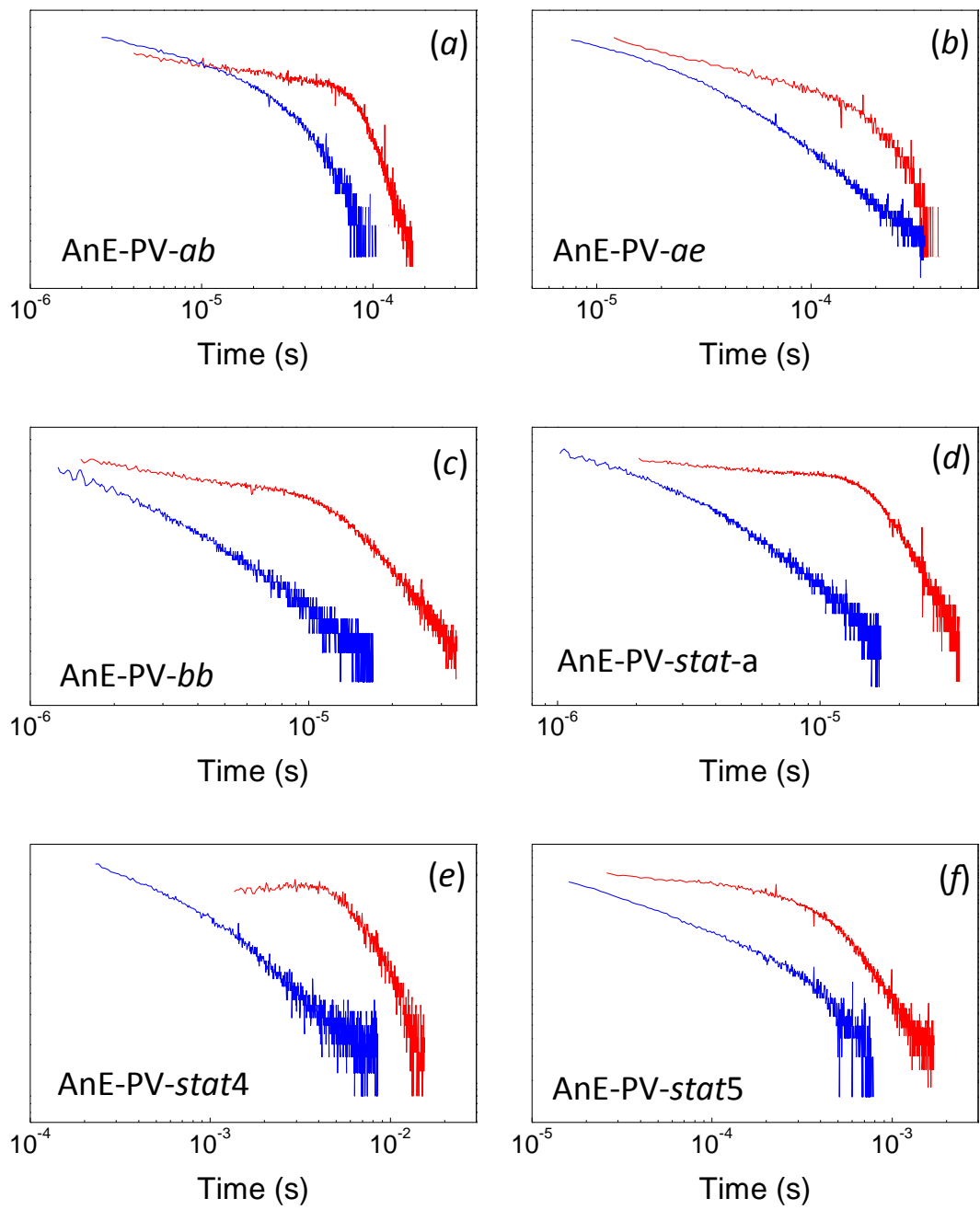


Figure 3.6 Typical TOF signals in log–log scales for an applied electric field of about $1 \times 10^5 \text{ V cm}^{-1}$. Positive carriers (red lines) and negative carriers (blue lines).

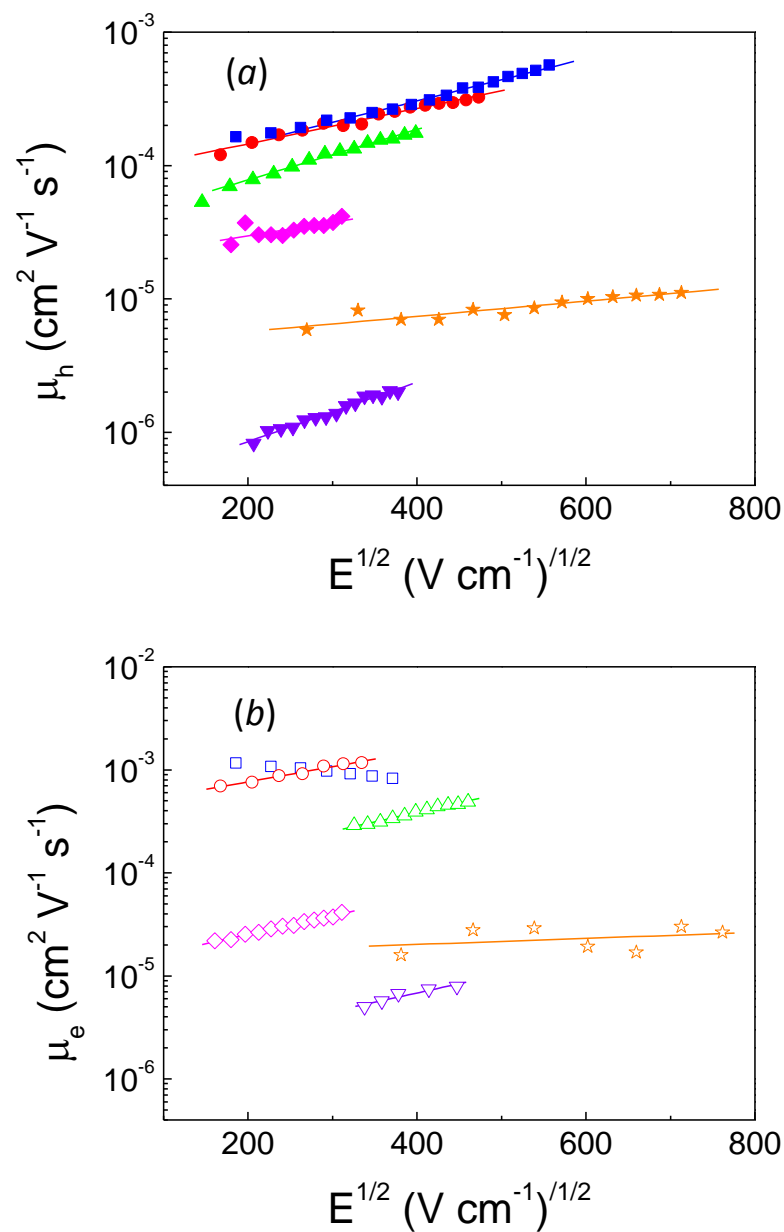


Figure 3.7 Hole mobility (filled symbol) (a) and electron mobility (open symbol) (b) as a function of the square-root of the electric field for: AnE-PV-*ab* (green up triangles); AnE-PV-*ae* (orange stars); AnE-PV-*bb* (blue squares); AnE-PV-*stat-a* (red circles); AnE-PV-*stat4* (violet down triangles); AnE-PV-*stat5* (magenta diamonds). The lines are the linear fit to the experimental data.

Table 3.2. Summary of mobility data: hole and electron mobility for an applied electric field of about $1 \times 10^5 \text{ V cm}^{-1}$, zero-field mobility and Poole-Frenkel for holes and electrons.

AnE-PV	<i>ab</i>	<i>ae</i>	<i>bb</i>	<i>stat-a</i>	<i>stat4</i>	<i>stat5</i>
Side-chains	octyl, 2-ethylhexyl	octyl, dodecyl	2- ethylhexyl	octyl, 2-ethylhexyl octyl	2- ethylhexyl, methyl	octyl, 2- ethylhexyl, methyl
μ_h ($\text{cm}^2 \text{ V}^{-1} \text{ s}^{-1}$)	1.3×10^{-4}	8.2×10^{-6}	2.3×10^{-4}	2.0×10^{-4}	1.6×10^{-6}	4.0×10^{-5}
μ_{0h} ($\text{cm}^2 \text{ V}^{-1} \text{ s}^{-1}$)	3.3×10^{-5}	3.8×10^{-6}	7.9×10^{-5}	7.9×10^{-5}	3.0×10^{-7}	1.3×10^{-5}
γ_h (V cm^{-1}) ^{-1/2}	4.3×10^{-3}	1.6×10^{-3}	3.4×10^{-3}	3.1×10^{-3}	5.1×10^{-3}	3.6×10^{-3}
μ_e ($\text{cm}^2 \text{ V}^{-1} \text{ s}^{-1}$)	2.9×10^{-4}	1.6×10^{-5}	9.1×10^{-4}	1.2×10^{-3}	5.0×10^{-6}	4.1×10^{-5}
μ_{0e} ($\text{cm}^2 \text{ V}^{-1} \text{ s}^{-1}$)	6.7×10^{-5}	1.5×10^{-5}	n.a.	3.9×10^{-4}	1.3×10^{-6}	1.1×10^{-5}
γ_e (V cm^{-1}) ^{-1/2}	4.4×10^{-3}	6.7×10^{-4}	n.a.	3.4×10^{-3}	4.1×10^{-3}	4.2×10^{-3}

The only decreasing trend with E was observed for electron mobility, in AnE-PV-*bb* films (Figure 3.7b). However, both the Poole-Frenkel-like trend of mobility, and a decreasing trend of μ with E can be explained within the same model of an hopping conduction, as demonstrated by Monte Carlo simulations.^[73, 74]

The data of Figure 3.7 and Table 3.2 clearly show the great effect of lateral chains on charge carrier mobility of AnE-PVs, with μ varying by two orders of magnitude both for holes (ranging between 1.6×10^{-6} and $2.3 \times 10^{-4} \text{ cm}^2 \text{ V}^{-1} \text{ s}^{-1}$ for E of about 10^5 V cm^{-1}) and electrons (between 5.0×10^{-6} and $1.2 \times 10^{-3} \text{ cm}^2 \text{ V}^{-1} \text{ s}^{-1}$ for the same field). As expected, the polymer with the longest substituents (AnE-PV-*ae*, with octyl and dodecyl chains) shows low mobility compared with the other ones, consistent with the reduction of the electronic interaction between conjugated backbones as the extension of lateral chains increases.^[75, 76] This is also confirmed by

the comparison between AnE–PV–*ab* and AnE–PV–*bb*, only differing for the octyl side–chains. The latter, with only 2–ethylexyl substituents, shows higher mobility values (2.3×10^{-4} against $1.3 \times 10^{-4} \text{ cm}^2 \text{ V}^{-1} \text{ s}^{-1}$ for holes, 9.1×10^{-4} against $2.9 \times 10^{-4} \text{ cm}^2 \text{ V}^{-1} \text{ s}^{-1}$ for electrons, for field of about 10^5 V cm^{-1}). However, the most striking difference of AnE–PV–*ae*, compared with the other polymers, is represented by the low dependence of mobility on electric field, as demonstrated by the lowest values of γ (*Table 3.2*). This could be due to a lower energetic disorder^[77] in the fluctuation of the energy of the hopping sites for charge transport, which could be attributed to a more ordered arrangement of polymer chains in the film. Indeed, a layered structure consisting of π – π stacked backbones has been already reported for films made of AnE–PVs with all–linear side chains attached close to the anthracenylene–ethynylene unit, in contrast to the more amorphous structure of polymers with branched lateral chains attached to the same backbone^[66]. The other five polymers, all bearing branched 2–ethylhexyl chains, show a γ value ranging between 3.1×10^{-3} and $5.1 \times 10^{-3} \text{ cm}^{1/2} \text{ V}^{-1/2}$, without a clear trend with the molecular structure.

The comparison between statistical and non–statistical polymers can be done by considering AnE–PV–*ab* and AnE–PV–*stat*–*a*, bearing the same octyl and 2–ethylhexyl side–chains. Better values both for mobility and γ were obtained for the polymer with lateral chains statistically distributed, confirming the superior features of the random polymer compared to the counterpart based on well–defined side–chain.^[64] Finally, looking at the data of *Table 3.2*, it is surprising the difference of roughly one order of magnitude between the mobility values of AnE–PV–*stat*4 and AnE–PV–*stat*5, two random polymers with the same side–chains and just differing for the different amount of short methyl chains. The former, with more methyl groups in the molecular structure (*Table 3.1*), shows lower values compared with AnE–PV–*stat*5, as well as the lowest one for the six considered polymers, indicating that the short methyl chains have a detrimental effect on the transport properties of charge carriers.

It is worth noting that the two polymers with methyl side–chains are among the ones exhibiting the lowest mobilities (*Figure 3.7* and *Table 3.2*) of the six considered,

confirming that the shortest lateral chains prevent a favourable organization of polymer films for the transport of charge carriers. To support this hypothesis, the X-Ray Diffraction (XRD) pattern of AnE–PV–*stat4* film is compared to that of AnE–PV–*stat-a*, without methyl chains and showing very good mobility values. The polymer films, prepared in the same conditions used for mobility investigation, showed very different XRD patterns (*Figure 3.8*).

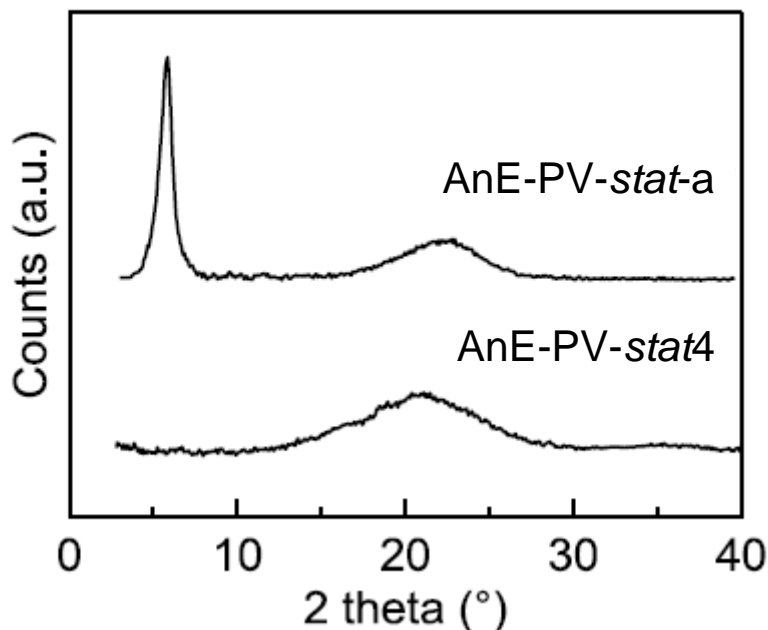


Figure 3.8 XRD spectra for AnE–PV–*stat-a* and AnE–PV–*stat4* films deposited onto zero–background quartz.

Differently from AnE–PV–*stat-a*, showing a semicrystalline character, AnE–PV–*stat4* reveals its complete amorphous feature. Indeed, AnE–PV–*stat-a* sample shows a crystalline peak at 5.53° (2θ), corresponding to a staking interlayer distance of 1.53 nm, while only a bell–shaped profile is visible in the wide angle region of the XRD pattern of AnE–PV–*stat4*, also present in the pattern of AnE–PV–*stat-a* and related to the amorphous component of the investigated films. Likely, the short methyl side–chains, reducing the overall rough symmetry of the repeating unit, could hinder the possibility of a regular stacking of the polymer main chains. This leads to a very different organization in the solid state and highly affects the charge transport properties of the films made with the two different polymers, with a variation of two orders of magnitude in the mobility values. It is important to

underline that also the photophysical properties of the two statistical polymers are greatly influenced, with AnE–PV–stat–a showing improved absorption and emission spectra compared to the amorphous AnE–PV–stat4.^[58]

The very different transport properties of AnE–PV–stat–a and AnE–PV–stat4 could be also attributed to a different extent of charge trapping processes. In this case, a different trend of charge carrier transit times with the applied electric field should be observed. It has been shown that, in a multiple trapping model, the transit time of charge carriers exhibits the following electric field dependence^[78]

$$t_{tr}(E) \propto E^{-1/\alpha} \quad (3.1)$$

where α is a dispersion parameter ($0 < \alpha < 1$; $\alpha = 1$ for non dispersive transport) introduced by Scher and Montroll^[79] in their model for the description of dispersive transport in amorphous solids. The electric field dependence of transit times derived from the TOF measurements are reported in *Figure 3.9* for AnE–PV–stat–a and AnE–PV–stat4.

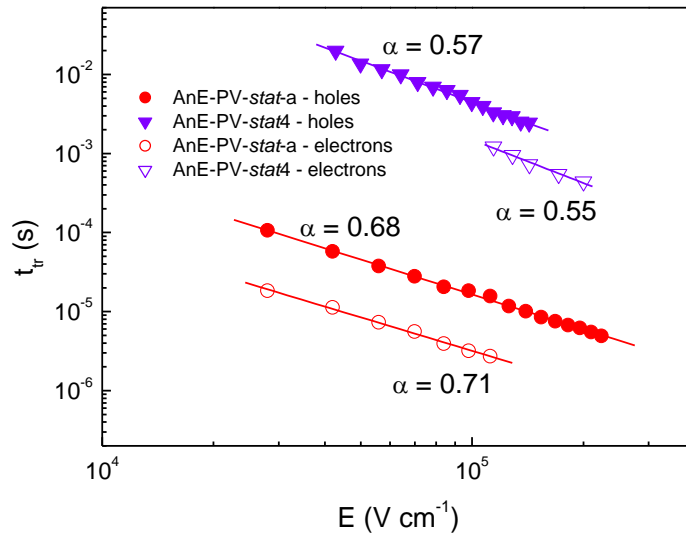


Figure 3.9 Transit time of holes (filled symbols) and electrons (open symbols) as a function of the electric field for AnE–PV–stat–a (red circles) and AnE–PV–stat4 (violet down triangles).

From the slope of the lines representing the linear fit to the experimental data, the values of the dispersion parameter were extracted. 0.57 and 0.55 were obtained for AnE–PV–*stat*4, for holes and electrons respectively, compared with the expected higher values for α of 0.68 (holes) and 0.71 (electrons) calculated for AnE–PV–*stat*–a and indicating that charge transport is less affected by charge trapping events in this latter polymer.

3.4 Effect of solvent and thermal treatments

The effect of a solvent and of a thermal treatment on the transport of positive charge carriers in films made of AnE–PV–*stat*–a and AnE–PV–*stat*–c, was investigated by AS using the experimental conditions described in *paragraph 2.1.3*.

In the case of AnE–PV–*stat*–a, the conductance, very low for $V_{bias} = 0$ V, increased by 4 orders of magnitude by increasing the bias (*Figure 3.10*), both in as–cast and solvent annealed samples. A small dip in the conductance spectra was observed for as–cast sample in the intermediate frequency range (10^4 – 10^5 Hz), shifting to higher frequencies for higher values of V_{bias} . These features, more evident in the solvent–annealed sample, are an indication of the occurrence of charge injection.

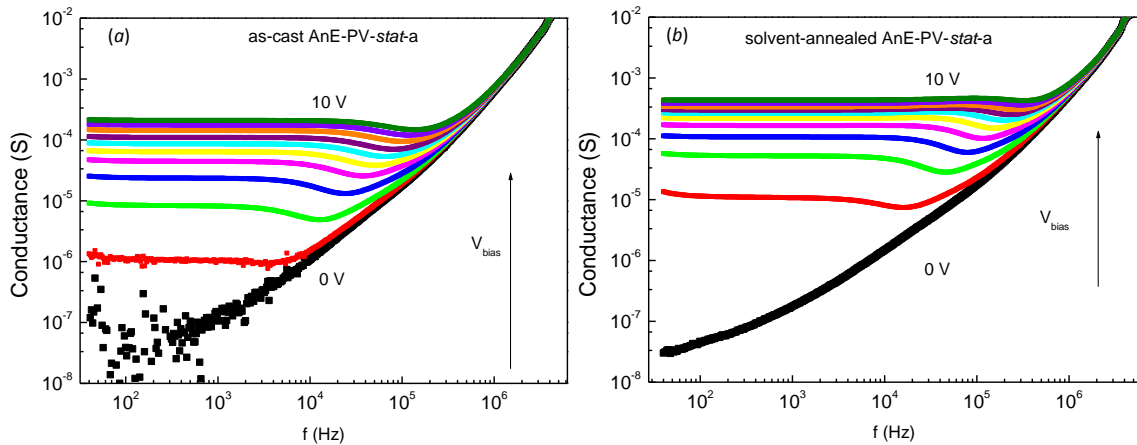


Figure 3.10 Frequency dependence of conductance for as–cast (a) and solvent–annealed (b) AnE–PV–*stat*–a films, for V_{bias} values in the range 0–10 V with a step of 1 V. The arrow indicates the direction of increasing V_{bias} .

The typical minima in the capacitance spectra were observed (Figure 3.11), allowing for the construction of the plots of the negative differential susceptance, shown in Figure 3.12.

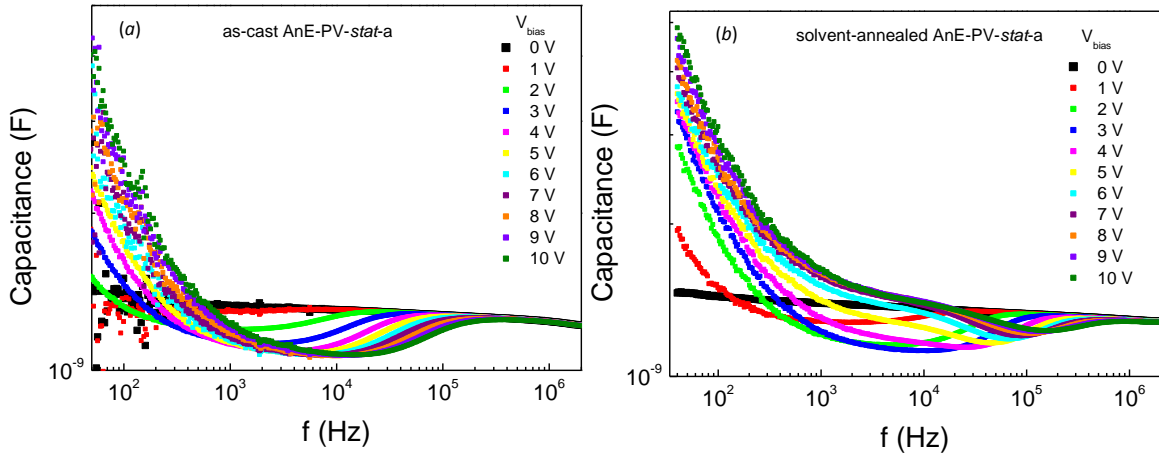


Figure 3.11 Frequency dependence of capacitance for as-cast (a) and solvent-annealed (b) AnE-PV-stat-a films.

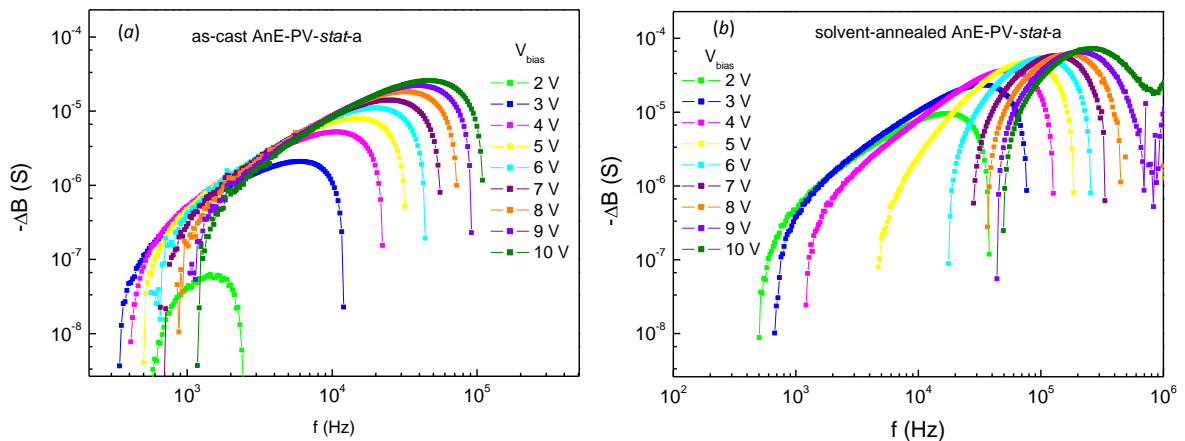


Figure 3.12 Variation in the negative susceptance with frequency for as-cast (a) and solvent-annealed (b) AnE-PV-stat-a films.

By increasing V_{bias} , $-\Delta B$ peaks increase and shift towards higher frequencies, as expected, but more significantly for the as-cast device. This indicates a lower field dependence of hole mobility for the solvent-annealed sample, likely due to a more ordered arrangement of polymer chains upon solvent annealing.

The frequency dependence of conductance, capacitance and $-\Delta B$ for AnE-PV-stat-c films, as-cast or thermal annealed, are shown in Figures 3.13, 3.14

and 3.15, respectively. Again, a variation of the spectra was observed between the as-cast and the treated (thermal-annealed) film, with an unclear dependence of $-\Delta B$ peaks on V_{bias} for the as-cast sample.

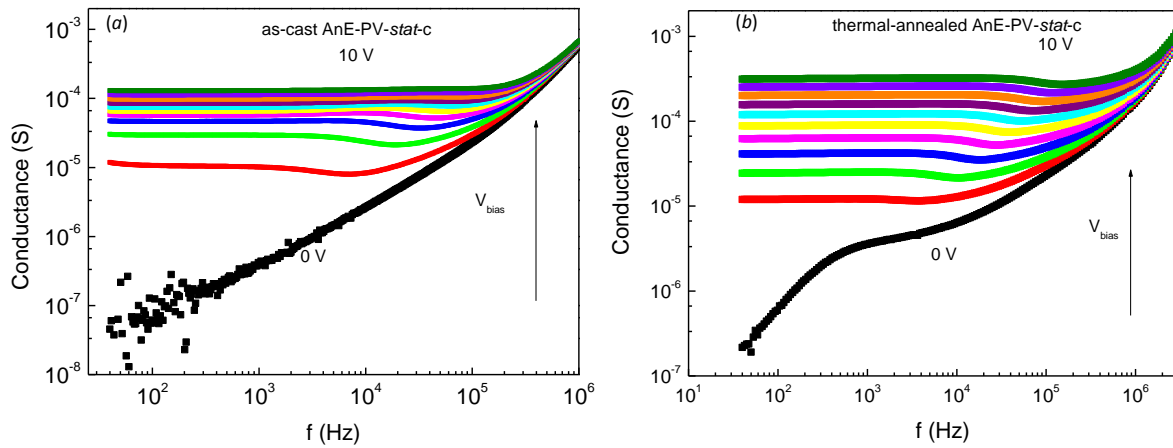


Figure 3.13 Frequency dependence of conductance for as-cast (a) and thermal-annealed (b) AnE-PV-stat-c films, for V_{bias} values in the range 0–10 V with a step of 1 V. The arrow indicates the direction of increasing V_{bias} .

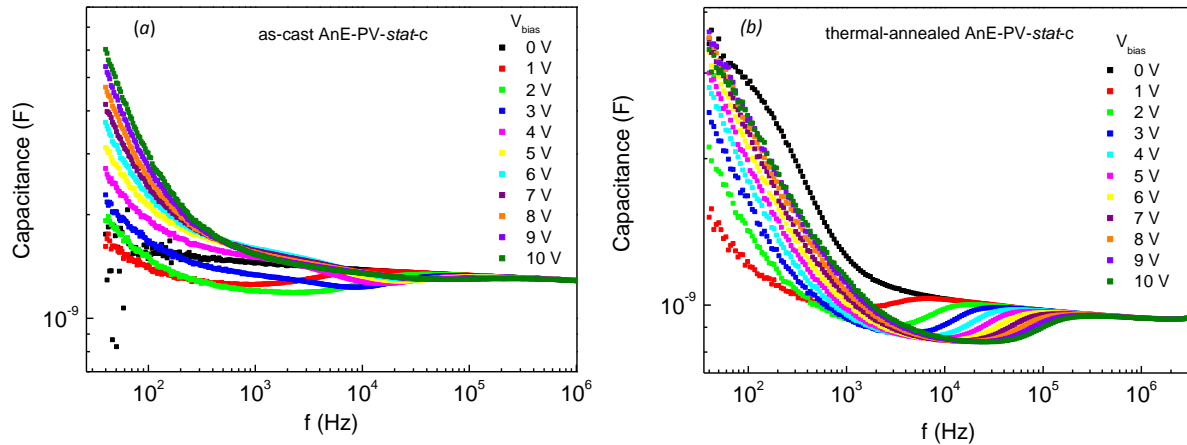


Figure 3.14 Frequency dependence of capacitance for as-cast (a) and thermal-annealed (b) AnE-PV-stat-c films.

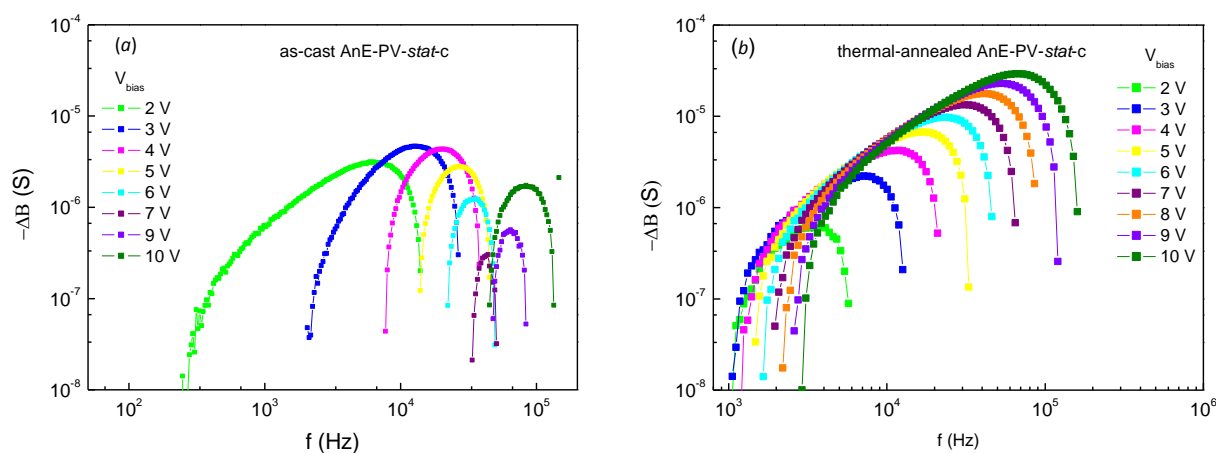


Figure 3.15 Variation in the negative susceptance with frequency for as-cast (a) and thermal-annealed (b) AnE-PV-stat-c films.

The values of the transit time of holes were extracted from the frequencies corresponding to the $-\Delta B$ peaks, as described in *paragraph 2.1.3*, and hole mobility was calculated by using the well-known expression (equation 1.1).

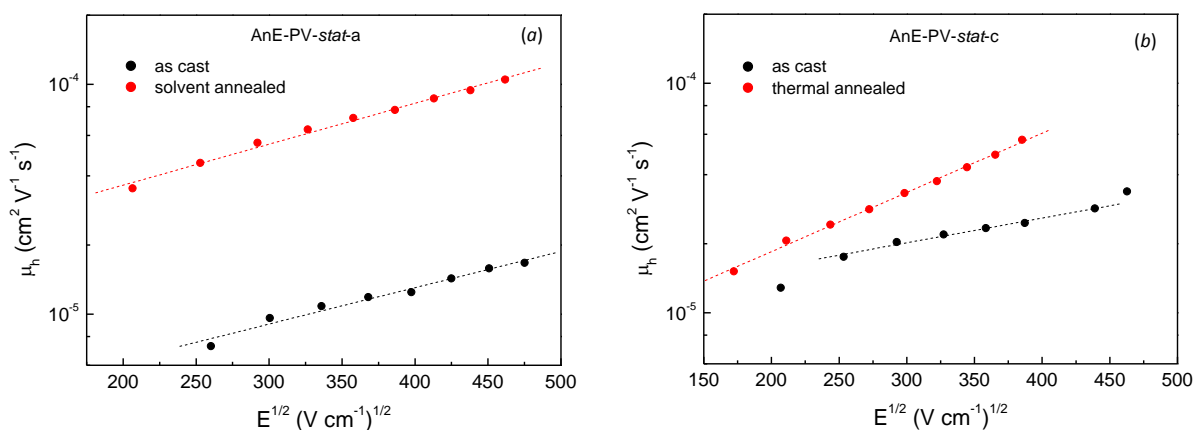


Figure 3.16 Dependence of hole mobility on the square-root of the electric field for as-cast and solvent-annealed AnE-PV-stat-a (a) and as-cast and thermal-annealed AnE-PV-stat-c (b) films. The dotted lines represent the linear fit to the experimental data.

As shown in *Figure 3.13*, the mobility data plotted against the square-root of the electric field, show a linear trend, suggesting a Poole-Frenkel behaviour for all the devices here considered. The parameters extracted from the Poole-Frenkel are collected in *Table 3.3*.

Table 3.3 Poole-Frenkel parameters for AnE-PV-*stat-a* and AnE-PV-*stat-c* samples and mobility values calculated for a field of 10^5 V cm^{-1} .

Polymer	Treatment	μ_{0h} ($\text{cm}^2\text{V}^{-1}\text{s}^{-1}$)	γ_h (V cm^{-1}) ^{1/2}	$\mu_h @ 10^5 \text{ V cm}^{-1}$ ($\text{cm}^2\text{V}^{-1}\text{s}^{-1}$)
AnE-PV- <i>stat-a</i>	as-cast	3.04×10^{-6}	3.64×10^{-3}	9.61×10^{-6}
	solvent-annealed	1.75×10^{-5}	3.84×10^{-3}	5.89×10^{-5}
AnE-PV- <i>stat-c</i>	as-cast	7.65×10^{-6}	3.09×10^{-3}	2.01×10^{-5}
	thermal-annealed	5.64×10^{-6}	5.94×10^{-3}	3.69×10^{-5}

Solvent and thermal annealing enhance the mobility of holes in AnE-PV-*stat-a* and AnE-PV-*stat-c* films spin-coated from chloroform solutions, likely due to an enhanced order upon annealing. Looking at the data of Table 3.3, it is worth noting that the mobility at zero field decreased and the Poole-Frenkel factor increased upon thermal-annealing AnE-PV-*stat-c* polymer film. In order to shed light on the origin of the variations observed in the transport of holes, AnE-PV-*stat-c* and AnE-PV-*stat-a* films, prepared and treated in the same conditions used for admittance spectroscopy, were investigated by XRD (Figure 3.17).

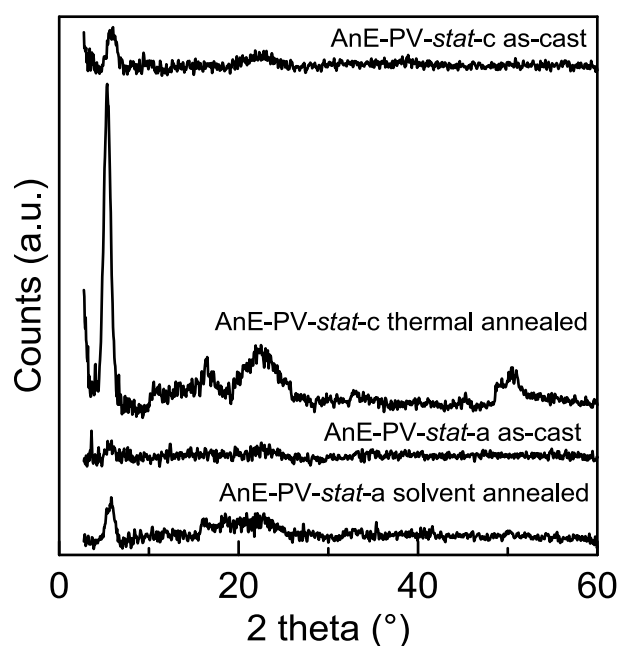


Figure 3.17 XRD spectra for AnE-PV-*stat-a* and AnE-PV-*stat-c* films deposited onto zero-background quartz.

In both cases the XRD profiles of the annealed samples suggest an increase in the molecular organization, but only in the case of thermal-annealed AnE–PV–*stat*–c sample the order is meaningful. We can appreciate an intense peak at 5.4° ($d=1.64\text{nm}$), two very low at 10.8° and 16.5° (0.82 and 0.54 nm) and a broad ‘bump’ centred around 22.6°. The peaks are due to the first, second and third order of a 1.64 nm periodicity due to chain–chain interlayer distance. The broad halo is caused by the disordered stacking of the chains within the main chain layers. For samples AnE–PV–*stat*–c as–cast and AnE–PV–*stat*–a solvent–annealed, only the reflection at about 5.8° is detected with low intensity, suggesting a low fraction of ordered material.

In summary, as-cast films from chloroform solutions are characterized by a low order degree, enhanced, as expected, by annealing. The thermal–annealed AnE–PV–*stat*–c sample shows the highest order degree, though does not exhibit the highest mobility. Indeed, though the significant difference of the XRD patterns of annealed AnE–PV–*stat*–c and AnE–PV–*stat*–a films, the highest mobility was calculated for the less ordered solvent–annealed AnE–PV–*stat*–a. In addition, the stronger field activation of mobility observed for thermal-annealed AnE–PV–*stat*–c could indicate a hole transport limited by the grain boundaries of a multi–crystalline structure, often observed for this class of polymers.^[66]

AnE–PV–*stat*–a and AnE–PV–*stat*–c polymer samples mainly differ for PDI, the weight average molecular weight being comparable (*Table 3.1*). Therefore, the light differences observed for charge transport in the two polymer samples could be due to their polydispersity, affecting the arrangement of polymer chains in the solid state. The role of PDI for the film organization, as well as for charge transport, will be confirmed in the next *paragraph*.

3.5 Effect of a fine variation of the macromolecular parameters

Three AnE–PV–*stat* polymer samples were considered, differing for the macromolecular parameters, denoted AnE–PV–*stat*–a, AnE–PV–*stat*–b, AnE–PV–*stat*–c (*Table 3.1*). The weight–average molecular weight (43700 g mol^{-1}) of AnE–PV–*stat*–b was nearly two times lower than that determined for

AnE–PV–*stat*–a (82400 g mol⁻¹) and AnE–PV–*stat*–c (83200 g mol⁻¹). In addition, as shown by the gel permeation chromatography (GPC) curves (Figure 3.18), AnE–PV–*stat*–c exhibited a broader M_w distribution compared with AnE–PV–*stat*–a.

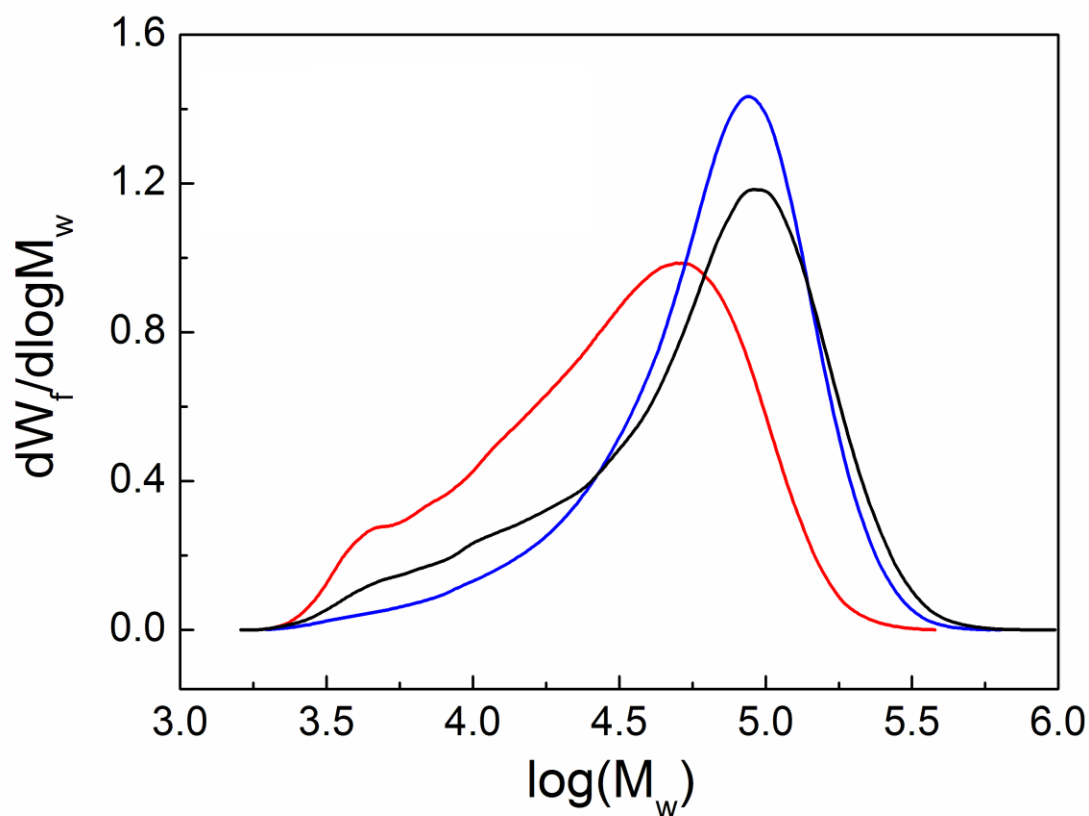


Figure 3.18 GPC curves of the three AnE–PV–*stat* samples: AnE–PV–*stat*–a (blue), AnE–PV–*stat*–b (red) and AnE–PV–*stat*–c (black).

3.5.1 Effect on the optical properties

The optical properties of the three AnE–PV–*stat* samples were investigated by UV–Vis absorption and photoluminescence (PL) spectroscopy, both in diluted solutions (chloroform, concentration between 3×10^{-7} mol L⁻¹ and 1×10^{-6} mol L⁻¹) and in thin films (55 nm) spin–coated onto quartz substrate from chlorobenzene (10 g L⁻¹) solutions.

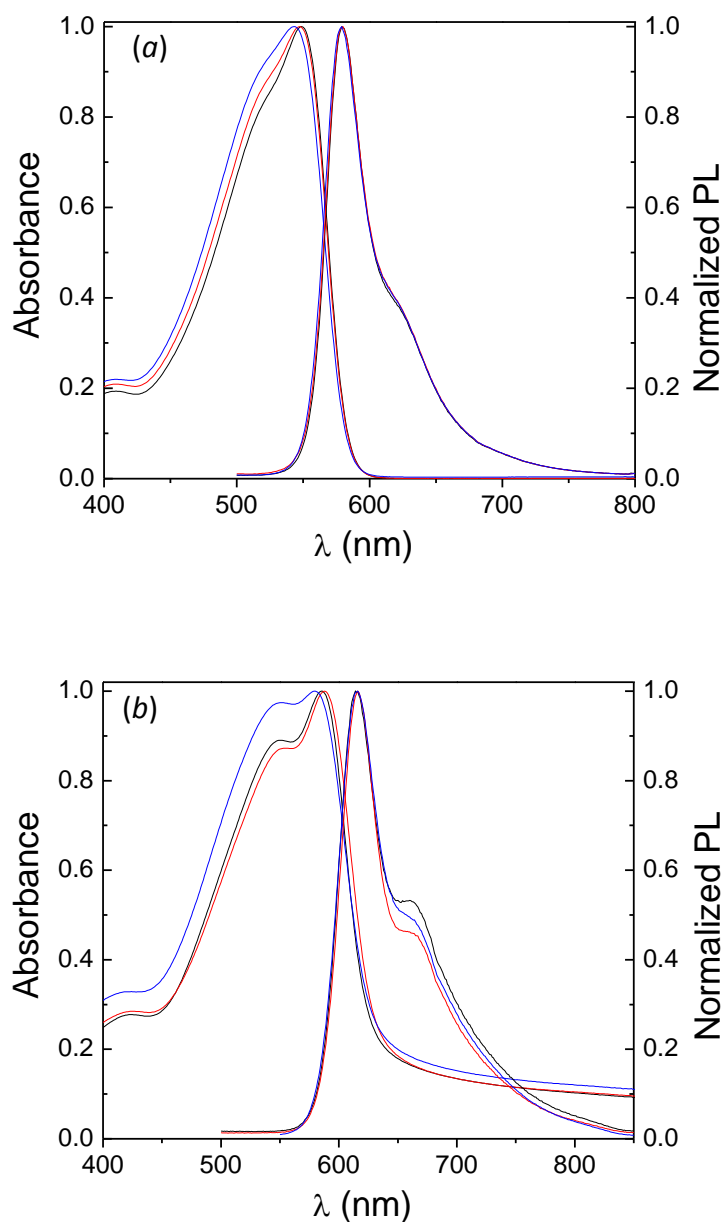


Figure 3.19 Absorption (left) and photoluminescence (right) spectra in normalized scales of dilute solutions (a) and thin films (b) of the same thickness (55 nm) spin-coated onto quartz substrate of the three AnE–PV–*stat* samples: AnE–PV–*stat*–a (blue), AnE–PV–*stat*–b (red) and AnE–PV–*stat*–c (black). The excitation wavelength was 400 nm for solutions and 450 nm for films.

As expected, no meaningful differences were observed in the optical spectra of dilute solutions (*Figure 3.19*), showing the same spectral features already reported for AnE–PV–*stat* polymers,^[64] with the same emission peak position (579 nm) and very close absorption maxima at 543, 547 and 548 nm for AnE–PV–*stat*–a,

AnE–PV–*stat*–b and AnE–PV–*stat*–c, respectively. Films of AnE–PV–*stat* spin–cast from chlorobenzene solution are known to show a stacking behaviour,^[64] resulting in structured absorption and photoluminescence spectra exhibiting two peaks, as shown in *Figure 3.19*, for the AnE–PV–*stat* samples here investigated. Given the narrow molar mass range for the three polymer samples, significant variations of the optical spectra were not observed, nevertheless some considerations can be made.

The main difference in the absorption spectra of films is between AnE–PV–*stat*–a and the other two samples, the former showing the lower energy peak slightly blue–shifted (located at 588 nm, against 586 and 579 nm for samples AnE–PV–*stat*–c, and AnE–PV–*stat*–b, respectively), indicating a moderate reduction of the effective conjugation, and a different relative intensity of the two absorption peaks (*Figure 3.19b*). These features should not be related to *MW*, given the comparable molecular weight of AnE–PV–*stat*–a and AnE–PV–*stat*–c, and could indicate a different molecular organization in the solid state due to the different polydispersity (*Table 3.1*). Indeed the lower and higher energy absorption peaks have been attributed to the formation of H and J aggregate formation, respectively^[62, 64, 80] so the spectrum of AnE–PV–*stat*–a seems to suggest a more balanced contribution of H– and J–type aggregations, the latter being in any case predominant for all the investigated samples.

Concerning the PL spectra, somewhat different emission capability were observed by films showing a comparable absorbance at the excitation wavelength of 450 nm (*Figure 3.19b*), qualitatively indicating the highest luminescence quantum yield for AnE–PV–*stat*–a and the lowest for AnE–PV–*stat*–c. Again this behaviour can be related to a different strength of π – π inter–chain interactions in the three samples, leading to a quenching of emission.^[62]

3.5.2 Effect on the structural and morphological properties

The preliminary indications on the solid state organization of the three samples were confirmed by XRD experiments, conducted on films drop–cast from chlorobenzene solutions. The diffraction patterns shown in *Figure 3.20* are

characterized by a sharp intense reflection at low angle, due to interlayer staking, and by a wide band with no resolved peaks at high angle.

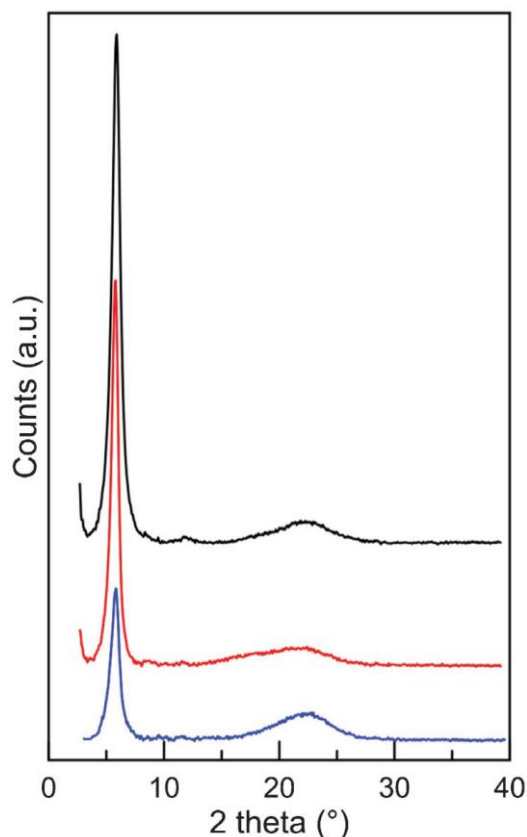


Figure 3.20 XRD patterns of films AnE–PV–stat–a (blue lines); AnE–PV–stat–b (red lines); AnE–PV–stat–c (black lines) drop–cast from chlorobenzene solutions onto zero–background quartz holder.

A low intensity second order peak is also detectable on the profile of AnE–PV–stat–c sample at 11.8° (2θ). The distance between the planes (d_i) shows only a slight variation in the three polymer samples (Table 3.4), with a modest lengthening by lowering the molar mass. On the contrary, the domain length seems to be strongly dependent on M_n and M_w . Indeed, AnE–PV–stat–b sample, characterized by the lowest molecular mass parameters, displays an increase of the mean domain length (L) of about 30% with respect to the other samples and a corresponding increase of the number of lattice planes per domain ($n_i = L/d_i$). A rough evaluation of the ratio of the area of the main peak to that the overall area under the XRD profile suggests that the overall order degree of the investigated

polymer films follows the order: AnE–PV–*stat*–c > AnE–PV–*stat*–b > AnE–PV–*stat*–a. However, if the number of lattice planes per domain is considered, AnE–PV–*stat*–b results in the sample with the largest ordered domains. The comparison of the XRD patterns of samples AnE–PV–*stat*–c and AnE–PV–*stat*–a, roughly showing the same peak in the GPC curves but different *PDI*, suggests that polydispersity plays an important role in the organization of polymer chains.

Table 3.4. XRD parameters of the three AnE–PV–*stat* samples: interlayer distance, peak width *FWHM*, mean domain length and mean number of interlayer lattice per domain.

Donors	d_i (nm)	<i>FWHM</i> (°, 2 θ)	<i>L</i> (nm)	n_i
AnE-PV- <i>stat</i> -a	1.52	0.86	10.3	6.8
AnE-PV- <i>stat</i> -b	1.53	0.67	13.2	8.6
AnE-PV- <i>stat</i> -a	1.50	0.84	10.5	7.0

The atomic force microscopy (AFM) inspection of films deposited in the same conditions used for the XRD investigation revealed a close correlation between the macromolecular parameters and the film topology (Figure 3.21). Polymer chains in AnE–PV–*stat*–b film, with the lowest M_w , were able to pack in smaller domains, compared with the samples with higher molar mass, while a prevailing fibril-like formation was observed for samples AnE–PV–*stat*–a and AnE–PV–*stat*–c. The smaller-domain morphology of AnE–PV–*stat*–b film was also accomplished by a higher root-mean-square roughness (R_q), compared to the films made of the polymers with higher molar weight. The values of R_q evaluated on a scan area of 0.5 $\mu\text{m} \times 0.5 \mu\text{m}$ were 0.71, 1.58 and 1.34 nm for AnE–PV–*stat*–a, AnE–PV–*stat*–b and AnE–PV–*stat*–c, respectively, and maintained the same trend over a larger scan area of 1.0 $\mu\text{m} \times 1.0 \mu\text{m}$. By comparing AnE–PV–*stat*–c and AnE–PV–*stat*–a, exhibiting a similar M_w , the lower R_q was observed for the one showing the lower polydispersity, indicating that the distribution of molecular weights plays a role in the film morphology.

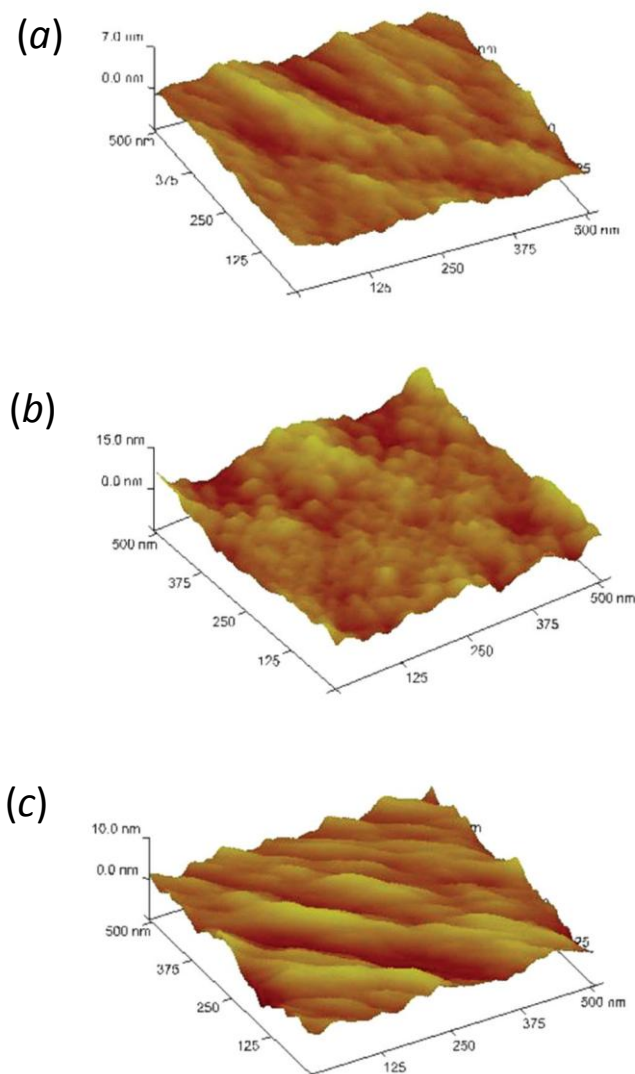


Figure 3.21 Three-dimensional AFM topography images of drop-casted films made of: AnE-PV-stat-a (a); AnE-PV-stat-b (b); AnE-PV-stat-c (c).

The comparison of *Figure 3.21a* and *3.21c* shows the effect of the different polydispersity index on the film morphology. Indeed, the higher *PDI* of AnE-PV-stat-c seems to be beneficial for a more regular arrangement of polymer chains, confirming the XRD data, and as previously suggested for poly(3-alkylthiophenes).^[81]

3.5.3 Effect on charge carrier mobility

TOF experiments were carried out in the same conditions described in *paragraph 3.2*. The polymer layers were drop-casted from the same chlorobenzene solutions used for the preparation of the XRD and AFM samples. The film thickness was 3.6, 4.2, 7.8 μm for AnE-PV-*stat-a*, AnE-PV-*stat-b* and AnE-PV-*stat-c*, respectively.

The photocurrent transients for the three AnE-PV-*stat* samples are displayed in a double-logarithmic representation in *Figure 3.22* for a comparable electric field of about $1 \times 10^5 \text{ V cm}^{-1}$.

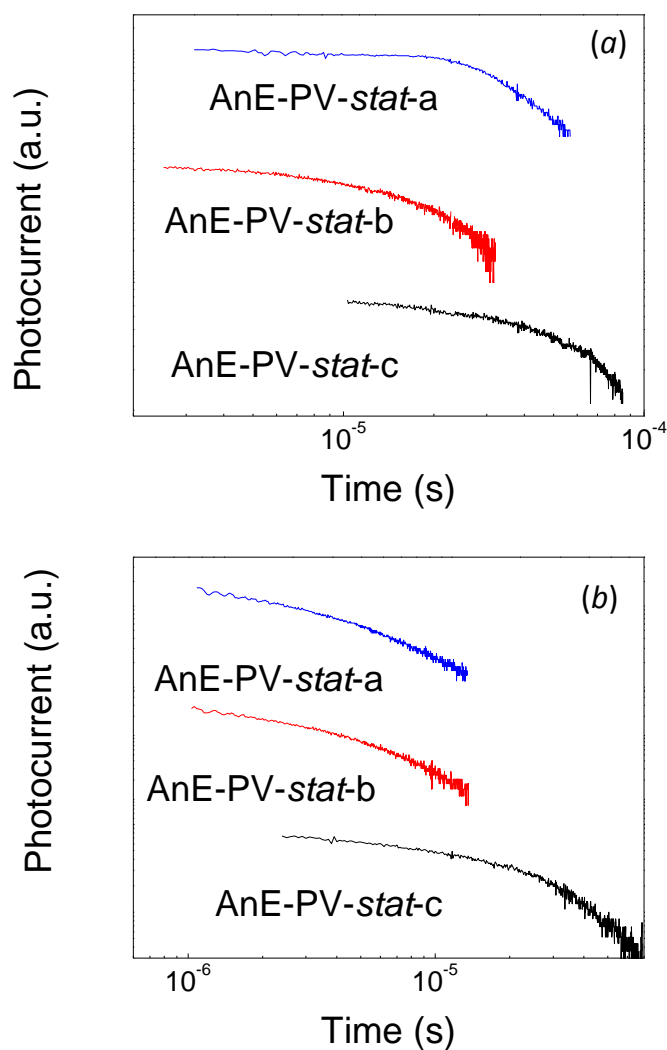


Figure 3.22 Log-log plots of photocurrent signals for holes (a) and electrons (b) for a comparable electric field of about $1 \times 10^5 \text{ V cm}^{-1}$.

The shape of TOF signals shown in *Figure 3.22* is representative for transients observed for different values of E and indicates a quite dispersive transport. The resulting values for charge carrier mobility are shown as a function of the applied field in *Figure 3.23*.

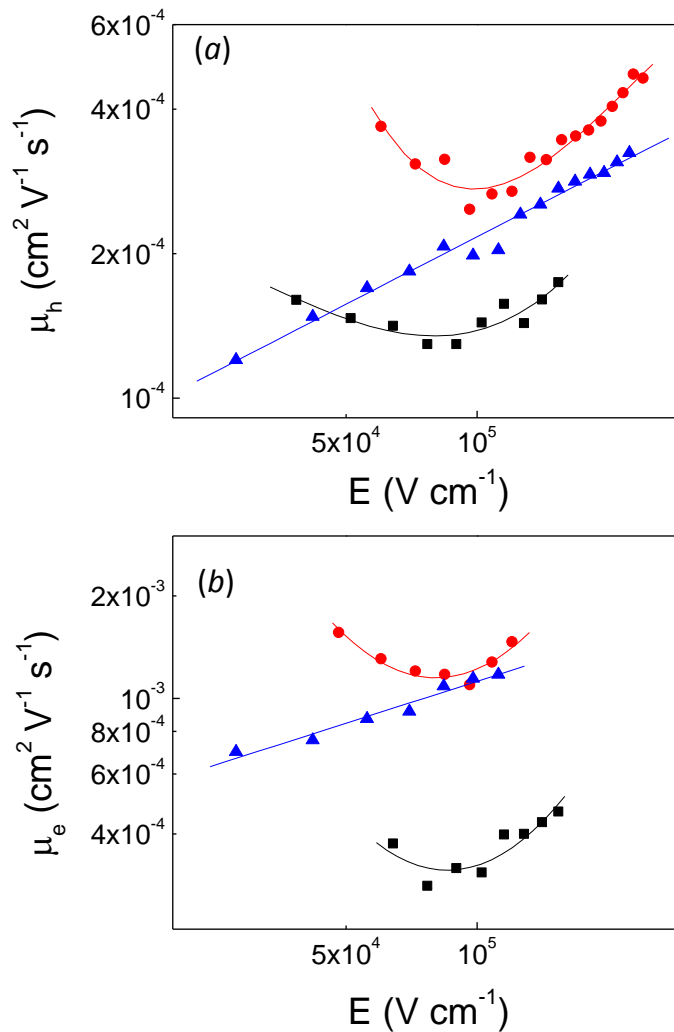


Figure 3.23 Hole (a) and electron (b) drift mobility as a function of the applied electric field: AnE–PV–stat–a (blue triangles); AnE–PV–stat–b (red circles); AnE–PV–stat–c (black squares). Lines are shown to guide the eye.

As far as the trend of μ with E is concerned, being the same for both positive and negative carriers for each AnE–PV–stat sample, again the main difference was observed between AnE–PV–stat–a and the other two polymer samples, both showing a higher overall degree of order as observed with XRD. It has already been

reported in *paragraph 3.2* that charge carrier mobility in AnE–PV–*stat*–a films shows a Poole–Frenkel behaviour both for holes and electrons,^[82] with an exponential increase of μ with the square–root of E .

Differently, mobility in AnE–PV–*stat*–c and AnE–PV–*stat*–b films exhibits a decreasing trend for low fields and reaches a minimum before starting increasing with E . For both types of carriers, drift mobility shows a clear dependence on the macromolecular parameters. At low fields (below $5 \times 10^4 \text{ V cm}^{-1}$), the hole mobility seems to be correlated to the mean domain length (*Table 3.4*), with more ordered polymer samples showing higher mobility. However hole mobility in sample AnE–PV–*stat*–a surpasses that in sample AnE–PV–*stat*–c as E is increased, because of the strong field activation of the less ordered polymer also at moderate electric fields.

3.5.4 Effect on the performance of BHJ solar cells

Bulk heterojunction solar cells were prepared with the three AnE–PV–*stat* samples, as electron–donors and PCBM as acceptor. Since, for a given D/A pair, the maximum photovoltaic performance of the related blends is determined by a critical interplay between different factors, such as miscibility, deposition conditions, blend thickness, donor to acceptor ratio, pre – and/or post–treatments,^[83] the comparison of different D/A pairs is not so straightforward. For this reason the aim of this work was not the optimization of solar cell devices, but to establish how the photovoltaic properties of AnE–PV–*stat*:PCBM blends were affected when an organization of the donor phase close to that of drop–casted thick films investigated by TOF, XRD and AFM was induced. To this end, efforts were made to use deposition and treatment conditions able to induce such organization in spin–coated thin films, required for lab–scale solar cell preparation. The AnE–PV–*stat*:PCBM active layers were deposited by using a not too high D/A ratio (1:1 w/w), the same solvent (chlorobenzene), the same solution concentration (17 g L^{-1}), the same low rotation speed of the spin–coater (500 rpm). After the deposition, the AnE–PV–*stat*:PCBM films were solvent–vapour annealed for one hour, in order to foster the polymer

chain organization through the slow-drying process. The structure of solar cells was completed with a LiF/Al cathode.

The photovoltaic parameters of solar cells based on the three donors are collected in *Table 3.5*, along with the thickness of the active layers, while the related *J-V* characteristics are displayed in *Figure 3.24*.

Table 3.5 Active layer thickness and photovoltaic parameters (AM1.5G, 100 mW cm⁻²) of solar cells made with the three AnE-PV-*stat* donors and PCBM acceptor in 1:1 weight ratio.

Donors	<i>d</i> nm	<i>J</i> _{sc} (mA cm ⁻²)	<i>V</i> _{oc} (V)	<i>FF</i>	<i>η</i> (%)
AnE-PV- <i>stat</i> -a	93	3.82	0.89	0.51	1.73
AnE-PV- <i>stat</i> -b	130	5.57	0.87	0.67	3.26
AnE-PV- <i>stat</i> -a	135	6.10	0.85	0.46	2.38

A straight comparison can be done for the same active layer thickness. Solar cells made with AnE-PV-*stat*-c show a slightly higher short-circuit current with respect to those with AnE-PV-*stat*-b donor, which could arise from an increased D/A interface, leading to a slightly higher generation of charge carriers. This could be due to a more intimate mixing with the PCBM moiety because of the longer polymer chains of AnE-PV-*stat*-c.

However, the striking difference in the photovoltaic parameters of the two kinds of cells is given by fill factor, raising from 0.46 for AnE-PV-*stat*-c to 0.67 for AnE-PV-*stat*-b, giving a strong indication of very different transport properties in the blends and confirming the mobility data of pristine donors.

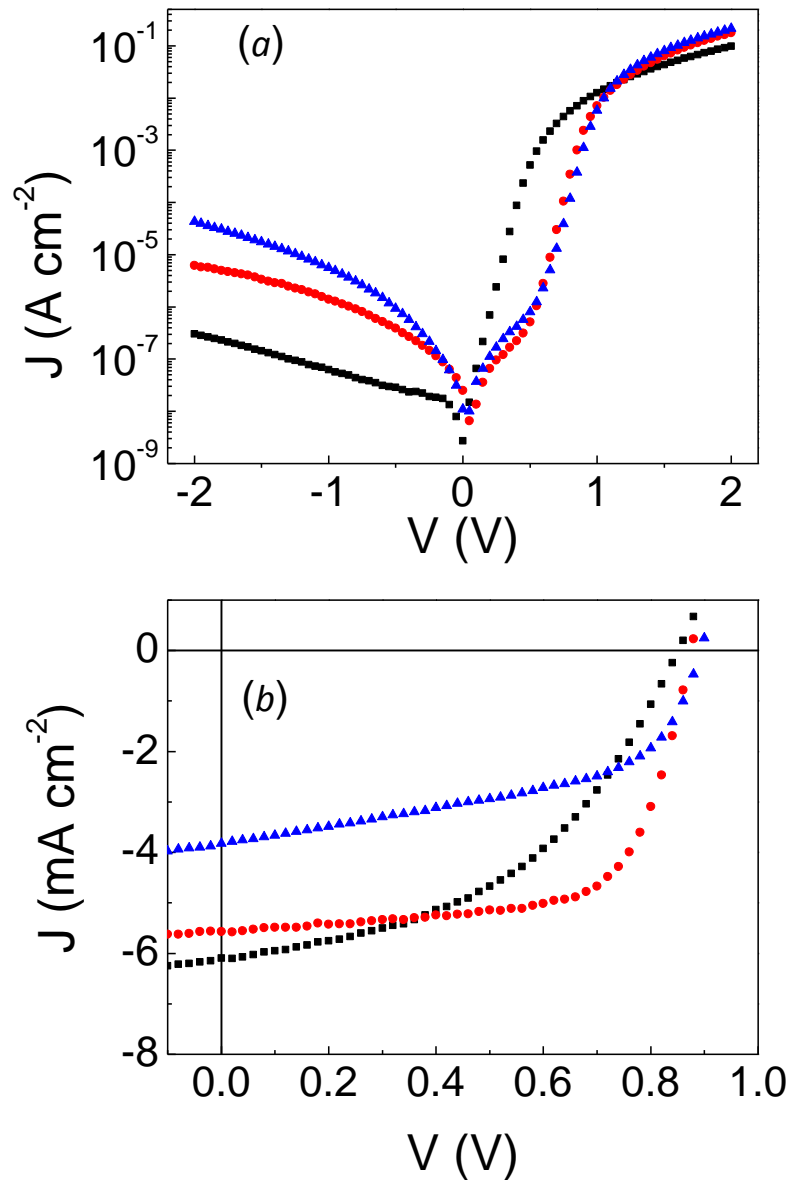


Figure 3.24 Current density–voltage characteristics in the dark (a) and under 100 mWcm^{-2} illumination (b) for solar cells made with the three electron–donors: AnE–PV–stat–a (blue triangles); AnE–PV–stat–b (red circles); AnE–PV–stat–c (black squares)

As expected,^[84] the open–circuit voltage was not meaningfully affected by the donor component (Table 3.5) and the enhanced FF of AnE–PV–stat–b based cells led to a power conversion efficiency of 3.26%, to be compared with 2.38% of AnE–PV–stat–c based cells. Concerning AnE–PV–stat–a donor, J_{sc} , thus η , can hardly be compared with the values observed for the other solar cells, because of the reduced active layer thickness. However, some consideration can be done on fill factor, which,

differently from J_{sc} , is not affected by the lower solar light harvesting ability of cells made with AnE–PV–stat–a donor. Fill factor of AnE–PV–stat–a cells was found to be 0.51, in between those shown by the other cells, again confirming the trend of hole mobility in pristine AnE–PV–stat films (Figure 3.23a). Figure 3.25 shows the straight correlation between fill factor of solar cells and the mobility of positive carriers measured in pristine AnE–PV–stat films at a field of about $1 \times 10^5 \text{ V cm}^{-1}$.

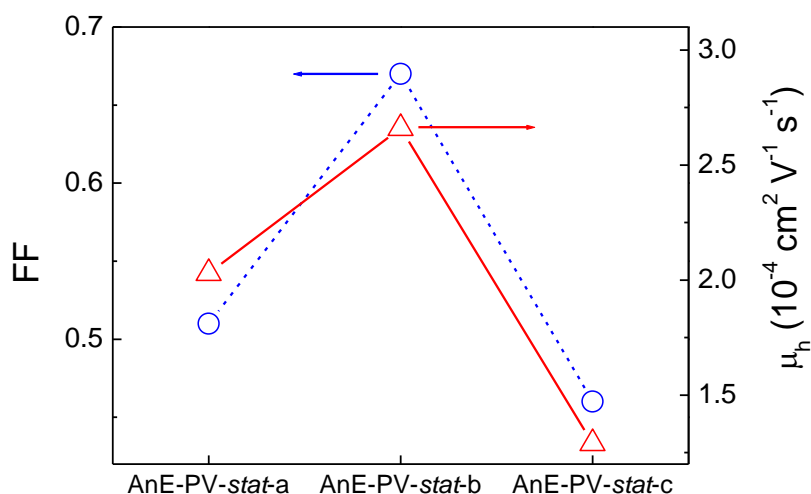


Figure 3.25 Fill factor of AnE–PV–stat:PCBM solar cells (left, blue circles) and TOF hole mobility, at about $1 \times 10^5 \text{ V}^{-1} \text{ cm}^{-1}$, of pristine AnE–PV–stat films (right, red triangles)

3.6 Discussion

A systematic investigation of charge carrier mobility in films made of a series of anthracene–containing poly (p–phenylene–ethynylene)–alt–poly(p–phenylene–vinylene)s, bearing the same conjugated backbone, has been performed, in order to establish the relationship between charge transport properties and (i) molecular structure, (ii) macromolecular parameters, and (iii) deposition conditions for this relevant class of conjugated polymers.

For the first time, we demonstrated the excellent ambipolar behaviour of this class of conjugated polymers, which could be interesting for field–effect transistor application. Indeed, AnE–PV polymers show a very good delocalization of HOMO and LUMO levels, consistent with a good ability to transport both positive and

negative charge carriers. In addition, differently from other good ambipolar conjugated polymers already reported in the literature, the bulk transport of negative carriers is even faster than that of positive carriers, with a drift mobility of fastest electrons of about six times higher than that evaluated for fastest holes in the case of the best-performing AnE–PV investigated. These results suggest that conjugated polymers with carbon–carbon triple bonds, rarely considered and investigated, could represent a promising platform toward high performance ambipolar materials for printable and plastic electronics.

For AnE–PV–*stat* we have also studied the effects of a slight variation of the macromolecular parameters on its transport properties, as well as on the related organic solar cells by using PCBM as electron–acceptor. Interestingly, a variation of just a factor of around two in the molecular weight of AnE–PV–*stat* led to appreciable modifications in the optical, morphological, and transport properties of its films, reflecting in the behaviour of AnE–PV–*stat*:PCBM solar cells. Not only the mobility data were affected by the macromolecular parameters, but also the trend of μ with the applied electric field was found to be dependent on them. A Poole–Frenkel–like behaviour was obtained for less ordered AnE–PV–*stat*–a films, while a minimum of μ at around $1 \times 10^5 \text{ V}^{-1} \text{ cm}^{-1}$ was observed for the other two polymer samples giving more ordered arrangements in cast–films. The comparison of AnE–PV–*stat*–a and AnE–PV–*stat*–c, showing the same peak in the GPC curves but different *PDI*, indicated that polydispersity plays a significant role in the organization of polymer chains in the investigated films, thus affecting all their properties. In addition, a strong correlation between the fill factor of AnE–PV–*stat*:PCBM solar cells and the mobility of pristine AnE–PV–*stat* films was obtained, suggesting that the tuning of the donor macromolecular parameters is critical for high performance polymer/fullerene solar cells.

By changing the side–chains of AnE–PVs, relevant differences in charge transport properties were observed for both positive and negative carriers. Indeed the nature of the substituents has a great impact on charge carrier mobility of the investigated polymers, with a variation observed of 2–3 orders of magnitude. Long octyl and dodecyl linear chains have a detrimental effect on μ , likely because of a less compact molecular packing, resulting in a decreased interaction between

adjacent hopping sites. Similarly, short methyl substituents induce low mobility values, but because of a highly disordered arrangement of polymer chains in the solid phase, also leading to an increased charge trapping. Indeed, a decreasing mobility with the amount of methyl chains in the molecular structure was clearly observed. Finally, the used experimental conditions, allowing for a straight comparison of the investigated films, definitely confirmed the better properties of random polymers, compared to the counterpart based on well-defined side-chain.

CHAPTER 4 – CHARGE TRANSPORT IN SOLAR CELLS MADE OF BAND GAP CONJUGATED POLYMERS AND NEAT-C₇₀

In this chapter, the effects of charge transport in BHJ solar cells, made of blends between low band gap conjugated polymers (electron–donors) and neat–fullerenes (electron–acceptors), are investigated.

Low cost, both of active materials and processing techniques for module production, is one of the main advantages of this innovative photovoltaic technology: the aim of this work, carried out within an industrial research project on organic solar cell, is to give a contribution to further restrain the costs of materials. The approach of this thesis is the replacement of the common soluble derivatives of fullerene with neat fullerenes (C₆₀ and C₇₀), much less soluble^[85] but with a cost one–tenth that of functionalized fullerenes. C₇₀ was preferred to C₆₀, because of its moderate absorption in the visible range.^[86]

The use of a third component, a pyrene derivative, was also considered for a better dispersion of the poorly soluble C₇₀ in the polymer matrix.

4.1. Materials

A copolymer based on poly(2,7–carbazole) derivatives, poly(N–9''–hepta–decanyl–2,7–carbazole–alt–5,5–(4',7'–di–2–thienyl–2',1',3'–benzothiadiazole) (PCDTBT) and a copolymer made of thiophene and benzodithiophene, thieno[3,4–b]–thiophene/benzodithiophene (PTB7, Luminescence Technology Corp.) were used as electron–donors.

In addition to solar cells made of neat–C₇₀, reference devices were prepared with [6,6]–phenyl C₇₁–butyric acid methyl ester (PC₇₀BM) as acceptor. Both electron–acceptors were purchased by Sigma–Aldrich.

In order to obtain a better dispersion of C₇₀, a third component, butyl 1–pyrenebutyrate (PyBB) was introduced in the blends.

PCDTBT and PyBB were synthesized at the Research Center for non Conventional Energies, Istituto ENI Donegani, ENI S.p.A. PCDTBT was synthesized according to a previously reported method^[87] while PyBB was prepared through a simple reaction of esterification with 1-butanol, starting from the commercial 1-pyrenebutyric acid in the presence of catalytic amount of H₂SO₄. All materials were used as received. *Figure 4.1* shows the molecular structure and the energy levels of the materials used in this chapter.

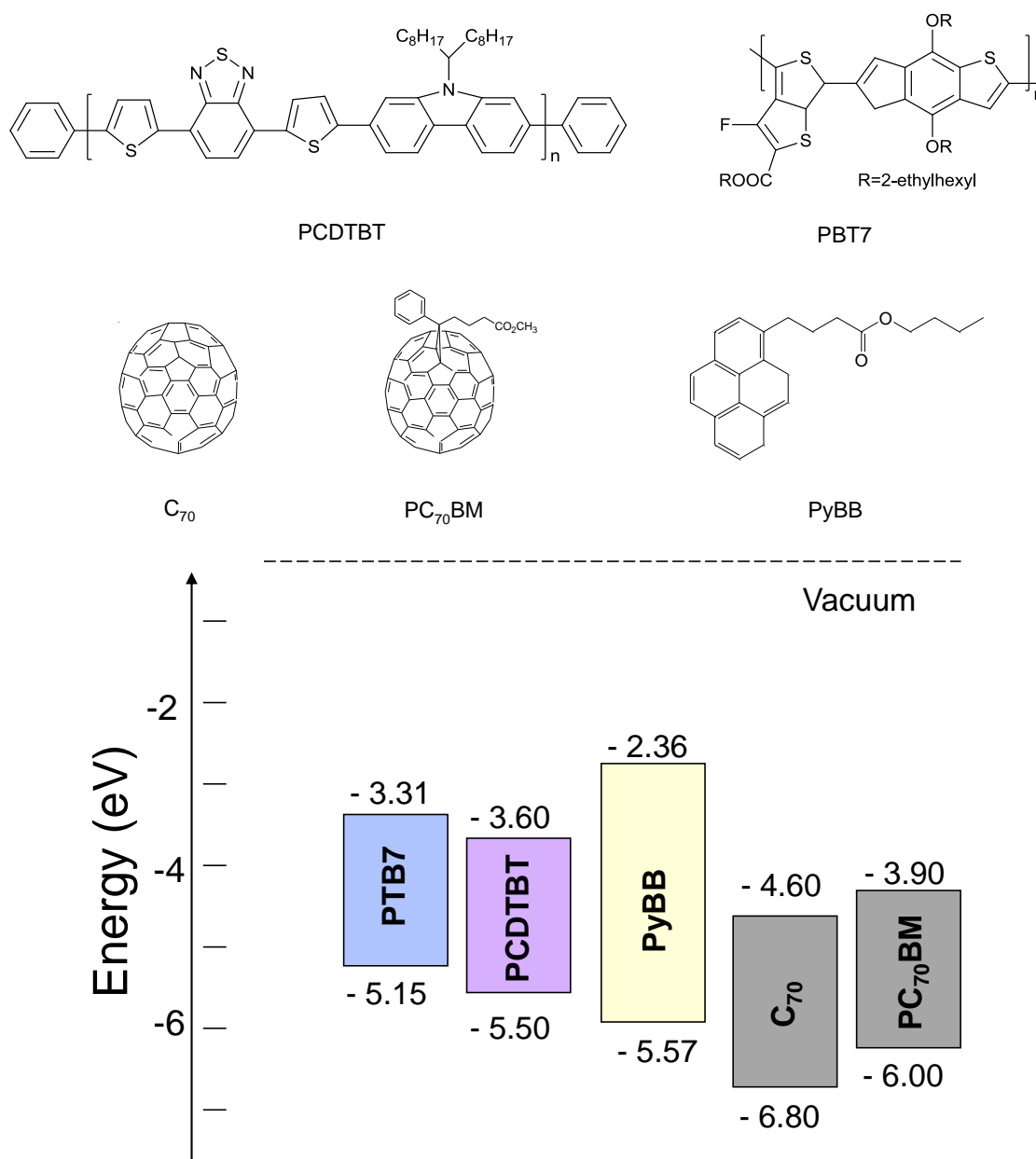


Figure 4.1 Molecular structure and energy levels of the materials used in this chapter.

4.2 Solar cells made of neat-C₇₀ as electron acceptor

Solar cells with PC₇₀BM as electron-acceptor were first prepared with both conjugated polymers, according to optimized procedures already reported in the literature for the active layer deposition and composition.^[88, 89] In particular, PTB7:PC₇₀BM solar cells were prepared in 1:1.5 weight ratio and deposited from a chlorobenzene solution (25 g L⁻¹) with 1,8-diiodooctane (3% vol) as additive, while PCDTBT:PC₇₀BM (1:4 w/w) devices were spin-coated from 1,2-dichlorobenzene (17.5 g L⁻¹). C₇₀-based solar cells were prepared in different D/A ratios from 1,2-dichlorobenzene solutions: PTB7:C₇₀ (1:2 w/w, 28 g L⁻¹) devices were deposited at 900 rpm while PCDTBT:C₇₀ (1:1 w/w, 10 g L⁻¹; 1:2 w/w, 11 g L⁻¹; 1:3 w/w, 12 g L⁻¹ and 1:4 w/w, 17.5 g L⁻¹) at 1000 rpm. For a better comparison of the cells made of the same donor, PTB7-based cells and PCDTBT-based ones, were prepared with the same thickness of the active layer, 100 nm and 70 nm respectively. Then the samples were transferred to the glove-box where the device structure was completed with the thermal evaporation of the top electrode Al (100nm).

The use of additives (1,8-diiodooctane, 1-chloronaphthalene, 1-methyl-2-pyrrolidinone) or thermal treatments were not effective in improving the performance of devices made of C₇₀.

4.2.1 Photovoltaic parameters

The *J-V* characteristics in the dark and under 100 mW cm⁻² (AM1.5G) illumination of as-cast PTB7:C₇₀ and PCDTBT:C₇₀ solar cells are shown in *Figure 4.2* and *Figure 4.3*, respectively, and compared with those obtained for the reference cells with PC₇₀BM, while the extracted photovoltaic parameters are collected in *Table 4.1*.

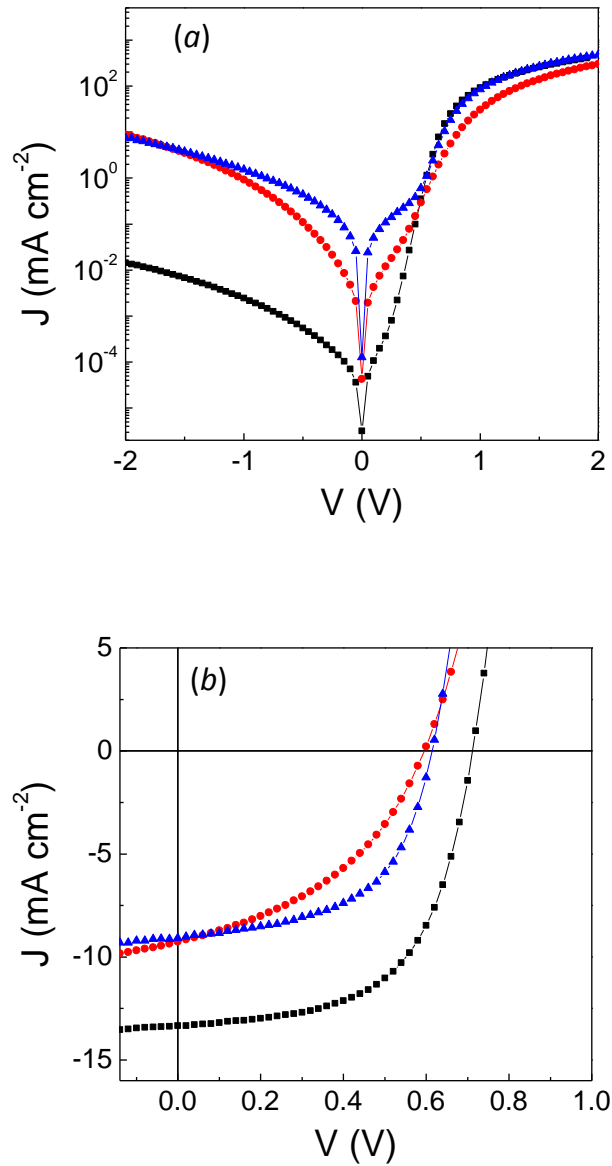


Figure 4.2 Current density – voltage characteristics in the dark (a) and under 100 mW cm⁻² illumination (b) of solar cells made of PTB7:PC₇₀BM (black squares), PTB7:C₇₀ (1:2 w/w) (red circles) and PTB7:C₇₀ (1:3 w/w) (blue triangles).

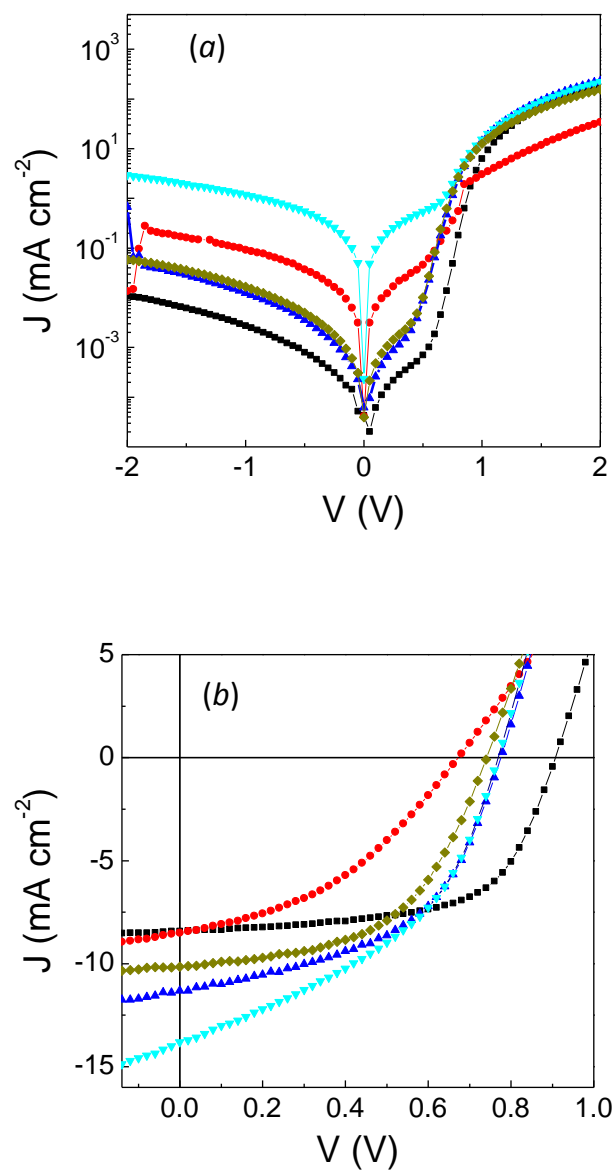


Figure 4.3 Current density – voltage characteristics in the dark (a) and under 100 mW cm^{-2} illumination (b) of solar cells made of PCDTBT:PC₇₀BM (black squares), PCDTBT:C₇₀ (1:1 w/w) (red circles), PCDTBT:C₇₀ (1:2 w/w) (blue up triangles), PTB7:C₇₀ (1:3 w/w) (cyan down triangles) and PTB7:C₇₀ (1:4 w/w) (dark yellow diamonds)

Table 4.1 Photovoltaic parameters at 100 mW cm⁻² (AM1.5G).

Active layer	D:A (w/w)	J_{sc} (mA cm ⁻²)	V_{oc} (V)	FF	η (%)
PTB7:PC ₇₀ BM	1:1.5	13.34	0.71	0.59	5.73
PTB7:C ₇₀	1:2	9.21	0.59	0.41	2.22
PTB7:C ₇₀	1:3	9.08	0.61	0.55	3.17
PCDTBT:PC ₇₀ BM	1:4	8.41	0.91	0.62	4.80
PCDTBT:C ₇₀	1:1	8.50	0.67	0.40	2.30
PCDTBT:C ₇₀	1:2	11.31	0.78	0.50	4.44
PCDTBT:C ₇₀	1:3	13.81	0.77	0.43	4.55
PCDTBT:C ₇₀	1:4	10.15	0.74	0.53	4.02

The values calculated for the power conversion efficiency of the reference cells were comparable to those reported in previous studies,^[88,89] with η of 5.73% calculated for PTB7:PC₇₀BM devices and of 4.80% for PCDTBT:PC₇₀BM cells. As shown in Table 4.1, the replacement of PC₇₀BM with C₇₀ led to the decrease of all photovoltaic parameters, with the only exception of the short-circuit current density of PCDTBT:C₇₀ solar cells. Indeed, differently from PTBT:C₇₀ devices, for which a significant reduction of J_{sc} was observed (J_{sc} of 9.08 and 9.21 mA cm⁻² for the two D/A ratios) compared to the related reference cell (13.34 mA cm⁻²), the change of the polymer donor resulted in an enhanced short-circuit current for neat-C₇₀ devices, with a J_{sc} ranging between 8.50 and 13.81 mA cm⁻², to be compared with 8.41 mA cm⁻² measured for PCDTBT:PC₇₀BM solar cells. The different behaviour of J_{sc} could be related to a different charge generation ability of the blends made of the two polymers, due to a different distribution of the D/A interface. In addition, the higher molar extinction coefficient of C₇₀, compared to PC₇₀BM, could be the origin

of the enhanced J_{sc} observed for PCDTBT:C₇₀ solar cells with respect to the PCDTBT:PC₇₀BM ones, as shown in *Figure 4.4*.

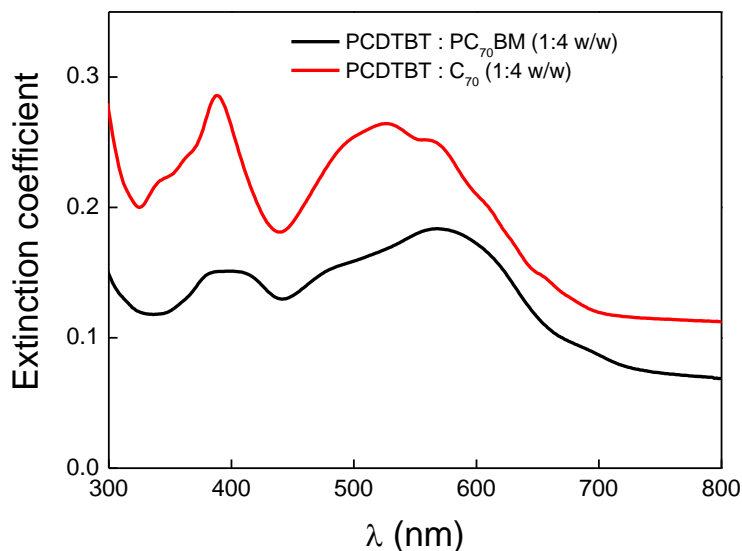


Figure 4.4 Extinction coefficients of PCDTBT:PC₇₀BM (black line) and of PCDTBT:C₇₀ (red line) blends, prepared with the same D/A weight ratio of 1:4.

The open-circuit voltage decreased from 0.71 V and 0.62 V of the reference cells made of PTB7 and PCDTBT, respectively, to values of around 0.6 V for PTB7:C₇₀ cells and ranging between 0.67 and 0.78 V in the case of PCDTBT donor. The reduction of V_{oc} upon replacing PC₇₀BM with C₇₀ could be explained by the effect of the higher leakage currents observed for cells made of neat-C₇₀ (*Figure 4.2a* and *4.3a*) as well as by the different electron affinities of the electron-acceptors.^[90] Also fill factor was found to decrease for all C₇₀-based solar cells, irrespective of the donor and of the D/A ratio, indicating higher losses for charge recombination, though FF is also affected by leakage paths. FF values in the range 0.41–0.55 were achieved for PTB7:C₇₀ solar cells and between 0.40 and 0.53 for PCDTBT:C₇₀ devices, against 0.59 and 0.62 calculated for the respective reference cells. Nevertheless, despite the loss of efficiency of solar cells made with C₇₀, good performances were obtained with PCDTBT donor at high fullerene contents. PCDTBT:C₇₀ cells prepared with 1:3 D/A ratio showed a J_{sc} of 13.81 mA cm⁻², V_{oc} = 0.77 V and FF of 43%, resulting in an efficiency of 4.55%, reduced by about 5% with respect to 4.80%

calculated for PCDTBT:PC₇₀BM reference cell. On the contrary, for the best PTBT:C₇₀ solar cells (1:3 weight ratio) a reduction of η of about 45% was observed by replacing PC₇₀BM with neat-C₇₀.

4.2.2 Analysis of photocurrents

In order to investigate the loss mechanisms in cells made of neat-C₇₀, the behaviour of photocurrents was analyzed as a function of voltage at different values of the light power intensity, and compared with that observed for the reference cells. The trend of the net photocurrent, is plotted in *Figure 4.5* and *4.6* versus the effective voltage for PTB7 and PCDTBT-based solar cells, respectively.

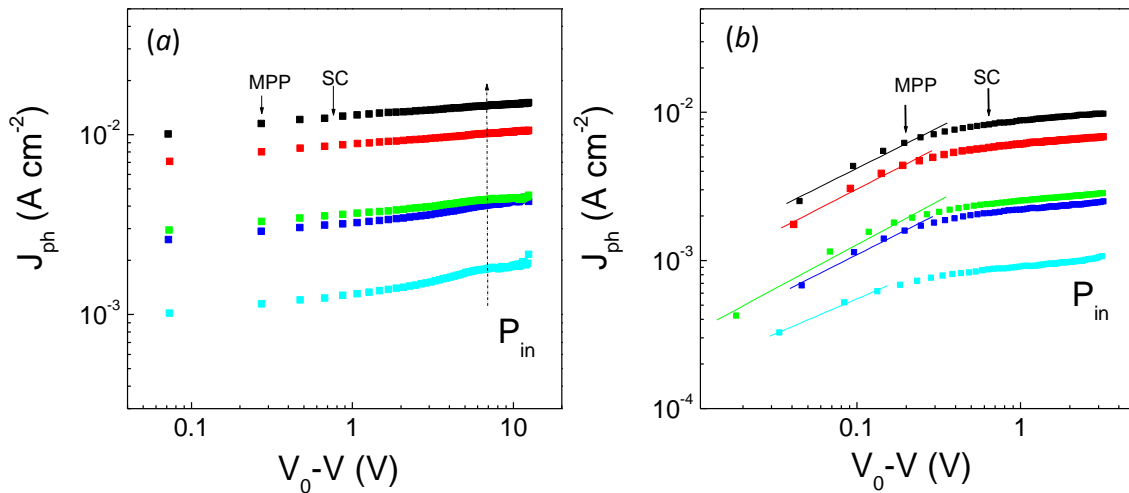


Figure 4.5 Net photocurrent as a function of the effective voltage at different light power intensities (8–100 mW cm⁻²) for PTB7:PC₇₀BM (1:1.5 w/w) (a) and PTB7:C₇₀ (1:3 w/w) (b) solar cells. Short-circuit (SC) and maximum power point (MPP) conditions are indicated by the arrows for the curves obtained at 100 mW cm⁻².

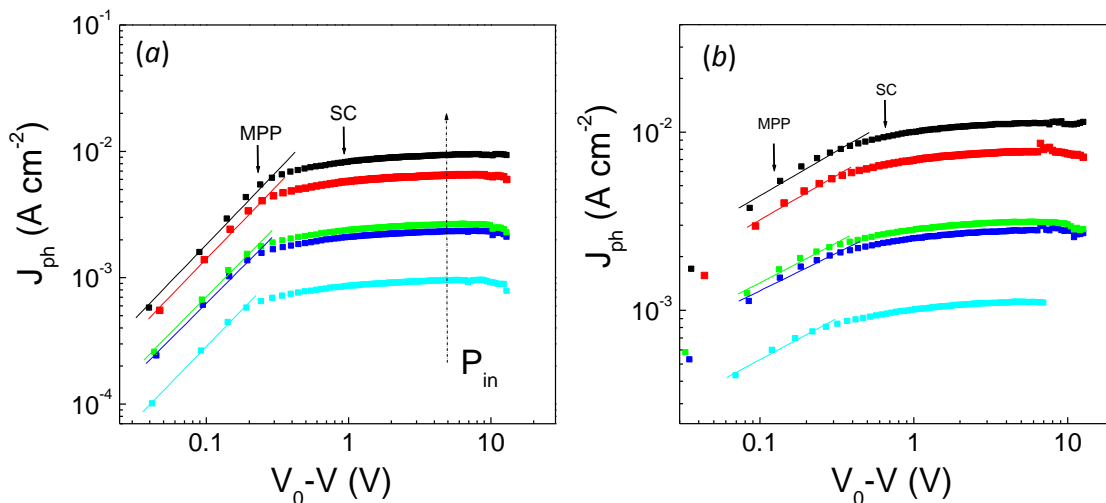


Figure 4.6 Net photocurrent as a function of the effective voltage at different light power intensities (8–100 mW cm^{-2}) for PCDTBT:PC₇₀BM (1:4 w/w) (a) and PCDTBT:C₇₀ (1:3 w/w) (b) solar cells. Short-circuit (SC) and maximum power point (MPP) conditions are indicated by the arrows for the curves obtained at 100 mW cm^{-2} .

For PTB7:PC₇₀BM solar cells, J_{ph} quickly saturates, showing a nearly constant value with the effective voltage. In these devices, charge carriers are efficiently collected at the electrodes with no recombination losses, even at low effective voltages, relevant for solar cell operation. Differently, a voltage-dependent behaviour of J_{ph} was observed for PCDCTB:PC₇₀BM solar cells (Figure 4.6a), with the saturation reached at an effective voltage of around 0.3 V independently of P_{in} and with a linear trend of J_{ph} with P_{in} at low $V_0 - V$. It is worth noting that in all cases J_{ph} is not significantly limited at short-circuit conditions, indicating that the built-in voltage is enough to sweep charge carriers out of the cells before they recombine. Differently, at lower fields, as at the maximum power point, recombination losses were observed for all cells made of neat-C₇₀ as well as for PCDTBT-based reference cells, reflecting in the lower values of FF compared to the recombination-free PTBT:PC₇₀BM devices (Table 4.1).

The different behaviour of J_{ph} in the range of low effective voltage could be attributed to different charge transport properties in the blends made of the two different donors. The mobility of charge carriers in PTBT:PC₇₀BM blend should be high enough to allow the extraction of charges before recombination even at very

low effective voltages, while a lower mobility in PCDTBT:PC₇₀BM solar cells could account for the field-dependent J_{ph} observed at low V_0-V , indicating that the drift length of charge carriers, the path they can cover before recombination, is lower than the blend thickness at those effective voltages and leading to a recombination loss.^[91] In effect, the mobility of holes in the donor phase is expected to be higher in PTB7 than in PCDTBT,^[92] though charge carrier mobility is extremely dependent on the D/A ratio and the deposition conditions of the blends.

A square-root dependence of J_{ph} with V_0-V was not observed for PCDTBT:PC₇₀BM solar cells in any range of the effective voltage, excluding for these cells space-charge effects or limitation of the photocurrent due to a low $\mu\tau$ product.^[93, 94] On the contrary, a square-root regime before saturation was observed for all cells made with neat-C₇₀, as shown in *Figure 4.5b* and *4.6b* for PTB7:C₇₀ (1:3 w/w) and PCDTBT:C₇₀ (1:3 w/w), respectively. To discern between the two possible limiting processes originating this behavior, space-charge formation or low $\mu\tau$, the trend of J_{ph} and that of the saturation voltage was analyzed with P_{in} . The results obtained for PTB7:C₇₀ (1:3 w/w) solar cells are shown in *Figure 4.7* in bilogarithmic plots. The slope of J_{ph} vs P_{in} , both at high (S_{HV}) and at low effective voltage (S_{LV}) is close to 1. 0.95 and 0.91 were calculated, respectively for S_{HV} and S_{LV} , for PTB7:C₇₀ solar cells prepared in 1:3 weight ratio. The $\frac{3}{4}$ power dependence of the photocurrent on the incident light was not observed at low P_{in} , indicating that J_{ph} is not limited by the occurrence of space-charge in these cells. The confirmation came from the behavior of V_{sat} , appearing nearly independent of P_{in} ,^[95] so showing a slope with P_{in} (S_{sat}) close to zero (a value of 0.09 was obtained for S_{sat} in PTB7:C₇₀ solar cells 1:3 w/w).

The same behaviour with light intensity was achieved for the other cells made with neat-C₇₀, as indicated by the values of S_{HV} , S_{LV} and S_{sat} collected in *Table 4.2*.

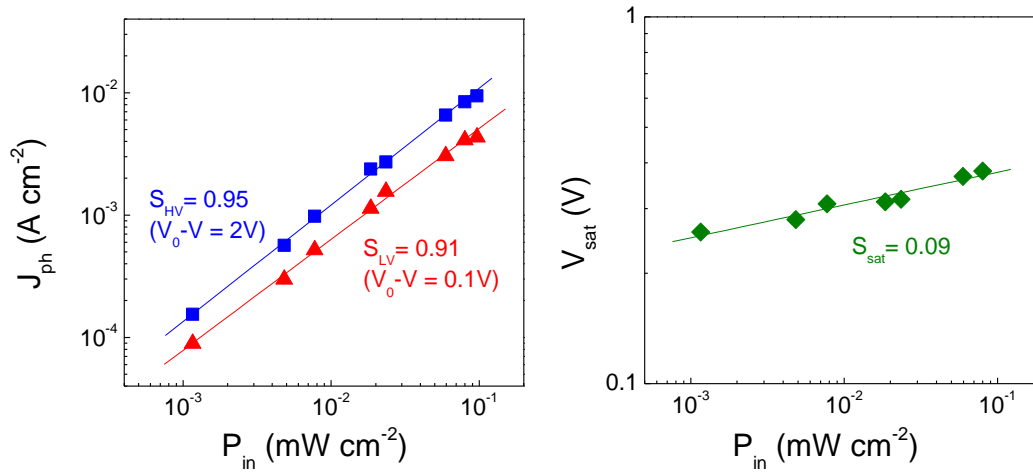


Figure 4.7 Net photocurrent at low and high effective voltage (a) and saturation voltage (b) as a function of light power for PTB7:C₇₀ (1:3 w/w) solar cells.

Table 4.2 Slopes extracted from the bilogarithmic plots of J_{ph} vs P_{in} and V_{sat} vs P_{in} .

Active layer	D:A (w/w)	S_{LV}	S_{HV}	S_{sat}
PTB7:C ₇₀	1:2	0.89	0.93	0.07
PTB7:C ₇₀	1:3	0.91	0.95	0.09
PCDTBT:C ₇₀	1:1	0.82	0.96	0.09
PCDTBT:C ₇₀	1:2	0.88	0.97	0.09
PCDTBT:C ₇₀	1:3	0.88	0.93	0.16
PCDTBT:C ₇₀	1:4	0.82	0.97	0.13

On the basis of the slopes of Table 4.2, it can be inferred that the photocurrent in C₇₀-based solar cells is limited by a low $\mu\tau$ product, rather than space-charge effects. The absence of space-charge formation can indicate that the mobility of charge carriers is not strongly unbalanced in these cells. To verify this, hole-only and electron-only devices made with the same blends used for solar cells were prepared to extract the mobility of carriers in the donor and in the acceptor phase with the space-charge limited current method, as described in the next paragraph.

4.2.3 Charge carrier mobility

As an example, the J - V curves of single-carrier devices for PTB7 and PCDTBT based solar cells are shown in *Figure 4.8* and *4.9* respectively. In most cases, a good fit of J - V characteristics (where V is given by equation 2.2) was obtained by using equation 2.1. However, the J - V curves of hole-only devices made of PTB7: C_{70} blends were consistently better described by the Mott-Gurney law with μ independent of field (equation 2.3).

In case of field-dependent mobility, the value of μ at any field E can be obtained by using the Poole-Frenkel expression in equation 1.1.

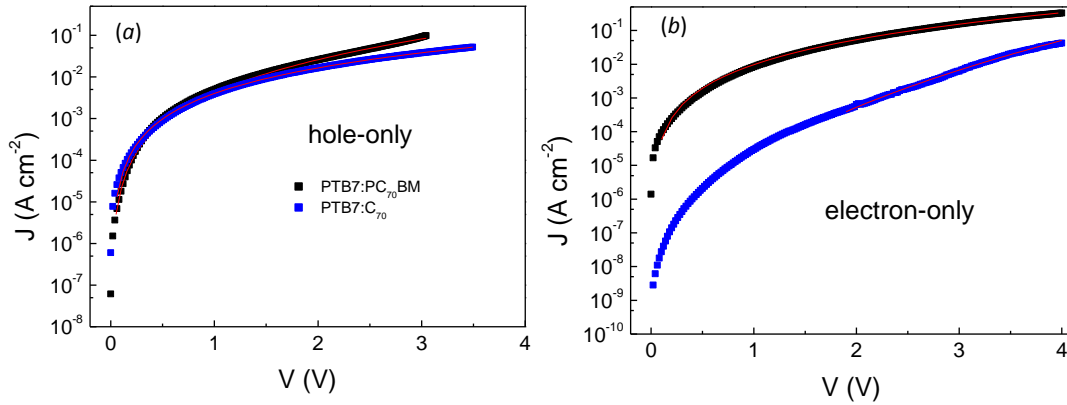


Figure 4.8 Current-density vs net voltage for hole-only (a) and electron-only (b) devices made of PTB7 as electron-donor. The red and magenta curves indicate the fit to the experimental data on the basis of equation 2.3.

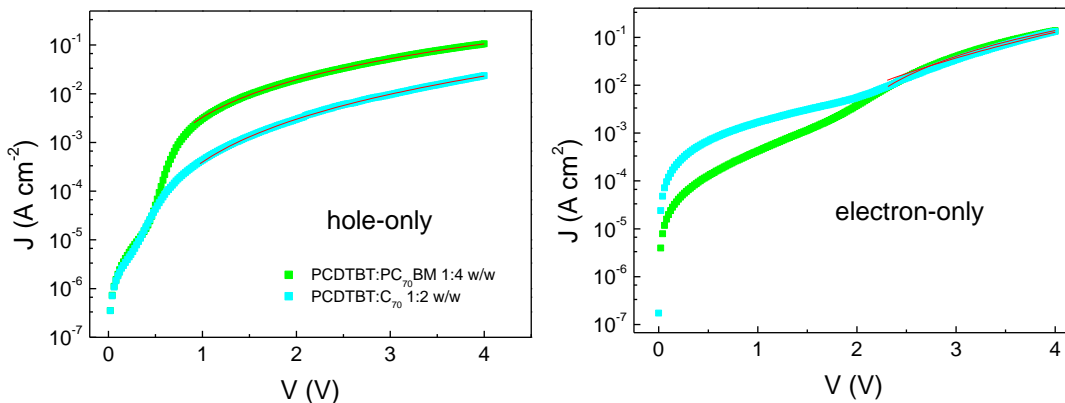


Figure 4.9 Current-density vs net voltage for hole-only (a) and electron-only (b) devices made of PCDTBT as electron-donor. The red curves indicate the fit to the experimental data on the basis of equation 2.3.

The series resistance was previously determined in devices with the same geometry and contacts of the single-carrier ones, but without the polymer/fullerene blend. The values of mobility calculated for a field of $5 \times 10^4 \text{ V cm}^{-1}$, corresponding to a potential of 0.5 V across a film 100 nm thick and close to the net potential at the maximum power point of the cells, are summarized in *Table 4.3*.

Table 4.3 Charge carrier mobility extracted from the J - V curves of single-carrier devices. The mobility values are calculated for an electric field of $5 \times 10^4 \text{ V cm}^{-1}$.

Active layer	D:A (w/w)	μ_h ($\text{cm}^2 \text{ V}^{-1} \text{ s}^{-1}$)	μ_e ($\text{cm}^2 \text{ V}^{-1} \text{ s}^{-1}$)
PTB7:PC ₇₀ BM	1:1.5	3.79×10^{-4}	4.56×10^{-4}
PTB7:C ₇₀	1:2	7.29×10^{-5}	1.97×10^{-4}
PTB7:C ₇₀	1:3	7.02×10^{-5}	4.25×10^{-4}
PCDTBT:PC ₇₀ BM	1:4	4.48×10^{-5}	3.06×10^{-5}
PCDTBT:C ₇₀	1:2	3.66×10^{-6}	1.37×10^{-5}
PCDTBT:C ₇₀	1:3	2.77×10^{-6}	1.15×10^{-5}
PCDTBT:C ₇₀	1:4	3.17×10^{-6}	3.20×10^{-5}

The mobility data of *Table 4.3* indicate a perfectly balanced charge transport for the reference solar cells, with mobilities in agreement with those already reported for the same blends prepared in similar conditions^[96] and with the expected higher values for PTB7:PC₇₀BM cells. Upon replacing PC₇₀BM with C₇₀, significant variations of the mobility of negative carriers were not observed, whereas a systematic decrease of the mobility of holes was obtained for both donors. The mobility of positive carriers was reduced by about 5 folds in PTB7:C₇₀ blends and by roughly one order of magnitude in PCDTBT:C₇₀ ones, resulting in charge carrier mobilities not strongly unbalanced, consistent with the absence of space-charge formation in the C₇₀-based solar cells.

The reduction of mobility in blends made of neat C₇₀, compared to the reference ones prepared with PC₇₀BM as acceptor, could explain the photocurrents limited by a low $\mu\tau$ product.

4.2.4 Impedance spectra

Impedance spectroscopy measurements were performed in order to get further information, in particular to extract the effective lifetime of charge carriers in the investigated solar cells. Impedance spectra were taken under illumination and superimposing a dc bias equivalent to the open-circuit voltage of the device on the harmonic voltage modulation. Under this condition, the photocurrent is cancelled by the recombination flux.

Typical impedance spectra obtained for the investigated cells are displayed in *Figure 4.10* in the Nyquist representation, with frequency as an implicit variable.

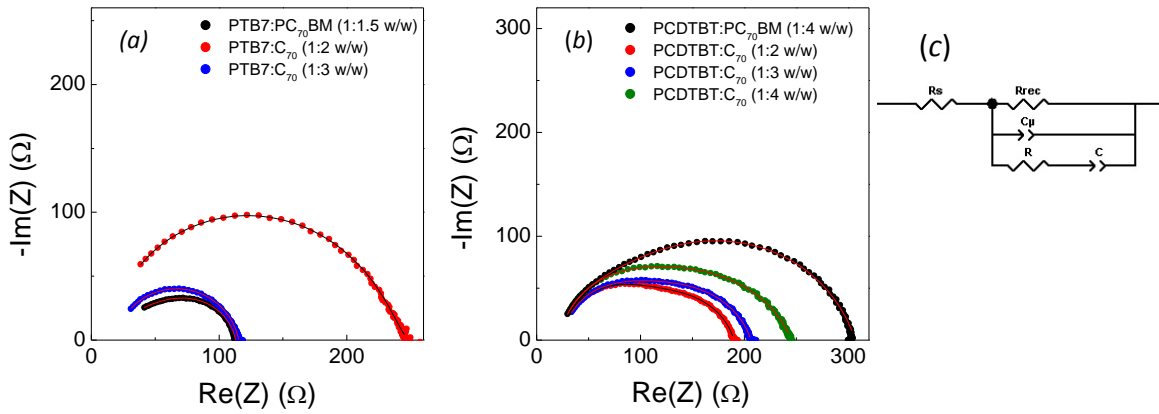


Figure 4.10 Nyquist plots for solar cells made of PTB7 (a) and PCDTBT (b) polymers under 1 sun irradiation conditions. Lines indicate the fit to the experimental data modelled by the circuit (c).

The Nyquist plots of PTB7-based devices exhibited a major arc in the investigated frequency range while the impedance spectra of PCDTBT-based cells showed additional features toward higher frequencies (*Figure 4.10b*). In both cases, a high quality fit of the experimental data was provided by the equivalent circuit depicted in *Figure 4.10b*, as demonstrated by the solid lines through the data points. The device series resistance is accounted by the resistor R_s in the model circuit of *Figure 4.10a*, while R_{rec} represents the recombination resistance, related to the recombination current, and C_μ is the chemical capacitance,^[55] due to the accumulation of photogenerated charge carriers and represented in the equivalent circuit by a constant phase element^[48] for better fittings. The additional series

combination of the resistor R and the constant phase element C , could account for charge trapping phenomena.^[56, 97, 98] The effective lifetime of charge carriers obtained from R_{rec} and C_{μ} ($\tau = R_{rec}C_{\mu}$) was compared with the extraction time (t_{ex}) of slowest charge carriers, holes for solar cells here investigated. The extraction time was estimated considering an average path of $L/2$ for carriers to be extracted and by using the relationship

$$t_{ex} = \frac{L/2}{\mu E} \quad (4.1)$$

The values of t_{ex} , obtained from the hole mobilities reported in *Table 4.3* and for $E = 5 \times 10^4 \text{ V cm}^{-1}$, are compared in *Figure 4.11* with the effective lifetimes of charge carriers. For both reference cells τ is longer than t_{ex} , assuring that charge carriers can be efficiently collected at the electrodes before recombination. The situation is reversed when PC₇₀BM is replaced by C₇₀, with t_{ex} much increased due to the lower mobility of charge carriers.

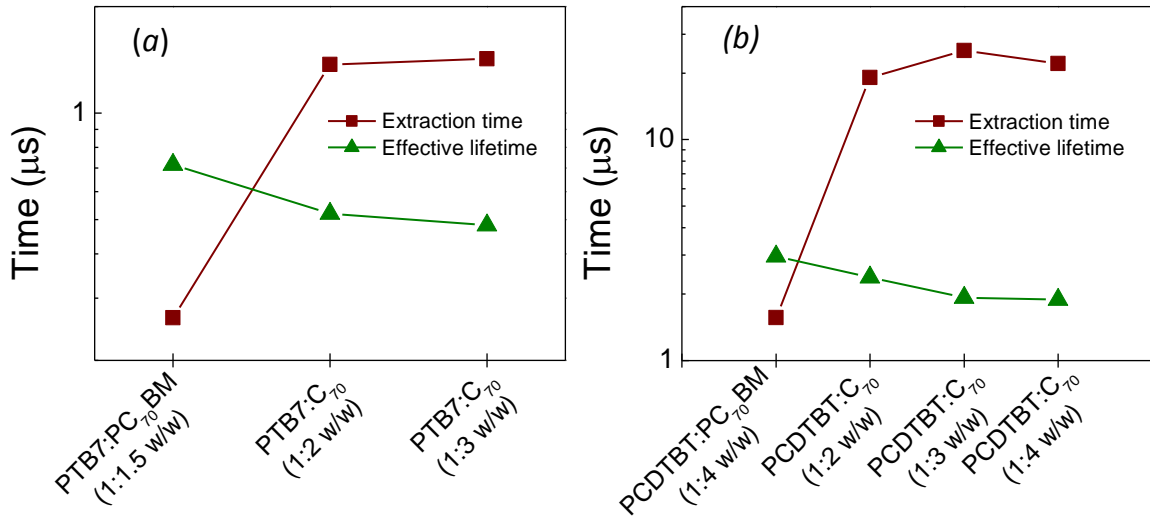


Figure 4.11. Extraction time and effective lifetime of charge carriers in PTBT-based cells (a) and PCDTBT-based cells (b).

As shown in *Figure 4.11*, τ did not drastically change by changing the acceptor, however the product $\mu\tau$ (with μ representing the mobility of positive carriers) is significantly reduced in neat-C₇₀-based cells as displayed in *Figure 4.12*. $\mu\tau$ of the

order of $10^{-10} \text{ cm}^2 \text{ V}^{-1}$ in the reference cells decreased by one order of magnitude, justifying the square-root dependence of the photocurrent on the effective voltage observed for C_{70} -based cells.

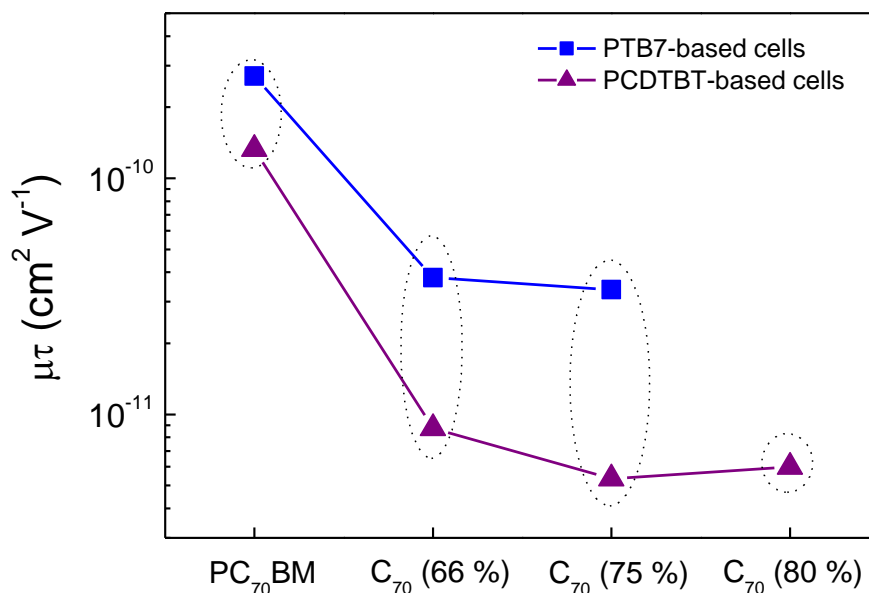


Figure 4.12. Mobility–lifetime product for PTB7-based cells (blue squares) and PCDTBT-based cells (purple triangles).

4.2.5 Blend morphology

Charge transport in the bicontinuous D/A network of organic solar cells is strictly related to the blend morphology, so the surface morphology of the investigated blends, deposited in the same conditions used for the preparation of solar cells, was characterized by AFM in tapping mode. The AFM images of PTB7: C_{70} solar cells (Figure 4.13) revealed an expected highly segregated morphology, reasonably due to the self-aggregation of C_{70} because of its poor solubility. On the contrary, the PTB7:PC₇₀BM reference blend showed the formation of a relatively well-organized phase percolation.

The formation of large domains with a size of hundreds of nm in PTB7: C_{70} blends could prevent the formation of the continuous interpenetrated D/A network required for the effective transport of charge carriers, reflecting in the worsening of charge carrier mobility. The large-domain morphology of PTB7: C_{70} films was also

accomplished by a higher root-mean-square roughness, compared to the reference blend with PC₇₀BM. The values of R_q , evaluated on a scan area of 2 $\mu\text{m} \times 1 \mu\text{m}$, were 3.10, 5.31 and 7.39 nm for PTB7:PC₇₀BM, PTB7:C₇₀ (1:2 w/w) and PTB7:C₇₀ (1:3 w/w), respectively.

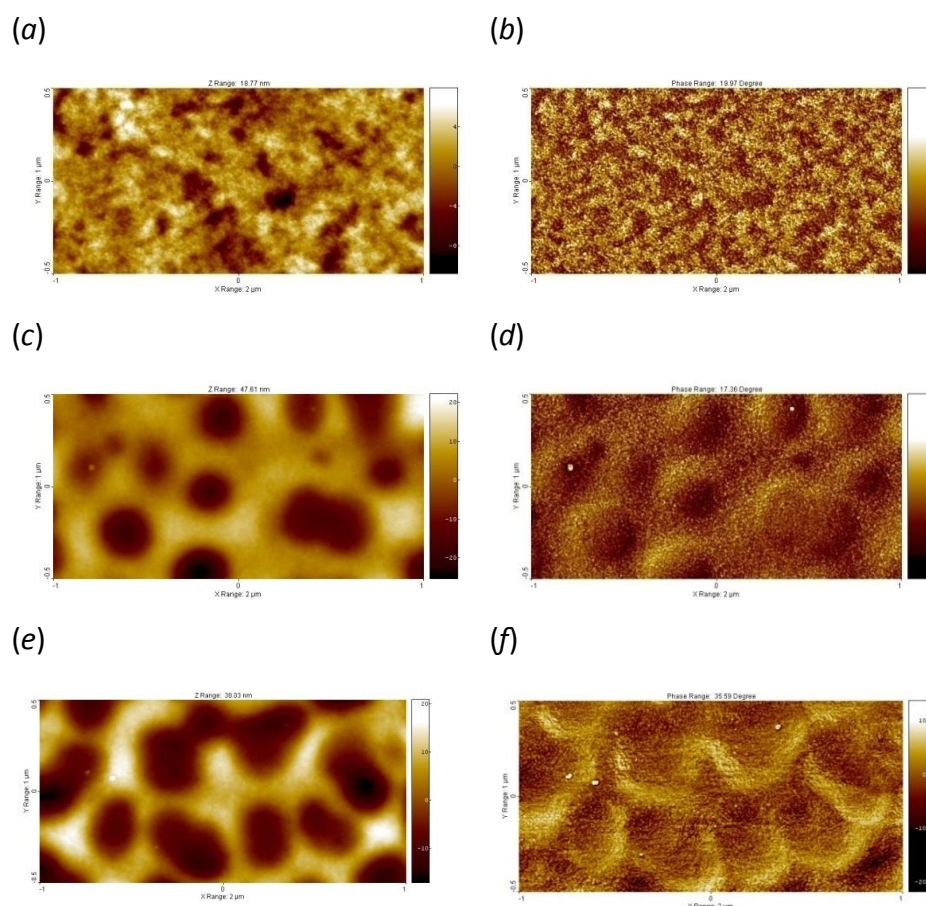


Figure 4.13. AFM images (2 $\mu\text{m} \times 1 \mu\text{m}$) of PTB7-based blends: PTB7:PC₇₀BM (1:1.5 w/w) (a) and (b); PTB7:C₇₀ (1:2 w/w) (c) and (d); PTB7:C₇₀ (1:3 w/w) (e) and (f). (a), (c) and (e): height; (b), (d) and (f): phase.

Surprisingly, by changing the polymer electron donor, the surface morphology observed for the neat-C₇₀ blends was very different, as shown in Figure 4.14, in which the AFM images of PCDTBT-based blends are compared. Significant differences between PCDTBT:PC₇₀BM and PCDTBT:C₇₀ were not revealed, as clearly demonstrated by Figure 4.14. For all PCDTBT-based blends, irrespective of the fullerene acceptor, a fine mixing of the two components was achieved. Accordingly, very low and similar R_q values were obtained, ranging between 0.61 nm and 0.87

nm. The images of *Figure 4.14* indicate that, differently from PTB7, PCDTBT acts as an excellent dispersing medium for C₇₀ molecules, enabling low-cost and efficient neat-C₇₀ solar cells.

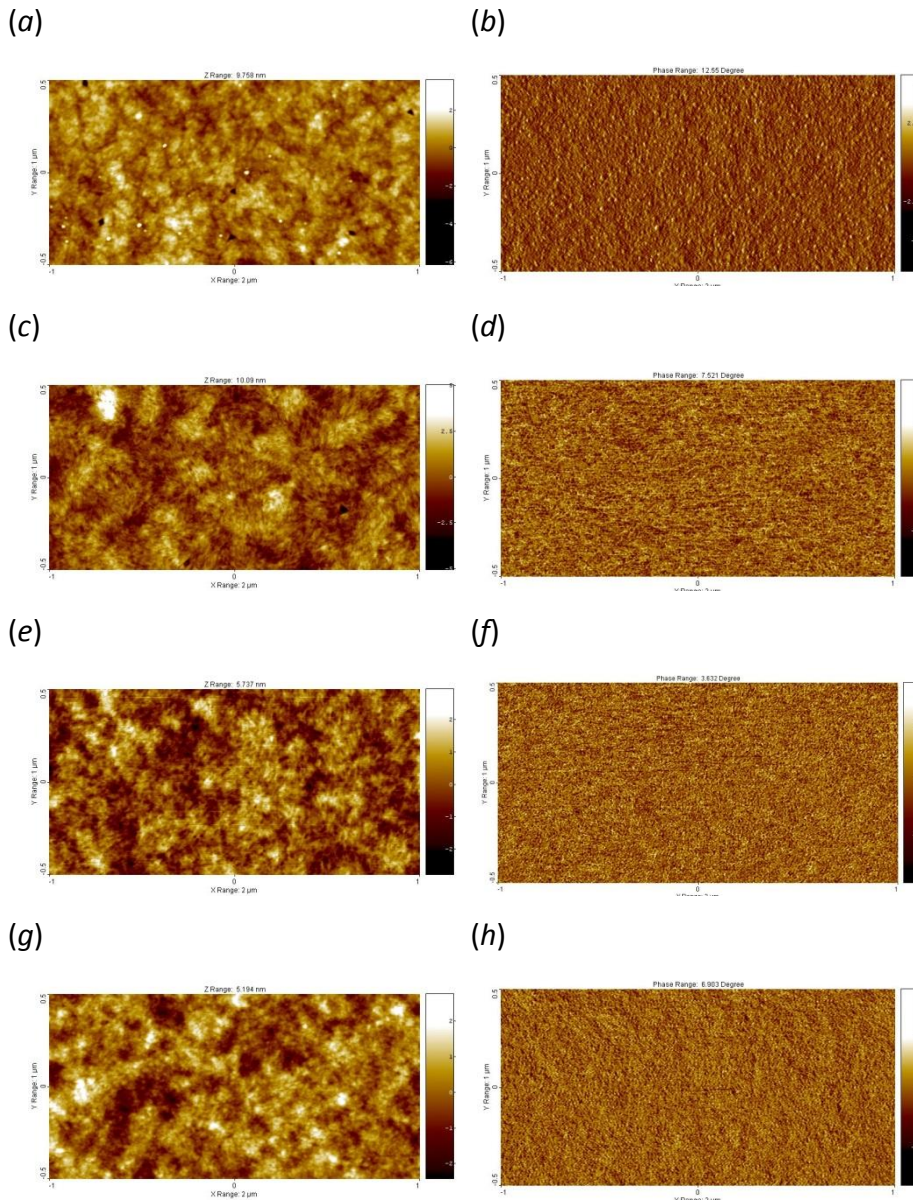


Figure 4.14. AFM images ($2\ \mu\text{m} \times 1\ \mu\text{m}$) of PCDTBT-based blends: PCDTBT:PC₇₀BM (1:4 w/w) (a) and (b); PCDTBT:C₇₀ (1:1 w/w) (c) and (d); PCDTBT:C₇₀ (1:2 w/w) (e) and (f); PCDTBT:C₇₀ (1:4 w/w)(g) and (h). (a), (c), (e) and (g): height; (b), (d), (f) and (h): phase.

The morphology of the blends is in agreement with the values of the short-circuit current reported in *Table 4.1*. Indeed, the reduction of J_{sc} in PTB7-based solar cells by replacing PC₇₀BM with C₇₀ can be clearly attributed to the

drastic reduction of the extension of the D/A interface, because of the high phase segregation. Differently, the surface morphology of all PCDTBT-based blends is similar, confirming that the enhanced light absorption is the main reason for the higher J_{sc} observed for PCDTBT:C₇₀ solar cells, compared to the reference PCDTBT:PC₇₀BM. However, the lower mobility values in the donor phase of PCDTBT:C₇₀ blends (Table 4.3) indicate that the polymer network is not as effective as in the reference PCDTBT:PC₇₀BM mixture in providing adequate pathways for the transport of positive charge carriers. The origin of the inspected excellent miscibility of PCDTBT:C₇₀ blends is still under investigation.

4.3 The use of pyrene as dispersant

In the previous *paragraph* it was found that, differently from PCDTBT:C₇₀ blends, PTB7 polymer showed poor miscibility with C₇₀, leading to a highly segregated morphology for PTB7:C₇₀ blends, with the formation of agglomerates on the micrometer scale. This is commonly found with neat-fullerenes, responsible for the drastic loss of efficiency usually observed in this kind of solar cells. To overcome this problem, a third component was introduced in the blend, to promote the dispersion of C₇₀ in the polymer matrix. To this purpose, PyBB was used, due to the faculty of pyrene to form strong π - π interactions with carbon nanotubes, as reported in the literature.^[99, 100] The results available in the literature, led to the hypothesis that the same interactions could establish with C₇₀ molecule, originating a C₇₀-PyBB adduct (Figure 4.15) with a good solubility in chlorinated solvents.

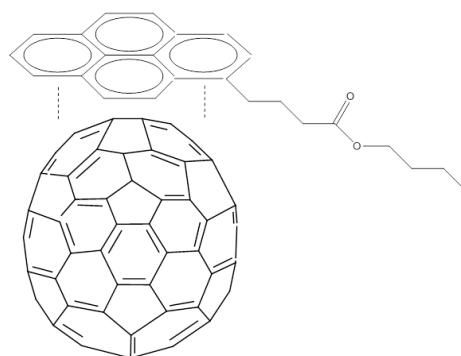


Figure 4.15 C₇₀-PyBB adduct with π - π interactions.

All solar cells with PyBB as dispersant were prepared in 1,2-dichlorobenzene with a C₇₀:PyBB molar ratio of 1:1 and deposited at 1000 rpm. PTB7:C₇₀:PyBB blends were prepared in different D/A ratios (1:1, 1:2 and 1:3 w/w, 34 g L⁻¹). The thickness of solar cells was about of 100 nm. An Al cathode (100 nm) was used.

4.3.1 Blend morphology

Figure 4.16 shows the morphology observed for some PTB7:C₇₀:PyBB blends, in comparison with that of a blend without pyrene (PTB7:C₇₀, D/A 1:2 w/w). The AFM images clearly show the effectiveness of PyBB in promoting the dispersion of C₇₀ in the polymer matrix. Moreover, the micrometric agglomerates of the PTB7:C₇₀ blend disappeared with the addition of pyrene. This had relevant effects also on the roughness of the films, which shifted from 5.31 nm in the absence of pyrene to values between 0.63 and 2.66 nm for PTB7:C₇₀:PyBB blends. The maximum dispersion of C₇₀ was observed for the mixture PTB7:C₇₀:PyBB 1:2 w/w, which showed the minimum roughness of 0.63 nm. In the overall, the look of the micrometer scale of the blends with pyrene is not very different from that of the high efficiency PTB7:PC₇₀BM active layer (Figure 4.13).

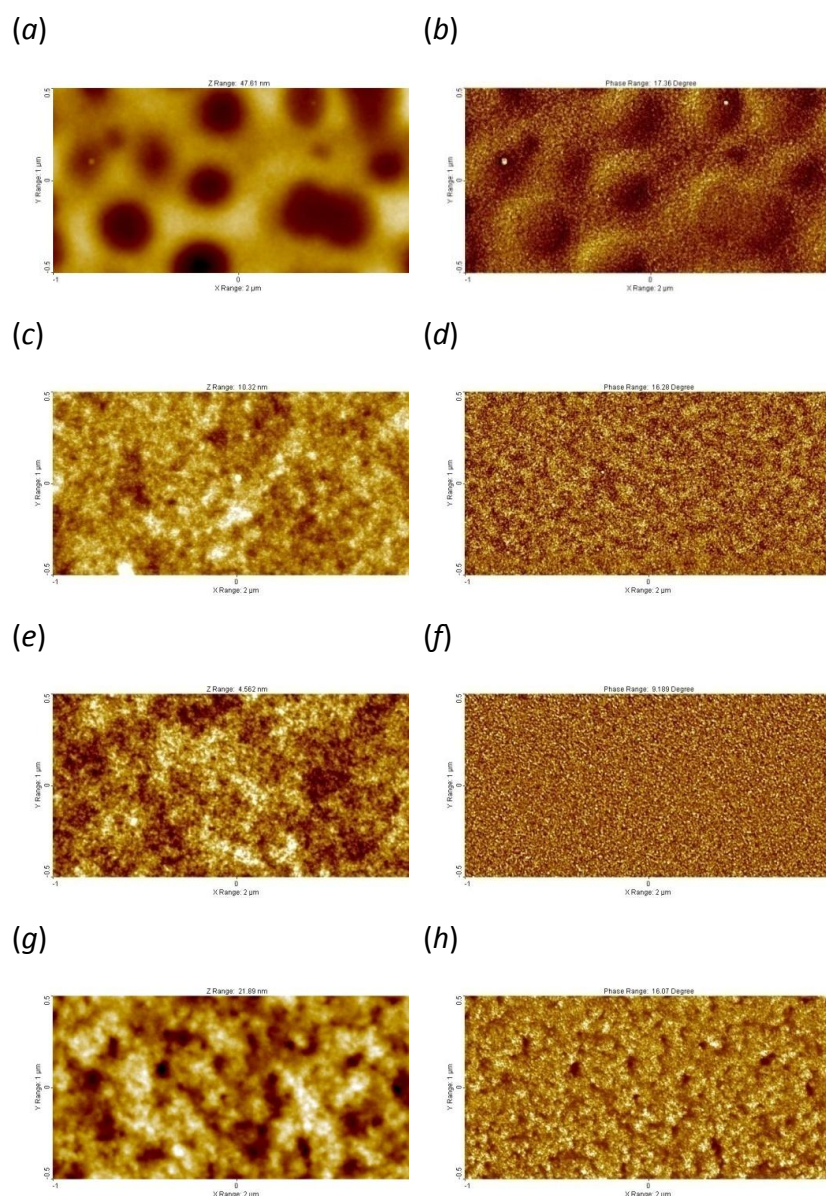


Figure 4.16. AFM images ($2 \mu\text{m} \times 1 \mu\text{m}$) of PTB7-based blends: PTB7:C₇₀ 1:2 w/w (a, b); PTB7:C₇₀:PyBB 1:1 w/w (c, d); PTB7:C₇₀:PyBB 1:2 w/w (e, f) and PTB7:C₇₀:PyBB 1:3 w/w (g, h). (a), (c), (e) and (g): height; (b), (d), (f) and (h): phase.

4.3.2 Photovoltaic parameters

The J - V characteristics in the dark and under 100 mW cm^{-2} illumination of PTB7:C₇₀:PyBB solar cells are shown in Figure 4.17, while the extracted photovoltaic parameters are collected in Table 4.4. Differently from PTB7:C₇₀ solar cells, a good rectification behaviour of the J - V characteristics was obtained, due to the much better film-forming properties of blends containing PyBB. The typical rectification

ratio at ± 2 V was of the order of 10^3 , which positively affected the V_{oc} of the related solar cells, as shown in *Table 4.4*.

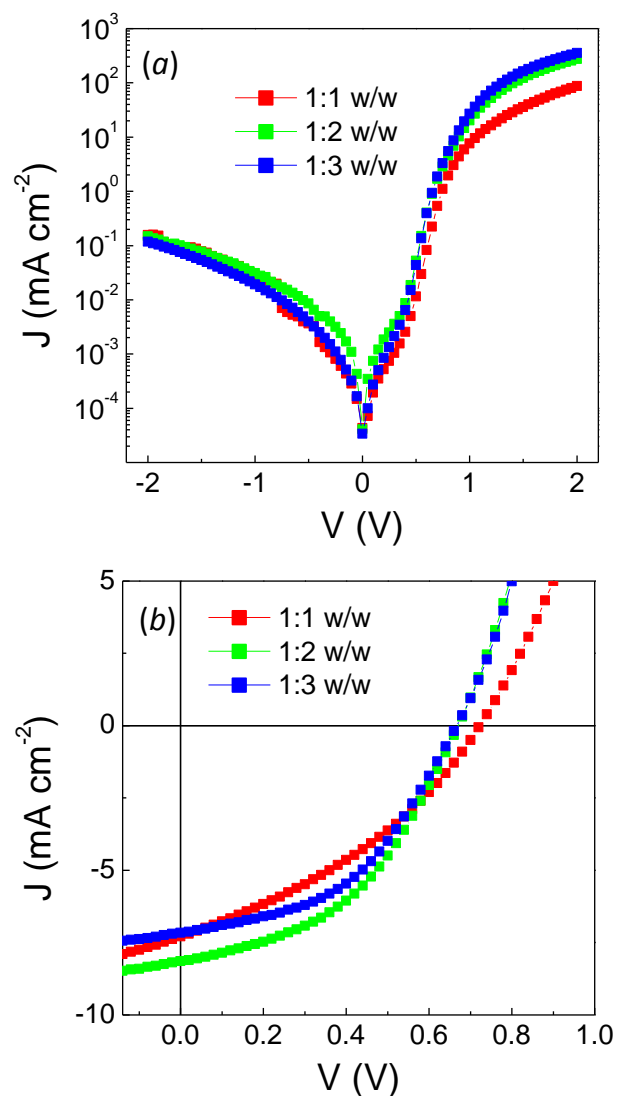


Figure 4.17 J - V characteristics in the dark (a) and under 100 mW cm^{-2} AM1.5G irradiation (b) for PTB7:C₇₀:PyBB solar cells, prepared with different PTB7:C₇₀ weight ratios (shown in the figure).

Table 4.4 Photovoltaic parameters at 100 mW cm⁻² (AM1.5G).

Active layer	D:A (w/w)	J_{sc} (mA cm ⁻²)	V_{oc} (V)	FF	η (%)
PTB7:C ₇₀ :PyBB	1:1	7.12	0.72	0.36	1.83
PTB7:C ₇₀ :PyBB	1:2	8.14	0.67	0.45	2.43
PTB7:C ₇₀ :PyBB	1:3	7.16	0.67	0.46	2.19

The data of Table 4.4 indicate that, despite the excellent dispersion of C₇₀ promoted by PyBB, the performance of PTB7:C₇₀:PyBB solar cells are not better than those made with neat-C₇₀. By changing the D/A weight ratio, a moderate variation of the photovoltaic parameters was observed, with the short-circuit current between 7.12 and 8.14 mA cm⁻², the open-circuit voltage between 0.67 and 0.72 V, the fill factor between 0.36 and 0.46, resulting in a power conversion efficiency ranging between 1.83 and 2.43%. Compared to PTB7:C₇₀ solar cells (Table 4.1), lower values for J_{sc} , FF and η were achieved. Indeed, PTB7:C₇₀ devices prepared with a D/A weight ratio of 1:3 exhibited a fill factor of 0.55, a J_{sc} of 9.08 mA cm⁻² (increasing to 9.21 mA cm⁻² for 1:2 D/A weight ratio) and a η of 3.17%. The reduced J_{sc} of PyBB-based solar cells can be explained by the reduced mass of the light-absorbing materials in these three-component blends, the thickness being the same of PTB7:C₇₀ solar cells, though the better intermixed morphology of PTB7:C₇₀:PyBB active layers should be more advantageous for the generation of free charge carriers. The photovoltaic parameter showing an enhanced value, compared to PTB7:C₇₀ solar cells, was V_{oc} , ranging between 0.67 and 0.72 V, not reduced by the high leakage currents observed for devices made without PyBB (Figure 4.2).

The light-intensity dependence of J_{sc} (Figure 4.18) indicated that, also for cells made with pyrene, bimolecular recombination is not a relevant channel loss at short-circuit conditions, given the nearly linear trend of J_{sc} with P_{in} . Indeed, the

values of α (ranging between 0.94 and 0.96) were found to be similar to those calculated for solar cells without PyBB.

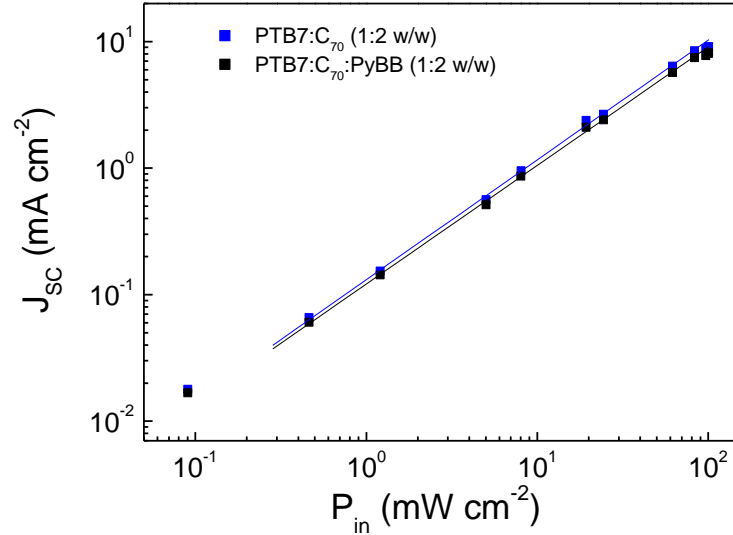


Figure 4.18. Dependence of J_{sc} on P_{in} for solar cells made with and without pyrene. Lines indicate the linear fit to the experimental data.

4.3.3 Analysis of photocurrents

Figure 4.19 shows, as an example, the trend of the net photocurrent, plotted versus the effective voltage and for different P_{in} , calculated for PTB7:C₇₀:PyBB solar cells in 1:2 D/A ratio. The saturation was reached at high effective voltages, indicating that, at high electric fields, nearly all the excitons dissociated at the donor/acceptor interface lead to the generation of pairs of free charge carriers, effectively collected at the electrodes without recombination. Differently, a voltage-dependent behavior of J_{ph} was observed at low V_0-V , with a square-root regime before saturation for all P_{in} . The same behaviour of J_{ph} with the effective voltage and P_{in} was observed also for PTB7:C₇₀:PyBB solar cells prepared with the other D/A weight ratios, with the exception of PTB7:C₇₀:PyBB blend prepared with a D:A ratio of 1:3 w/w, for which the saturation was not reached in the investigated voltage range.

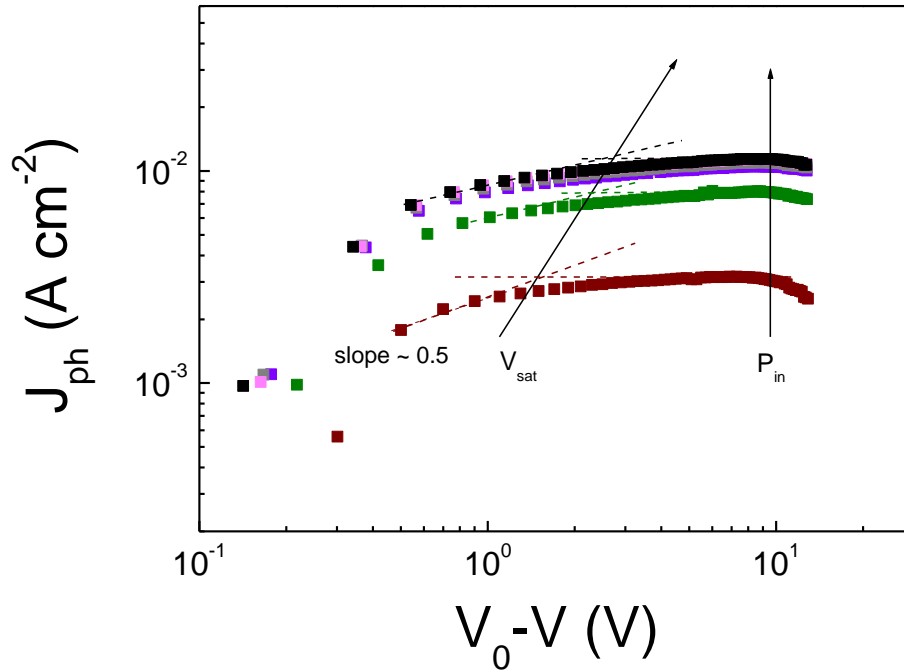


Figure 4.19 Light–intensity dependence of the net photocurrent versus the effective voltage for a PTBT7:C₇₀:PyBB solar cell (D/A 1:2 w/w). The intensity was varied from 24.3 mW cm⁻² to 100 mW cm⁻².

To discriminate between the two possible limiting processes originating the square–root regime of the photocurrent, space–charge formation or low $\mu\tau$ product, the trend of J_{ph} and that of the saturation voltage was analyzed with P_{in} . The slope of J_{ph} vs P_{in} at high effective voltage was found to be 1.00 for the cells prepared with 1:2 D/A weight ratio (Figure 4.20a), while that at low effective voltage was 0.79. The roughly $\frac{3}{4}$ power dependence of the photocurrent at low P_{in} might suggest a limitation of J_{ph} by the occurrence of space–charge in these cells, confirmed by the square–root trend of the saturation voltage with the light intensity^[101], as shown in Figure 4.20b, in which S_{sat} (0.42) indicates the slope of the double–logarithmic plot V_{sat} vs P_{in} . The same behavior was observed for the cells prepared with the other weight ratios, as demonstrated by the slopes collected in Table 4.6.

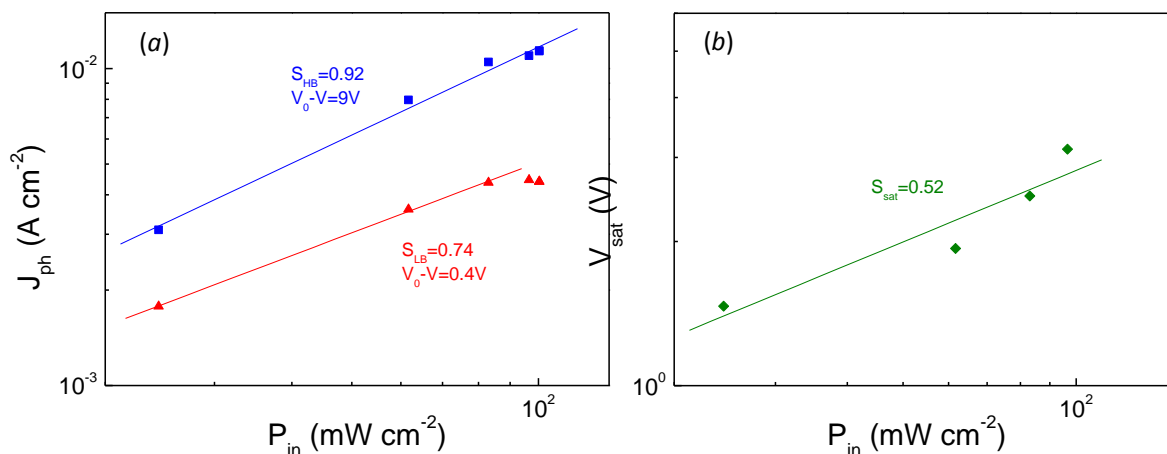


Figure 4.20 Light–intensity dependence of the photocurrent (a) and the saturation voltage (b) for a PTB7:C₇₀:PyBB device (D/A 1:2 w/w). Lines indicate the linear fit to the experimental data. The values of the slopes are also reported.

Table 4.6 Slopes of the double–logarithm plots J_{ph} vs. P_{in} and V_{sat} vs. P_{in}

Active layer	D:A (w/w)	S_{LB}	S_{HB}	S_{sat}
PTB7:C ₇₀ :PyBB	1:1	0.77	0.94	0.46
PTB7:C ₇₀ :PyBB	1:2	0.74	0.92	0.52
PTB7:C ₇₀ :PyBB	1.3	0.74	0.88	--

The values of the slopes of Table 4.6, clearly prove that J_{ph} is limited by the build–up of space charge in all solar cells prepared with pyrene. This result suggests that charge carrier mobility in this devices could be strongly unbalanced.

4.3.4 Charge carrier mobility

In order to prove our hypothesis about the strongly unbalanced mobility in solar cells with pyrene, hole–only and electron–only PTB7:C₇₀:PyBB devices were prepared as described in paragraph 2.1.1, to measure the charge carrier mobility with the SCLC technique. The best fit of the experimental data was obtained by using the Mott–Gurney law modified for μ dependent on field (equation 2.3). The parameters extracted from the fit of the J – V curves are collected in Table 4.7.

Table 4.7 Hole and electron mobility (calculated for an electric field of 10^5 V cm^{-1}) and γ parameter for PTB7:C₇₀:PyBB blends.

Active layer	D:A (w/w)	μ_h ($\text{cm}^2 \text{ V}^{-1} \text{ s}^{-1}$)	μ_e ($\text{cm}^2 \text{ V}^{-1} \text{ s}^{-1}$)	γ_h ($\text{cm}^{1/2} \text{ V}^{-1/2}$)	γ_e ($\text{cm}^{1/2} \text{ V}^{-1/2}$)
PTB7:C ₇₀ :PyBB	1:1	5.49×10^{-5}	5.21×10^{-7}	2.90×10^{-4}	1.30×10^{-2}
PTB7:C ₇₀ :PyBB	1:2	4.28×10^{-5}	4.57×10^{-7}	--	1.20×10^{-2}
PTB7:C ₇₀ :PyBB	1:3	2.72×10^{-5}	5.67×10^{-7}	4.00×10^{-4}	1.40×10^{-2}

Despite the clear morphological variation, the mobility of holes does not undergo significant variations in the devices with pyrene, compared with solar cells prepared without PyBB (Table 4.3). The hole mobility was between 2.72×10^{-5} and $5.49 \times 10^{-5} \text{ cm}^2 \text{ V}^{-1} \text{ s}^{-1}$ by changing the D/A ratio of PTB7:C₇₀:PyBB blends. Differently, the mobility of negative carriers was found to be drastically reduced, in comparison with that of PTB7:C₇₀ cells. Mobility values between 4.57×10^{-7} and $5.67 \times 10^{-7} \text{ cm}^2 \text{ V}^{-1} \text{ s}^{-1}$ were obtained for electrons, that is, roughly two orders of magnitude lower than in solar cells without PyBB. In addition, a strong dependence of the electron mobility on the electric field was also observed, as demonstrated by the high values of γ_e .

In spite of the presence of pyrene, solar cells with PyBB showed strongly unbalanced hole and electron mobility. This condition results favourable for the formation of space charge, as confirmed by the behaviour observed for the photocurrent. For these cells, negative charge carriers are much slower than positive ones and tend to be accumulated in the device. The accumulation of charge favours the bimolecular recombination processes, with consequent loss of the device performance.

4.3.5 Impedance spectra

The impedance spectra obtained under 100 mW cm^{-2} illumination for PTB7:C₇₀:PyBB devices are displayed in Figure 4.21 and compared with that of a cell without pyrene. The Nyquist plots of PTB7:C₇₀:PyBB cells exhibited a major arc in the low frequency range and a smaller one toward high frequency. For comparison, the

spectrum taken in the same conditions for a PTB7:C₇₀ (1:2 D/A) cell is also reported in the figure. The impedance spectra of PTB7:C₇₀:PyBB cells show higher resistance and capacitance (Figure 4.22), compared to devices made without PyBB. The increased capacitance, for cells made with the same area and thickness, can indicate charge trapping phenomena in solar cells prepared with PyBB^[102].

The experimental data were fitted with the same equivalent circuit used for the solar cells described in paragraph 4.2.4. The data extracted from the fitting are collected in Table 4.8. Also the increased charge carrier lifetime in PTB7:C₇₀:PyBB cells, compared to cells without pyrene, is a further indication of charge trapping effects^[56].

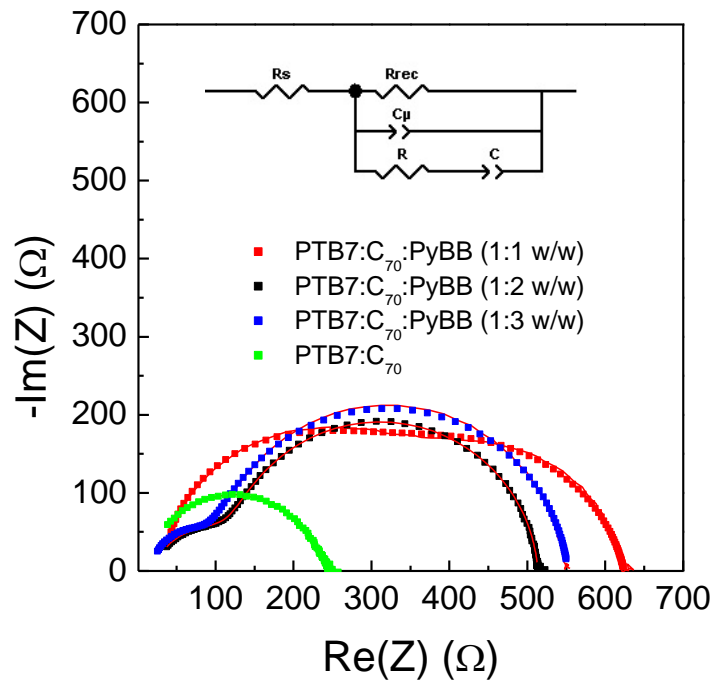


Figure 4.21 Cole–Cole plots of PTB7:C₇₀:PyBB and PTB7:C₇₀ (D/A 1:2 w/w) solar cells. Lines indicate the fit to the experimental data modeled by the circuit shown in inset.

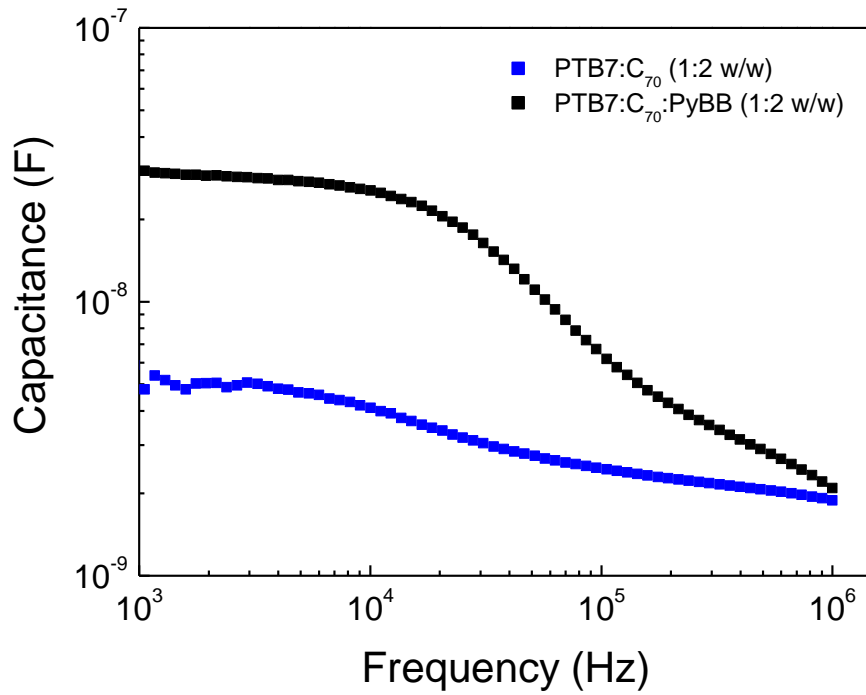


Figure 4.22 Capacitance as a function of the frequency in PTB7-based solar cells. The D/A weight ratio is indicated in parenthesis.

Table 4.9 Parameters extracted from the fit of Cole-Cole plots at 1 sun.

Active layer	D:A (w/w)	R_{rec} (Ω)	C_{μ} (nF)	τ (μ s)
PTB7:C ₇₀	1:2	231.5	7.2	1.7
PTB7:C ₇₀ :PyBB	1:1	590.3	9.9	5.9
PTB7:C ₇₀ :PyBB	1:2	495.4	56.6	28.0
PTB7:C ₇₀ :PyBB	1:3	535.4	46.8	25.1

The impedance measurements were performed at different levels of the light power intensity, in order to get indication on the order of charge recombination processes in the investigated cells. It has been shown that R_{rec} is related to V_{oc} , dependent on P_{in} , through the following expression:

$$R_{rec} \propto \exp\left(-\frac{q\beta}{2kT}V_{oc}\right) \quad (4.2)$$

where the parameter β represents the recombination order^[56]. From the slopes of the semilogarithmic plots of R_{rec} vs V_{oc} (Figure 4.23), β values of 0.86, 1.02 and 1.04 were obtained for PTB7:C₇₀:PyBB cells prepared in 1:1, 1:2 and 1.3 D/A ratio, respectively, confirming a prevailing first-order process for these device, attributed to the recombination of mobile charge carriers with trapped ones.

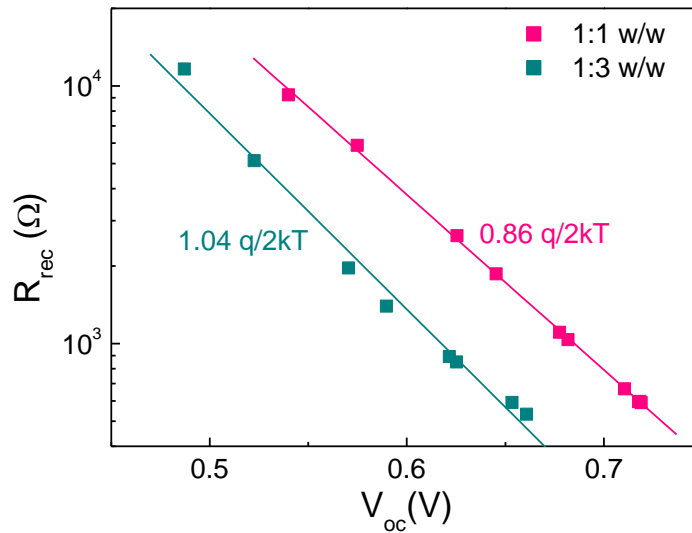


Figure 4.23 Recombination resistance as a function of the open-circuit voltage for PTB7:C₇₀:PyBB solar cells prepared with a D/A weight ratio of 1:1 and 1:3.

4.4 Discussion

The performance of solar cells made of PTB7 or PCDTBT as donors and neat-C₇₀ as acceptor are mainly limited by the charge transport properties in the blends, compared to the reference cells made of PC₇₀BM. Upon replacing PC₇₀BM with C₇₀, the mobility of positive carriers in the donor phase is roughly reduced by one order of magnitude, while that of electrons is only slightly modified. Though a

strong unbalanced transport was not observed in C₇₀-based cells, preventing space-charge formation, a limitation of the photocurrent due to a low $\mu\tau$ product was systematically observed, independently of the polymer donor and the D/A ratio. The effective lifetime of charge carriers did not change a lot by replacing PC₇₀BM with C₇₀, though was slightly reduced in neat-C₇₀ solar cells, but, combined with the lower mobility, contributed to the significant reduction of the $\mu\tau$ product in devices made of neat-C₇₀, compared to PC₇₀BM-based solar cells.

The modified charge transport properties of C₇₀-based cells were determined by the blend morphology, affected by the replacement of the acceptor. A highly segregated morphology was observed for PTBT:C₇₀ solar cells, with the formation of large domains with a size of hundreds of nm. Given the worse mobility of holes in these blends, poorly interconnected domains in the donor phase can be hypothesized. Differently, PCDTBT was an excellent dispersant for C₇₀ and the comparison of the surface morphology of PCDTBT:C₇₀ and PCDTBT:PC₇₀BM blends did not reveal significant differences, at least on the scale explored by the AFM. However, despite the relevant different morphologies of C₇₀-based blends made of the two polymers, a consistent reduction of the hole mobility was also observed for PCDTBT:C₇₀ solar cells, indicating that the D/A mixing is not so effective in the formation of the bicontinuous donor and acceptor domains required for efficient charge transport.

Nevertheless, thanks to the enhanced light absorption of the blends made of neat-C₇₀, PCDTBT:C₇₀ solar cells underwent a limited loss of efficiency (~ 5%), compared to the reference PCDTBT:PC₇₀BM, reaching a η of 4.55% and demonstrating that high efficiency solar cells made of cheap neat-fullerene are possible if the right donor is selected.

In order to obtain a better dispersion of C₇₀ in PTB7, a third component, PyBB, was introduced in the blends. The effectiveness of PyBB as dispersant of C₇₀ is clearly demonstrated by the AFM images. Indeed, the morphology of PTB7:C₇₀:PyBB blends does not show the formation of the micrometric agglomerates observed without PyBB. However, despite the huge morphological variation obtained with PyBB dispersant, the performance of PTB7:C₇₀:PyBB solar cells were not significantly improved with respect to those made without PyBB. The best performance was

obtained for the D/A ratio of 1:2 w/w, with an efficiency at one sun of 2.43%, to be compared with 2.22% obtained without pyrene.

The extended electrical characterization indicated that the main limiting factors of PyBB-based solar cells, both correlated to inadequate charge transport properties, are: space charge formation and charge trapping effects. Charge trapping is, at least in part, responsible for the drastic reduction of electron mobility in PTB7:C₇₀:PyBB solar cells. As a consequence, the strongly unbalanced hole and electron mobilities, differing by two orders of magnitude, lead to the formation of space charge, with a loss of performance for solar cells containing PyBB.

The origin of charge trapping upon addition of PyBB in the active layer is still under investigation.

CHAPTER 5 – CONCLUDING REMARKS

Charge transport properties constitute a major determining factor for the operation of any electronic device and mainly for organic electronics, given the much worse mobility of charge carriers in organic materials, compared to that in conventional semiconductors. On the other hand, charge carrier mobility in organic solids is highly dependent on a number of factors (chemical structure, deposition conditions, and macromolecular parameters for polymers), as demonstrated in this Thesis for AnE–PVs conjugated polymers, which must be accurately controlled in order to obtain good performance for electronic applications.

AnE–PVs are a relevant class of conjugated polymers. By appropriately choosing the lateral side–chains and the deposition conditions, affecting the electronic interaction between the conjugated backbones and the order degree of the film, hole and electron mobilities of the order of 10^{-4} and 10^{-3} $\text{cm}^2 \text{V}^{-1} \text{s}^{-1}$ have been achieved, respectively. In addition, even a moderate variation of the molecular weight (just of a factor of two) has been found to induce a meaningful modification of charge carrier mobility, as well as of the optical properties of the polymer films. Interestingly, all investigated AnE–PVs show a very good ambipolar behaviour, demonstrated for the first time in this Thesis work.

For the photovoltaic application, the correlation between charge transport properties and device performance is much more critical than for other organic devices, given the particular arrangement of the donor and acceptor phases in the active layer of BHJ solar cells. As a consequence, charge carrier mobility in the two different phases of the donor/acceptor blend is highly determined by the blend morphology, in addition to that exhibited by the pristine materials, and most of the losses of BHJ solar cells are currently due to low and/or unbalanced mobilities.

Concerning the intrinsic charge transport properties of pristine photovoltaic materials, a straight correlation between hole mobility in pristine AnE–PVs and the fill factor of the related solar cells, using PCBM as acceptor, has been found. However, the great impact of charge transport for the performance of BHJ solar cells is more clearly demonstrated by the results obtained on BHJ solar cells made of

neat-C₇₀, instead of its soluble derivatives. The aim of the work was to give a contribution to further restrain the costs of active materials, low cost being one of the main advantages of this innovative photovoltaic technology.

The performance of solar cells made of PTB7 or PCDTBT as donors and neat-C₇₀ as acceptor are mainly limited by the charge transport properties in the blends, compared to the reference cells made of PC₇₀BM. Upon replacing PC₇₀BM with C₇₀, the mobility of positive carriers in the donor phase is roughly reduced by one order of magnitude, while that of electrons is only slightly modified. Though a strong unbalanced transport was not observed in C₇₀-based cells, preventing space-charge formation, a limitation of the photocurrent due to a low $\mu\tau$ product was systematically observed, independently of the polymer donor and the D/A ratio. The modified charge transport properties in the C₇₀-based cells were determined by the blend morphology, affected by the replacement of the acceptor. A highly segregated morphology was observed for PTBT:C₇₀ solar cells, with the formation of large domains with a size of hundreds of nm. Differently, PCDTBT was an excellent dispersant for C₇₀ and the comparison of the surface morphology of PCDTBT:C₇₀ and PCDTBT:PC₇₀BM blends did not reveal significant differences. However, despite the relevant different morphologies of C₇₀-based blends made of the two polymers, a consistent reduction of the hole mobility was also observed for PCDTBT:C₇₀ solar cells, indicating that the D/A mixing is not so effective in the formation of the bicontinuous donor and acceptor domains required for efficient charge transport. Nevertheless, PCDTBT:C₇₀ solar cells underwent a limited loss of efficiency (12%), compared to the reference PCDTBT:PC₇₀BM, reaching an efficiency of 4.22% and demonstrating that high efficiency solar cells made of cheap neat-fullerene are possible if the right donor is selected.

The introduction of a third component in the blends, a derivative of pyrene, was greatly effective in improving the dispersion of C₇₀ in the PTB7 matrix, but a consequent improvement of the performance of the related solar cells was not observed. The strong unbalanced mobilities led to space-charge formation in the blends with pyrene and charge trapping effects were also found.

LIST OF PUBLICATIONS

1. Nadia Camaioni, Francesca Tinti, Alessandra Degli Esposti, Sara Righi, Ozlem Usluer, Sameh Boudiba, and Daniel A. M. Egbe “*Electron and hole transport in an anthracene-based conjugated polymer*” APPLIED PHYSICS LETTERS, **101**, 053302 (2012)
2. Francesca Tinti, Fedlu K. Sabir, Massimo Gazzano, Sara Righi, Christoph Ulbricht, Ozlem Usluer, Veronika Pokorna, Vera Cimrova, Teketel Yohannes, Daniel A.M. Egbe and Nadia Camaioni “*Tuning the properties of an anthracene-based PPE–PPV copolymer by fine variation of its macromolecular parameters*” RSC Advances, **3**, 6972 (2013)
3. Francesca Tinti, Fedlu K. Sabir, Massimo Gazzano, Sara Righi, Christoph Ulbricht, Ozlem Usluer, Teketel Yohannes, Daniel A.M. Egbe and Nadia Camaioni “*Effect of Side Chains on Charge Transport of Anthracene-Based PPE–PPV Copolymers*” DOI:10.1002/macp.201300611
4. Nicola Gasparini, Sara Righi, Francesca Tinti, Alberto Savoini, Riccardo Po and Nadia Camaioni “*Efficient bulk–heterojunction solar cells with neat C₇₀*” submitted.
5. Nicola Gasparini, Sara Righi, Francesca Tinti, Alberto Savoini, Riccardo Po and Nadia Camaioni “*Charge trapping in PTB7:C₇₀:pyrene bulk–heterojunction solar cells*” in preparation.

REFERENCES

- [1] <http://www.rsc.org/ScienceAndTechnology/roadmap/CS3-2013.asp>
- [2] B. D. Malhotra, et. al., *Pramana – J. Phys.*, **61**, 331 (2003).
- [3] P. Sonar, et. al., *Phys. Chem. Chem. Phys.*, **15**, 17064 (2013).
- [4] H. Yan, et. al., *Nature*, **457**, 679 (2009).
- [5] I. Mc Culloch, et. al., *Nature Mater.*, **5**, 328 (2006).
- [6] H. Sirringhaus, et. al., *Nature*, **401**, 685 (1999).
- [7] Worldwide Organic Electronics Market ww.productronica.com (1999).
- [8] W. Brutting, et. al., *Physics of Organic Semiconductors*, Wiley-VCH (2005) cap. 1.
- [9] T. A. Skotheim, et. al., *Handbook of Conducting Polymers*, Marcel Dekker (1998).
- [10] V. Coropceanu, et. al., *Chem. Rev.*, **107**, 926 (2007).
- [11] S. Holliday, et. al., *Chem. Mater.*, DOI: 10.1021/cm402421p.
- [12] J. L. Bredas et. al., *J. Chem. Rev.*, **104**, 4971 (2004).
- [13] A. J. Mozer, et.al., *J. Phys. Chem. B*, **108**, 5235 (2004).
- [14] D. M. Pai, *J. Chem. Phys.*, **52**, 2285 (1970).
- [15] W. D. Gill, *J. Appl. Phys.*, **43**, 5033 (1972).
- [16] H. Poole, *Phylos. Mag.*, **32**, 112 (1916).
- [17] J. Frenkel, *Phys. Rev.*, **54**, 647 (1938).
- [18] H. Bässler, *Phys. Status Solidi B*, **175**, 15 (1993).
- [19] A. W. Hains, et. al., *Chem. Rev.*, **110**, 6689 (2010).
- [20] Y. Sun, et. al., *Nat. Mater.*, **11**, 44 (2012).
- [21] S. Gunes, et. al., *Chem. Rev.*, **107**, 1324 (2007).
- [22] R. Po, et. al., *Energy Environ. Sci.*, **4**, 285 (2011).
- [23] R. Po, et. al., *J. Phys. Chem.*, **114**, 695 (2010).
- [24] R. Po, et. al., *J. Phys. Chem. Lett.*, **4**, 1821 (2013)
- [25] G. Yu, et. al., *J. Appl. Phys.*, **78**, 4510 (1995).
- [26] J. J. M. Halls, et. al., *Nature*, **376**, 49 (1995)
- [27] B. C. Thompson, et. al., *Angew. Chem. Int. Ed.*, **47**, 58 (2008).
- [28] P. T. Boudreault, et. al., *Chem. Mater.*, **23**, 456 (2011).
- [29] M. T. Dang, et. al., *Chem. Rev.*, **113**, 3734 (2013).

- [30] M. A. Green, et. al., *Prog. Photovoltaics: Res. Appl.*, **21**, 1 (2013).
- [31] H. J. Park, et. al., *Energy Environ. Sci.*, **6**, 2203 (2013).
- [32] L. J. A. Koster, et. al., *Appl. Phys. Lett.*, **88**, 052104 (2006).
- [33] J. D. Servaites, et. al., *Energy Environ. Sci.*, **4**, 4410 (2011).
- [34] H. Azimi, et. al., *Adv. Energy Mater.*, **1**, 1162 (2011).
- [35] E. Von Hauff, et. al., *Sol. Energy Mater. Sol. Cells*, **87**, 149 (2005).
- [36] K. N. Semenov, et. al., *J. Chem. Eng. Data*, **55**, 13 (2010).
- [37] M. A. Lampert, et. al., *Current Injection in Solids Academic*, New York (1970).
- [38] D. Gupta, et. al., *Proceedings of the IEEE*, **97**, 1558 (2009).
- [39] S. Bange, et. al., *Phys. Rev. B*, **81**, 035209 (2010).
- [40] K. Kassing, *Phys. Status Solidi*, **28**, 107 (1975).
- [41] C. J. Brabec, et. al., *Appl. Phys. Lett.*, **80**, 7 (2002).
- [42] W. E. Spear, *Proc. Phys. Soc. B*, **70**, 1139 (1957).
- [43] W. E. Spear, *Proc. Phys. Soc.*, **76**, 826 (1960).
- [44] O. H. Le Blanc, *J. Chem. Phys.*, **33**, 626 (1960).
- [45] R. G. Kepler, *Phys. Rev.*, **119**, 1226 (1960).
- [46] D. Poplavskyy, et. al., *J. App. Phys.* **93**, 341 (2003).
- [47] R. Schwarz, *J. Non-Cryst. Solids*, **227**, 148 (1998).
- [48] J. R. Macdonald, et. al., *Impedance Spectroscopy Theory, Experiment, and Applications*, Wiley-Interscience (2005).
- [49] P. W. M. Blom et. al., *Synth. Met.*, **121**, 1621 (2001).
- [50] A. Foertig, et.al., *Phys. Rev. B*, **86**, 115302 (2012).
- [51] C. J. Brabec, et. al., *Adv. Funct. Mater.*, **12**, 709 (2002).
- [52] A. Gadisa, et. al., *Appl. Phys. Lett.*, **84**, 1609 (2004).
- [53] V. D. Mihailetschi, et. al., *Appl. Phys. Lett.*, **93**, 216601 (2004).
- [54] M. Lenes, et. al., *Adv. Funct. Mater.*, **19**, 1106 (2009).
- [55] G. Garcia-Belmonte, et. al., *Sol. Energy Mater. & Sol. Cells*, **94**, 366 (2010).
- [56] A. J. Heeger, et. al., *Adv. Energy Mater.*, **1**, 517 (2011).
- [57] D. A. M. Egbe, et.al., *Macromolecules*, **43**, 1261 (2010).
- [58] Ö. Usluer, et. al., *J. Polym. Sci. Polym. Chem.*, **50**, 3425 (2012).
- [59] P. A. Troshin, et. al., *Adv. Energy Mater*, **3**, 161 (2013).

- [60] S. Saeb, et.al., *TEOCHEM*, **200**, 361 (1989).
- [61] M. Levitus, et. al., *J. Am. Chem. Soc.*, **123**, 4259 (2001).
- [62] D. A. M. Egbe, et.al., *Prog. Polym. Sci.*, **34**, 1023 (2009).
- [63] G. D. Sharma, et. al., *Appl. Mater. & Interface*, **2**, 504 (2010).
- [64] D. A. M. Egbe, et.al., *J. Mater. Chem.*, **20**, 972 (2010).
- [65] A. D. Becke, *J. Chem. Phys.*, **98**, 5648 (1993).
- [66] S. Rathgeber, et.al, *Macromolecules*, **43**, 306 (2010).
- [67] A. J. Campbell, et.al., *Appl. Phys. Lett.*, **79**, 2133 (2001).
- [68] A. J. Campbell, et.al., *J. Appl. Phys.*, **82**, 6326 (1997).
- [69] H. Scher et al., *Phys. Rev.B*, **12**, 2455 (1975).
- [70] P. E. Parris, et al., *Phys. Status Solidi B*, **218**, 47 (2000).
- [71] A. Zen, et. al., *Adv. Funct. Mater.*, **14**, 757 (2004).
- [72] C. Di, et. al., *Adv. Mater.*, **22**, 1273 (2010).
- [73] L. Pautmeier, et. al., *Synth. Met.*, **37**, 371 (1990).
- [74] P. M. Borsenberger, et.al., *J. Chem. Phys.*, **94**, 5447 (1991).
- [75] S. M. Tuladhar, et. al., *Phys. Rev. B*, **79**, 03520 (2009).
- [76] H. S. Lee, et.al., *J. Phys. Chem. C*, **117**, 11764 (2013).
- [77] H. Bässler, et. al., *Top. Curr. Chem.*, **1**, 312 (2012).
- [78] T. Tiedje, et. al., *Solid State Commun.*, **37**, 49 (1981).
- [79] H. Scher, et. al., *Phys. Rev. B*, **12**, 2455 (1975).
- [80] S. Rathgeber, et.al., *Polymer*, **52**, 3819 (2011).
- [81] R. C. Hiorns, et. al., *Adv. Funct. Mater.*, **16**, 2263 (2006).
- [82] N. Camaioni, et. al., *Appl. Phys. Lett.*, **101**, 053302 (2012).
- [83] G. Li, et. al., *Nat. Photonics*, **6**, 153 (2012).
- [84] C. J. Brabec, et. al., *Adv. Funct. Mater.*, **11**, 374 (2001).
- [85] D.E. Motaung, et. al., *Sol. Energy Mater. Sol. Cells*, **93**, 1674 (2009).
- [86] M. M. Wienk, et. al., *Angew. Chem., Int. Ed.*, **42**, 3371 (2003).
- [87] N. Blouin et. al., *Adv. Mater.*, **19**, 2295 (2007).
- [88] B. A. Collins, et. al., *Adv. Energy Mater.*, **3**, 65 (2013).
- [89] G. Namkoong, et. al., *Org. Electr.*, **14**, 74 (2013).
- [90] M. C. Scharber, et. al., *Adv. Mater.*, **18**, 789 (2006).
- [91] A. M. Goodman, et. al., *J. Appl. Phys.*, **42**, 2823 (1971).

- [92] T. Wang, et. al., *Adv. Funct. Mater.*, **22**, 1399 (2012).
- [93] P. W. M. Bloom, et. al., *Adv. Mater.*, **19**, 1551 (2007).
- [94] V. D. Mihailetschi, et. al., *Phys. Rev. Lett.*, **94**, 126602 (2005).
- [95] H. Azimi, et. al., *Adv. Energy Mater.*, **1**, 1162 (2011).
- [96] Z. He, et. al., *Adv. Mater.*, **23**, 4636 (2011).
- [97] A. Mani, et. al., *J. Phys. Chem. B*, **112**, 10086 (2008).
- [98] H. Zhou, et. al., *Adv. Mater.*, **25**, 1646 (2013).
- [99] G.J. Bahun, et. al., *J. Polym. Sci. A: Polym. Chem.*, **48**, 1016 (2010).
- [100] P.D. Tran, et. al., *Angew. Chem. Int. Ed.*, **50**, 1371 (2011).
- [101] V.D. Mihailetschi, et. al., *Adv. Func. Mat.*, **16**, 699 (2006).
- [102] A. Guerrero, et. al., *Org. Electr.*, **13**, 2326 (2012).

ACKNOWLEDGEMENTS

I would first like to acknowledge my assistant supervisor Dr. Nadia Camaioni for all the care and time she liked to spend in my Ph.D. education. She is an inspiring example of excellent professional attitude, honesty, and objectivity, which are qualities every good scientist should never lack. I thank her for helping me and for being always willing to explain and research.

I would like to thank my supervisor Prof. Stefano Stagni for his good will and his helpfulness.

My special thanks go to Francesca, Nicola and Roberta for their friendship and their moral support.

I recognize with gratitude the Research Center for non Conventional Energies, Istituto ENI Donegani, ENI S.p.A and the Consortium MIST E-R for the economic support.

Finally, my deepest thanks go to my family and friends whose unwavering love and irreplaceable presence have guided me throughout.